



HAL
open science

Réalisation des nanostructures désirées en or et en argent par effet thermique local induit optiquement : Application au stockage de données et à l'imprimante couleur

Fei Mao

► To cite this version:

Fei Mao. Réalisation des nanostructures désirées en or et en argent par effet thermique local induit optiquement : Application au stockage de données et à l'imprimante couleur. Physique [physics]. Université Paris-Saclay, 2020. Français. NNT : 2020UPASN011 . tel-02892554

HAL Id: tel-02892554

<https://theses.hal.science/tel-02892554>

Submitted on 7 Jul 2020

HAL is a multi-disciplinary open access archive for the deposit and dissemination of scientific research documents, whether they are published or not. The documents may come from teaching and research institutions in France or abroad, or from public or private research centers.

L'archive ouverte pluridisciplinaire **HAL**, est destinée au dépôt et à la diffusion de documents scientifiques de niveau recherche, publiés ou non, émanant des établissements d'enseignement et de recherche français ou étrangers, des laboratoires publics ou privés.

Realization of desired Au and Ag nanostructures by optically induced local thermal effect: Application to data storage and color printer

Thèse de doctorat de l'université Paris-Saclay

École doctorale n° 575 Electrical, Optical, Bio: Physics and Engineering (EOBE)

Spécialité de doctorat : physique

Unité de recherche : Université Paris-Saclay, CentraleSupélec, ENS Paris-Saclay, CNRS, Laboratoire de Photonique Quantique et Moléculaire, 94235, Cachan, France.

Référent : ENS Paris-Saclay

Thèse présentée et soutenue à ENS Paris-Saclay, par

Fei MAO

Composition du Jury

Fabrice VALLÉE

Professor, Université Lyon 1

Rapporteur

Jean-Christophe LACROIX

Professor, Université de Paris

Rapporteur

Duc-Tho NGUYEN

Associate professor, University of Georgia, USA

Examineur

Ngoc Diep LAI

Associate professor, ENS Paris-Saclay

Directeur de thèse

Isabelle LEDOUX-RAK

Professor, ENS Paris-Saclay

Présidente

Chi-Thanh NGUYEN

Research Engineer, CNRS

Co-encadrant

List of publications

- **Mao F.**, Pham T. N., Nguyen B. M., Li Z., Au T. H., Nguyen D. T. T., Tong Q. C., Pham T. L., Nguyen T. H., Tran Q. T., Lai N. D., “*One-photon absorption based direct laser writing for fabrication of multi-dimensional photonic and plasmonic nanostructures,*” Int. J. Nanotechnology (IJNT), accepted (2020).
- **Mao F.**, Davis A., Tong Q. C., Luong M. H., Nguyen C. T., Ledoux-Rak I., Lai N. D., “*Direct laser writing of gold nanostructures: application to data storage and color nanoprinting,*” Plasmonics 13 (6), 2285-2291 (2018).
- **Mao F.**, Davis A., Tong Q. C., Luong M. H., Nguyen C. T., Ledoux-Rak I., Lai N. D., “*Direct laser coding of plasmonic nanostructures for data storage applications,*” Nanophotonics VII 10672, 106722Z (2018).
- **Mao F.**, Tong Q. C., Nguyen D. T. T., Huong A. T., Odessey R., Saudrais F., Lai N. D., “*LOPA-based direct laser writing of multi-dimensional and multi-functional photonic submicrostructures,*” Advanced Fabrication Technologies for Micro/Nano Optics and Photonics X 10115, 1011509 (2017).
- Tong Q. C., **Mao F.**, Luong M. H., Do M. T., Ghasemi R., Tien T. Q., Nguyen T. D., Lai N. D., “*Arbitrary Form Plasmonic Structures: Optical Realization, Numerical Analysis and Demonstration Applications,*” Chapter 5, Book “Plasmonics”, IntechOpen (2018).

Contents

Acknowledgements	III
1 General introduction	1
1.1 Plasmonics	1
1.2 Fabrication techniques	5
1.3 Motivation and thesis plan	11
2 Realization of plasmonic nanoparticles in large area by thermal dewetting method in an oven	15
2.1 Introduction	15
2.2 Thermal annealing of plasmonic NPs	17
2.3 Simulations of Au and Ag NPs by FDTD method	24
2.4 Thermal annealing of Au + Ag films	29
2.5 Conclusion	34
3 Direct laser writing of Au and Ag nanoparticles and nanostructures	37
3.1 Introduction	37
3.2 Optically induced thermal effect: theory and simulation	38

CONTENTS

3.3	Realization of plasmonic nanostructures by DLW method	46
3.3.1	Continuous-wave based DLW method	46
3.3.2	Realization of Au and Ag NPs	49
3.3.3	Realization of plasmonic nanostructure with metallic NPs	55
3.3.4	Demonstration of direct fabrication of nanoholes arrays	57
3.4	Conclusion of chapter 3	64
4	Applications of fabricated plasmonic nanostructures	67
4.1	Introduction	67
4.2	Data storage	68
4.3	Color printer	74
4.4	Fluorescence enhancement	75
4.5	Random laser based on a monolayer of Au NPs	82
4.6	Conclusion and discussion	84
	Conclusion and prospects	87

Acknowledgment

In the past years, I have learned and grown a lot. With the help of professors, classmates, and friends, I was able to complete my doctoral studies.

First of all, I would like to express my deepest gratitude to my supervisor, Professor Ngoc Diep Lai, for his continued support of my doctoral research, for his patience, motivation and great knowledge. With the help of his guidance, I can research and write this thesis.

At the same time, I would like to express my heartfelt thanks to Dr. Chi Thanh Nguyen and Professor Isabell Ledoux-Rak, my co-supervisors, for their scientific guidance, consistent support, and encouragement during my Ph.D.

I want to thank my labmates who have worked with me for many years - Quang Cong Tong, Andrew Davis, Mai Hoang Luong, Dam Thuy Trang Nguyen, Kirill Kniazhev, Li Zhen, etc. It is really happy to work with them.

I am also very grateful to my colleagues and friends who gave me their help and time in these years, especially Dr. Rasta Ghasemi for her great help in cleanroom facilities and nano-manufacturing.

I would also like to thank all members of my defense committee: Professor Fabrice Vallée, Professor Jean-Christophe LACROIX, and Professor Tho Duc Nguyen for their insights and encouragement, as well as for embracing me to expand my problem.

CONTENTS

Last but not least, I want to thank my family for their support and constant encouragement over the period of my Ph.D.

Chapter 1

General introduction

1.1 Plasmonics

Plasmonics is a branch of optical condensed matter science devoted to optical phenomena in the nanoscale vicinity of metal surfaces [1]. When an incident light wave irradiates on a metallic nanostructure, different types of resonance modes appear due to the fluctuation of free electrons in the conduction band of the metal. The nature of these modes can determine the strength of the interaction between the incident light and the nanostructures. Therefore, the optical response of plasmonic devices can be controlled if there is some degree of control over the incident light and nanostructures.

The most famous report in the history of the plasmonic phenomena can date back to Lycurgus Cup (British Museum, London, UK 1902) [2]. It has a fantastic visual shock that its color could be changed under ambient lighting only one thing needs to change is the position where we put the light. As shown in figure 1.1, its color is green (a) and when putting the light inside the cup and let the light through it, then we could get a probably new Cup with glints bright red (b) [4]. Likely, the rose window of the Notre Dame Cathedral is also very impressive as figure 1.1 (c) shows. Great

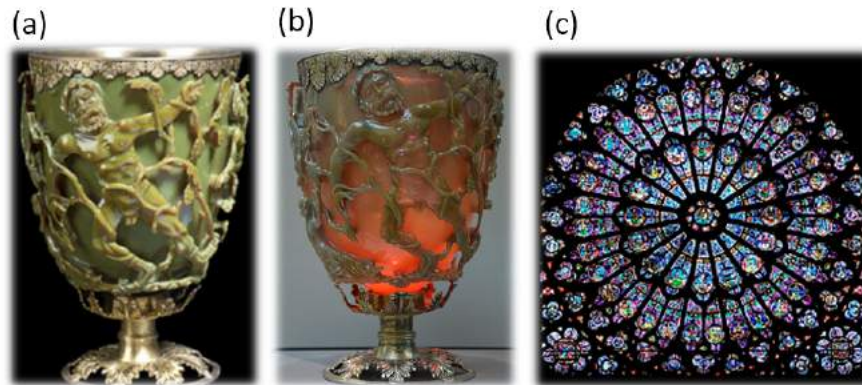


Figure 1.1: (a) Examples of decorative objects made by plasmonic nanoparticles. The Lycurgus Cup in reflected and transmitted light. Department of Prehistory and Europe, the British Museum [2]. (b) The rose window of Notre-Dame (about the year 1250) [3].

craftsmen used their excellent techniques to create such beautiful artwork which could light the nave with different colors. This may be amazing at that time and appeal a lot of attentions so that it gradually became a new research direction that dealing with the interaction between an electromagnetic field and free electrons in a metal. So now we know that is “plasmonic” effect, the color of the Cup changes due to gold and silver nanoparticles embedded in the glass [5].

With a huge number of investigations in the domain, we can separate the plasmonic effect in three types: surface plasmon polariton (SPP), localized surface plasmon resonance (LSPR), and plasmonic nanostructures (PNS).

SPP is an electromagnetic excitation existing on a metallic surface [6]. It is an intrinsically two-dimensional excitation whose electromagnetic field decays exponentially with distance from the surface. The propagation distance of SPPs depends primarily on the absorption of the metal and the thickness and surface roughness of the film. Figure 1.2 (a) illustrates the light propagation along with a metal-dielectric or metal-air interface, while only a particular wavelength and a particular incident

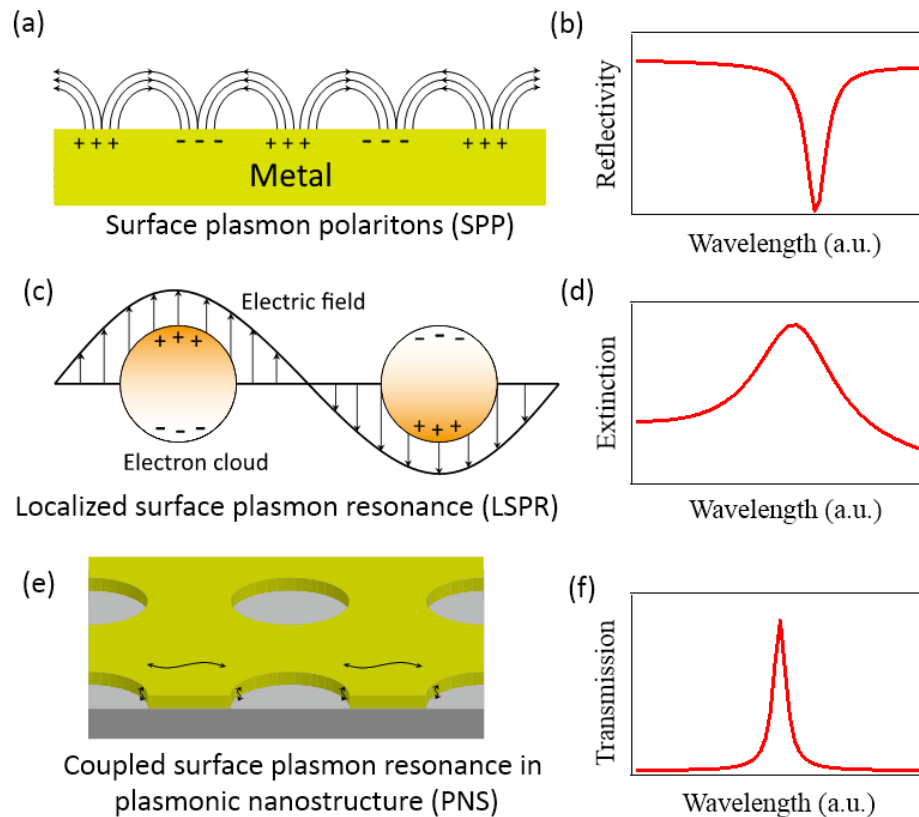


Figure 1.2: (a) Surface plasmon polariton (SPP) at a metal-air interface and corresponding reflectivity properties (b). (c) Localized surface plasmon resonance (LSPR) in isolated nanoparticles and corresponding plasmonic resonant spectrum (d). (e) Coupled surface plasmon resonance in a nanoholes array and corresponding transmission properties (f).

angle could propagate and the others will be reflected. The illustration of the reflectivity curve is shown in figure 1.2 (b), where we can see that the reflectivity is greatly reduced at a specific wavelength, called resonant mode. The SPP therefore paves the way for a number of applications. Figures 1.3 (a,b) show an example of integrated optical communication [7] and bio-sensors [8] based on the SPP.

LSPR is the result of the confinement of a surface plasmon in metallic nanoparticles (NPs) having a size smaller than the wavelength of the light used to excite the plasmon. Usually, when a particular light is focused on metal NPs, the electron os-

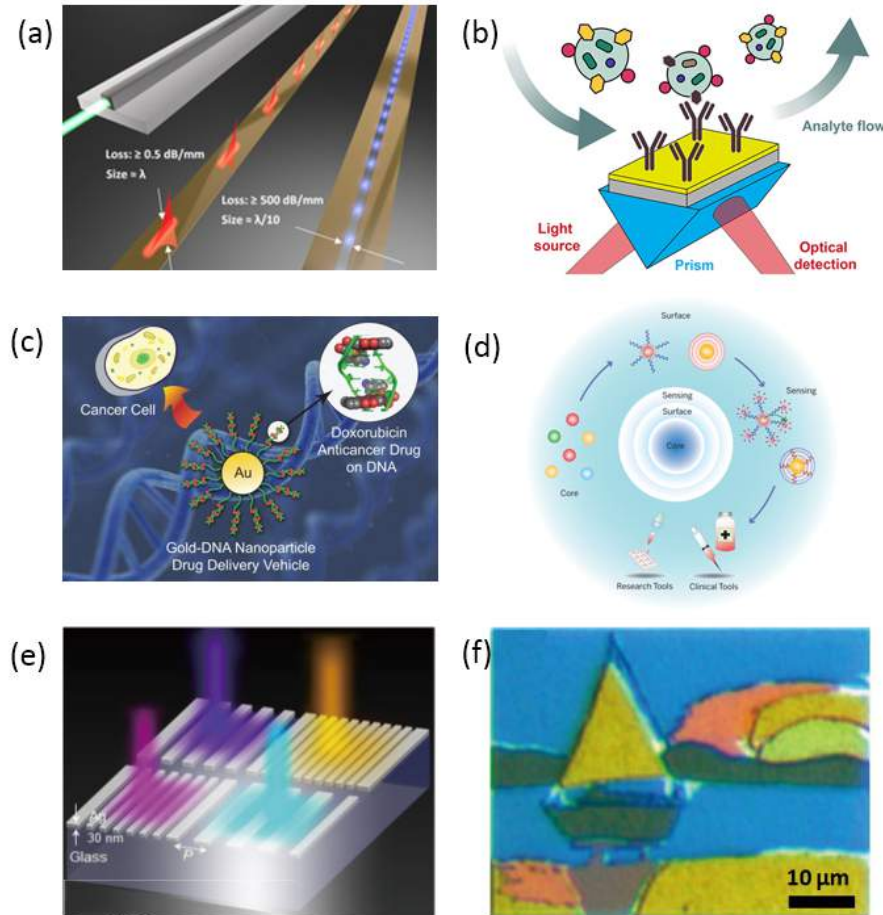


Figure 1.3: *Plasmonic applications of SPP: integrated optical communication (a) [7] and bio-sensors (b) [8]. Plasmonic applications of LSPR: gold nanoparticles in cancer therapy (c) [9] and bio-sensors (d) [10]. Plasmonic applications of PNS: light filters (e) [11] and nano color printing (f) [12].*

cillation at the NP surface will cause a charge separation and then leading to form a dipole oscillation along the direction of the electric field of the light. By that, the oscillation of the light field around the metal ball will be enhanced. Meanwhile, only certain wavelengths of light can be absorbed and scattered. This is called plasmonic resonance mode, as shown in Fig. 1.2 (d). The metallic NP becomes a very hot nano spot, with a temperature reaching several thousand degrees [13–15]. According to these optical properties of LSPR, many applications could be investigated: antimicro-

1.2. FABRICATION TECHNIQUES

bial effects [16], cancer treatment [17, 18], solar cells [19], light-emitting diodes [20], spectroscopy [21], signal enhancement for imaging [22], chemical synthesis [23], catalysis [24], photoelectrochemical [25], mechano-optical instrumentation [26], etc. Since LSPR is a localized effect, it is easy to dope metallic NPs into another material and to incorporate them into components, thus it has many other applications. Figure 1.3 (c,d) show the examples of cancer therapy [9] and bio-sensors [10] based on the LSPR.

Since LSPR strongly and locally amplifies the electromagnetic (EM) field near the metallic surface, many works propose to make LSPR propagating as in the case of SPP. Therefore, PNS does a good job to combine the effect of SPP and LSPR [27]. Indeed, when two metallic NPs are close enough, a strong EM field appears in the proximity of NPs surfaces, which may modify their surface potential and couple their plasmonic modes [28, 29]. Those modes can span over a broader optical spectrum as compared to their individual compartment. The spectrum of the coupled system is usually red-shifted and a relatively small or moderate splitting of the modes is observed [30–33]. Then, PNS with multiple metallic NPs [1, 34] or multiple nano-holes arrays (NHAs) [35–38] are studied. These PNSs allow having many applications since it has more degree of control, for example, the structure type, period, filling factor, etc. It seems that PNS is the best way of implementing many applications based on the plasmonic effect. Figures 1.3 (e,f) show the examples of light filters [11] and nano color printing [12] based on PNSs.

1.2 Fabrication techniques

There are many fabrication techniques that allow obtaining plasmonic structures. SPPs are the simplest structures, which can be obtained by creating a metallic thin

1.2. FABRICATION TECHNIQUES

film on a definite substrate by atomic deposition or evaporation method. The metallic film thickness is most important which can affect the propagation properties. The typical thickness of SPP is about 50 nm which can be made in a large area (few millimeters to few centimeters) or following a one-dimensional waveguide. The last one is done usually by using a template pre-fabricated by the mask lithography technique.

To get the metallic NPs, there are numerous fabrication techniques [39]. Chemical synthesis has been the primary means of growing a wide variety of metal NPs shapes (including stars [40, 41], rods [42–44], boxes [45], and cages [46–48]) because reaction conditions such as temperature, surfactants, and precursors can be independently controlled [49]. Extensive works of the different synthetic conditions and outcomes have been published elsewhere [50–59]. Although solution-based methods are scalable, the large distribution of shape and size of NPs within a single reaction vessel is still a challenge. Recently, the dewetting method [60] is also proposed to obtain a monolayer of NPs on a surface, where heating can be got from the electric or optically induced thermal effect. This technique shows a great advantage as compared to others since it allows obtaining NPs in the desired area [61] or even a structure of NPs by using a polymeric template prior annealing [62].

In order to obtain PNSs in a large area, we need to use various techniques such as a combination of interference lithography and gold etching [63–66], evaporation or sputtering of metallic materials onto structured polymeric templates [67–69], a combination of interference lithography and thermal annealing technique [70–72]. In addition, forming the desired configuration of metallic NPs in a small area, other methods are also necessary such as high-energy radiation metal membranes [73, 74], focused ion beam [75, 76], or a combination of nano-sphere lithography [77, 78], electron-beam lithography (EBL) [79–85], or direct laser writing (DLW) technique with lift-off method [86]. These methods are used to create the desired structures at nanoscale,

1.2. FABRICATION TECHNIQUES

so they are the most employed for PNSs fabrication.

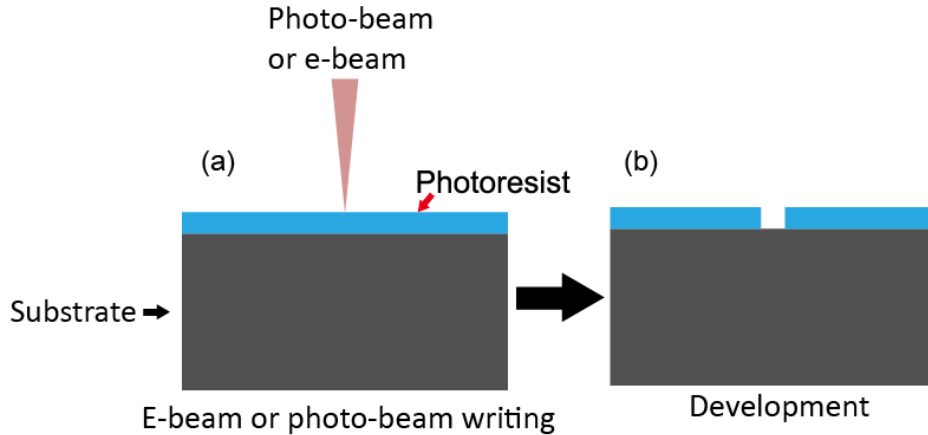


Figure 1.4: *Schematic diagram of e-beam or photo-beam lithography on a photoresist film (a) and the photoresist pattern after development (b).*

Here, we briefly introduce several common fabrication methods of PNS. The EBL, photolithography, and focused ion beam lithography have been the main techniques for fabricating nanoscale patterns. For plasmonic fabrication, a combined method of photolithography or EBL, and a lift-off process, called PEEL must be used. This is an indirect method that consists of two steps: template fabrication and metal structure formation. EBL appeared in the late 1960s [87] and consists of the electron irradiation of a surface that is covered with a resist sensitive to electrons by means of a focused e-beam. The main advantage of EBL over the conventional photolithography techniques includes very high-resolution [88]. This technique is used today for most PNS fabrication of high resolution and with arbitrary configuration. Besides, photo-beam lithography, also called photolithography or optical lithography, is the process of forming a pattern in a layer of an energy-definable polymer (photoresist). DLW or laser interference methods are widely used to fabricate sub-micrometer polymeric structures. Figure 1.4 illustrates a template fabricated by e-beam or photo-beam lithography on a photoresist film. The e-beam or photo-beam induces a change in

1.2. FABRICATION TECHNIQUES

the molecular structure and solubility of the resist film. After exposure, the resist is developed in a suitable solvent to selectively dissolve either the exposed (positive resist) or unexposed (negative resist) areas. After exposing and developing, the resist layer on top of the sample can be used as a mask or template for transferring the pattern into a metallic structure.

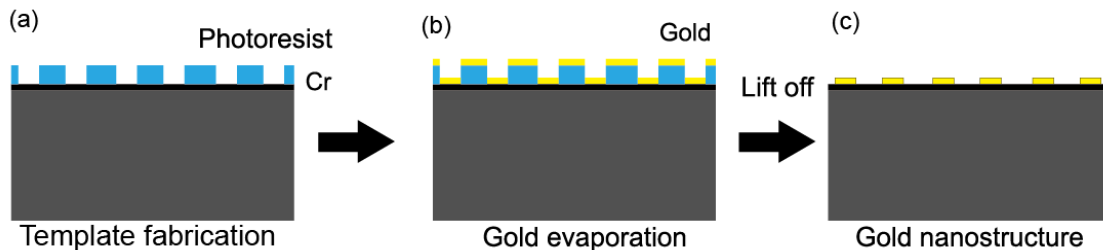


Figure 1.5: *Plasmonic structures fabricated by polymer templates and a lift-off method. First, the photoresist pattern is formed by e-beam or photo-beam writing (a), then gold film is evaporated on top of the structures (b), the plasmonic structure is obtained after the lift-off process (c).*

Figure 1.5 illustrates a nanopatterning procedure that transfers patterned features in a photoresist into plasmonic structures [89, 90]. First, photoresist patterns are fabricated by the EBL or photolithography method on a glass substrate as shown in Fig. 1.5 (a). Then a gold film is deposited on top of the polymeric pattern as illustrated in Fig. 1.5 (b). Finally, the sample is lifted-off to obtain the metallic nanostructures array (Fig. 1.5 (c)) by removing the polymeric template.

A combination of polymeric templates and plasma etching methods is also a common way to obtain plasmonic structures [91]. Figure 1.6 illustrates how to fabricate the metallic structure by this combination. The photoresist pattern is obtained by EBL or photolithography method on top of a metallic film that is deposited on the glass substrate. Then, the plasma etching is applied to remove the metallic film through the air holes leaving the metallic film under the photoresist part on a glass

1.2. FABRICATION TECHNIQUES

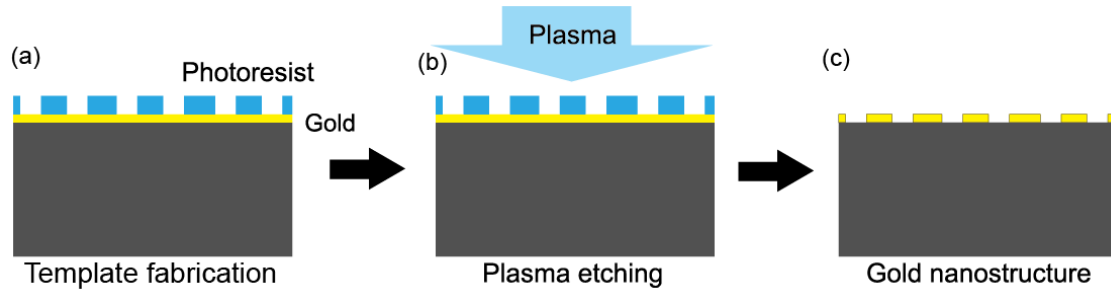


Figure 1.6: *Plasmonic structures fabricated by using polymeric template and plasma etching methods. First, the photoresist pattern is formed by e-beam or photo-beam writing on top of a metallic film (a), then plasma is used to etch the metallic material through the air holes (b), the plasmonic structure remains after removing polymeric template (c).*

substrate. After removing the polymeric structure, PNS is obtained as shown in Fig. 1.6.

These two combination methods are indirect ways to make the PNSs. An example of NHA fabricated by the DLW method and gold evaporation method is recently demonstrated in our laboratory and shown in Fig. 1.7 [92].

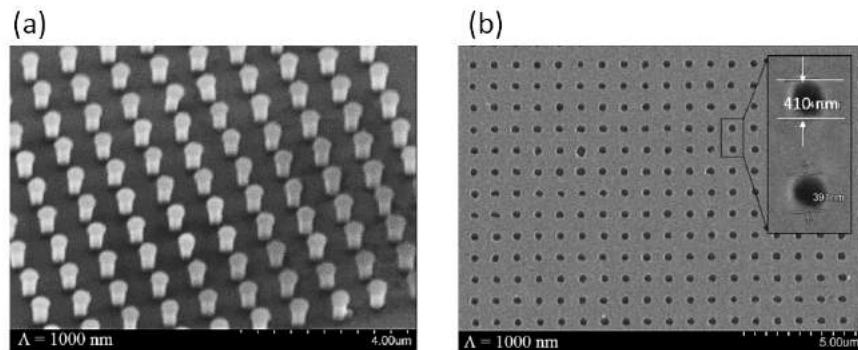


Figure 1.7: *SEM images of (a) photoresist pattern of nanopillars array fabricated by DLW method; (b) gold nanoholes pattern after the lift-off process [92].*

In order to directly fabricate PNSs (i.e. without photoresist template), it requires an energetic source that enables defusing metallic thin film. The focused ion beam

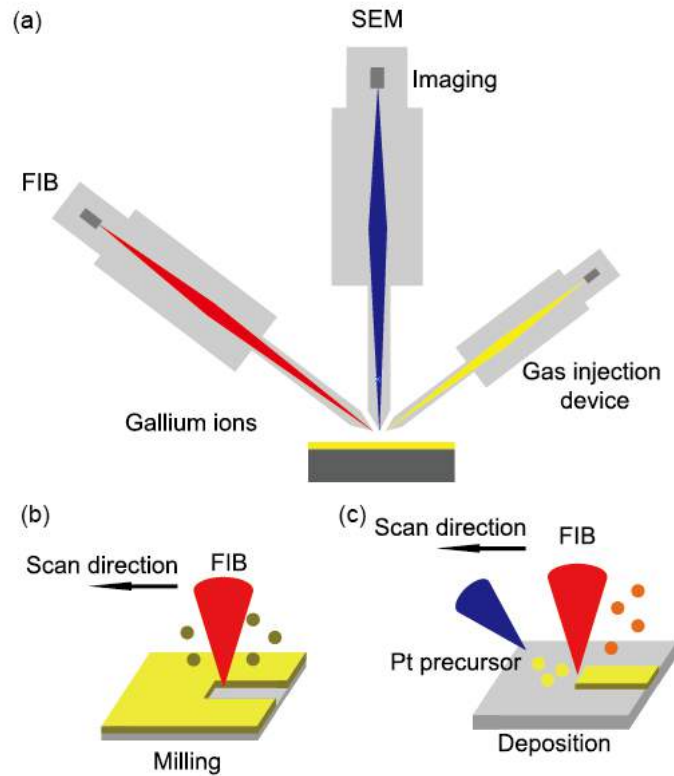


Figure 1.8: (a) Illustration of focused ion beam (FIB) system, which can be used in two ways for fabrications of metallic structures: milling (b) and deposition (c).

(FIB) technique is demonstrated as a direct way to fabricate plasmonic structures, which was mainly developed during the late 1970s and the early 1980s [93]. A typical FIB system is illustrated in Fig. 1.8 (a). The system contains three parts: scanning electron microscopy (SEM), FIB and gas inject system (GIS). By this FIB, two ways can be used to obtain desired plasmonic structures. Figure 1.8 (b) illustrates the fabrication of the milling method. The FIB allows removing the sample material using a high ion current beam. By scanning the ion beam over the substrate, a plasmonic structure with arbitrary shape can be obtained. In order to speed up the milling process, an etching gas can be introduced into the work chamber during milling. Figure 1.8 (c) illustrates the localized maskless deposition of both metal and insulator materials. The precursor gases are sprayed on the surface by a fine

needle (nozzle), the incident ion beam decomposes the adsorbed precursor gases. Then the volatile reaction products desorb from the surface and are removed through the vacuum system, while the desired reaction products remain fixed on the surface as a thin film. This FIB is robust but it is the most expensive method and it is not easy to have access to this method for most research laboratories.

So far, all these indirect and direct fabrication methods have been demonstrated. These techniques present many advantages but also some drawbacks. The fabrication of PNSs by indirect methods requires at least two steps, making this method rather complicated and expensive. FIB method has the advantages of high sensitivity, high resolution, and high stability, but it also has some disadvantages, such as it needs a high vacuum system, expensive and easy to damage the substrate. Therefore, it is necessary to develop a new method, simple and low-cost to realize PNS on-demand in a single step.

1.3 Motivation and thesis plan

In order to realize PNSs on demand, our lab has recently demonstrated the fabrication of Au NPs by a conventional thermal annealing process [94]. The experimental results show that the high-temperature annealing process melted the sputtered Au films, leading to the formation of isolated Au nano-islands, which exhibit a plasmonic effect with respect to the initial sputtered films. The distribution of metallic NPs dewetting on the oven is random in a large area. Then, thermal annealing of Au film by a high power continuous-wave (CW) laser beam is demonstrated [92]. To fabricate PNS in a small area and with the desired shape, an optically induced local thermal effect by using the DLW is applied [95]. This method is a direct way to fabricate desired patterns on demand. The optically induced thermal effect on an Au substrate

is studied, which can form the Au NPs on different substrates. Many interesting questions are then raised: can this DLW be applied to other metallic thin films, such as Ag or Au/Ag mixing films? Can DLW be used to create NPs array (NPA) or NHAs (like FIB)? What are the applications of these fabricated structures?

In order to answer these questions, we study theoretically and experimentally the use of the DLW employing a CW laser with controllable laser power to realize both NPA and NHA structures on gold and silver films. We investigate their optical properties and demonstrate some potential applications of fabricated 1D and 2D PNSs.

This thesis is organized as following:

In chapter 1, we briefly introduce the fundamental backgrounds of plasmonics, such as surface plasmon polaritons, localized surface plasmon resonance, and nano-holes array and their potential applications. Then, we introduce the common fabrication techniques of plasmonic structures and introduce the motivation of the PhD work.

In chapter 2, gold and silver NPs are elaborated by the thermal dewetting method using an oven in atmospheric conditions. We studied the optical properties of Ag NPs as a function of different fabrication parameters. A tentative fabrication of dual plasmonic structure by using a combination of Au and Ag film is also realized. The plasmonic effect is demonstrated in a good agreement between the FDTD simulations and the experimental characterizations.

In chapter 3, we first theoretically studied the optically induced thermal effect in a metallic film by using two simulation methods: Matlab and Comsol Multiphysics. We show that Matlab can be used to calculate the temperature distributions in an ideal model, while Comsol software not only can solve the ideal model but also can simulate the temperature distribution with a rough surface. All the simulation results

1.3. MOTIVATION AND THESIS PLAN

are compared to verify the correctness of the optically induced thermal effect model. To simulate the shape of the nanoholes array created in a real case, we calculated the temperature contour shape in the laser focusing area on a rough metallic surface. These results will guide for experimental realizations and explain the real fabricated structures. Then, we demonstrated the use of the DLW technique using a CW laser at 532 nm for the fabrication of plasmonic structures on demand. We first fabricated the plasmonic structures made of gold and silver NPs separately. Their optical properties are experimentally studied and compared with the simulation results obtained by the FDTD method. By increasing the laser power, we demonstrated for the first time the direct fabrication of gold NHAs with controllable size and structures. Their optical properties are simulated by FDTD method and compared with experimental characterization results.

In chapter 4, we demonstrated some applications of PNS with Au or Ag NPs, such as data storage, nano color printer, fluorescence enhancement, and random laser. We show that plasmonics based data storage is very promising, which can replace the traditional optical disks fabricated by using photorefractive materials. By varying the metallic NPs size, we demonstrated that this technique paves the way for some potential applications, such as QR codes at a submicro scale that is ideal for anti-counterfeiting. Finally, we demonstrated some preliminary results of random laser based on plasmonic NPs resized by the DLW technique.

In the last chapter, we summarize our works and discuss some prospects.

Chapter 2

Realization of plasmonic nanoparticles in large area by thermal dewetting method in an oven

2.1 Introduction

According to the physical and chemical properties, nanoparticles (NPs) can be classified into different types: carbon-based NPs, ceramic NPs, metal NPs, semiconductor NPs, polymeric NPs, and lipid-based NPs. According to the size and morphology, NPs can be classified into nanoball, nanorods, nanoshells, nanocages, etc. [96]

The most representative characteristics of the metallic NPs are the strong absorption/scattering peak in the visible range [97–100]. Namely, when the electronic vibration frequency of the metallic NP is equal to the incident light wave frequency, surface plasmon resonance (SPR) occurs, resulting in a strong absorption/scattering peak. Meanwhile, the peak position is very sensitive to the shape, size, and distribution of metal NPs. Their optical properties allow many applications such as nano-

optics [101,102], nonlinear optics [103,104], catalysis [105,106], thermodynamics [107], sensors [108–111], monitor [112], and medical diagnostics [113], etc.

With the development of modern nanotechnology, the fabrication of noble metal NPs can be prepared by break-down or build-up methods [114]. The break-down method is a technique for crushing the bulk metal by mechanical grinding [115], mechanical milling [116], or annealing by thermal effect [117–119]. The build-up method is a technique for assembling metallic atoms and has a lot of variations. Usually, the build-up method is used in a chemical reaction [120] or assemble in a solution [121], and the break-down method is used in physics grinding, machine milling, laser decomposition, and so on [122].

The dewetting method is widely used in nanostructure fabrications [123,124]. In the research of Hayashi et al. [125], they discovered that the melting point is decreased by reducing a metallic particle to nanolevel [126]. This opens a way to obtain metallic NPs with a moderate temperature, by using simply an electric oven.

In this chapter, we use a break-down method of thermal annealing technique to realize a monolayer of metallic NPs in large area. We first investigate the formation of gold (Au) and/or silver (Ag) NPs and then their mixture by using the oven annealing method. We experimentally show the variation of the size of formed Au and Ag NPs as a function of the annealing temperature and the annealing time. Simulations by the finite-difference time-domain methods are used to study the plasmonic properties of a monolayer of Au and Ag NPs, which are then compared with the experimental ones. We also simulate the plasmonic properties of the mixed Au/Ag NPs, and study theoretically the environmental effect.

2.2 Thermal annealing of plasmonic NPs

Figure 2.1 shows the fabrication of Au or Ag NPs monolayer by using the thermal dewetting method in an oven. Metallic NPs can be formed on the surface of a glass substrate.

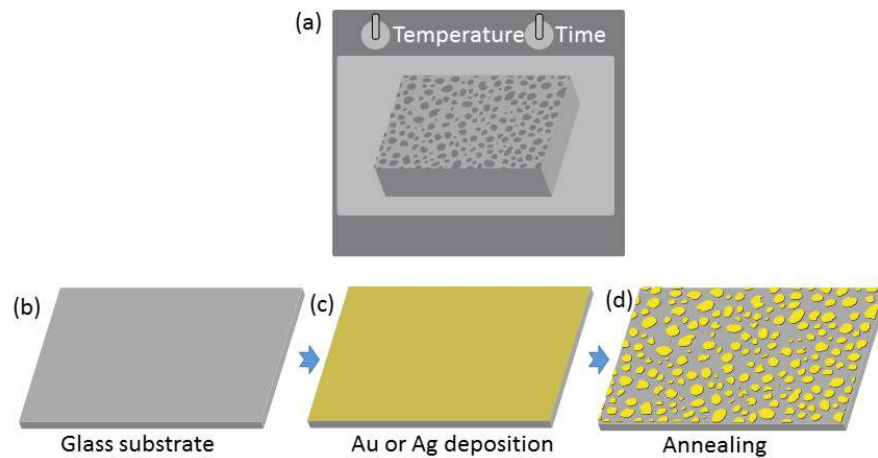


Figure 2.1: (a) Illustration of the dewetting method by oven annealing. (b-d) Annealing process of gold/silver nanoparticles.

The fabrication process can be explained as follows: first, the Au or Ag film is deposited on a glass substrate. The Au films were deposited onto 1.1 mm thick standard glass substrates by using an Emitech K650 magnetron sputter. The deposition conditions are a DC argon plasma with a gas purity of 99.995% and a discharge current of 50 mA. The average sputtering time is eight minutes so that we can obtain a desired thin Au film of about 12 nm thick (measured by a Dektak profilometer). For Ag films, the evaporation machine (Edwards, model: Auto 306) is used to obtain a uniform Ag film, whose thickness is about 8 nm. The samples are putting inside a hot oven with suitable annealing temperature and time. Inside the oven, the Au or Ag film is heating under a suitable temperature that can form NPs in the air environment. After annealing, the samples are naturally cooled down to room temperature.

2.2. THERMAL ANNEALING OF PLASMONIC NPS

To characterize the morphology of Au and Ag NPs, a scanning electron microscope (SEM, Hitachi S3400N / EDS Thermo Electron) is used to obtain the image of NPs, of which the shape and size can be calculated. The typical SEM images of annealing Au and Ag NPs are illustrated in Fig. 2.2. After many experiments, the annealing temperatures of the Au and the Ag NPs are set to 500 °C and 200 °C, respectively, which are the most suitable values to form these metallic NPs. The size, shape, and distribution of Au and Ag NPs are quite easy to distinguish from these SEM images. And the distribution of Au or Ag NPs is linked to their metallic nature, their thickness and the film preparation method.

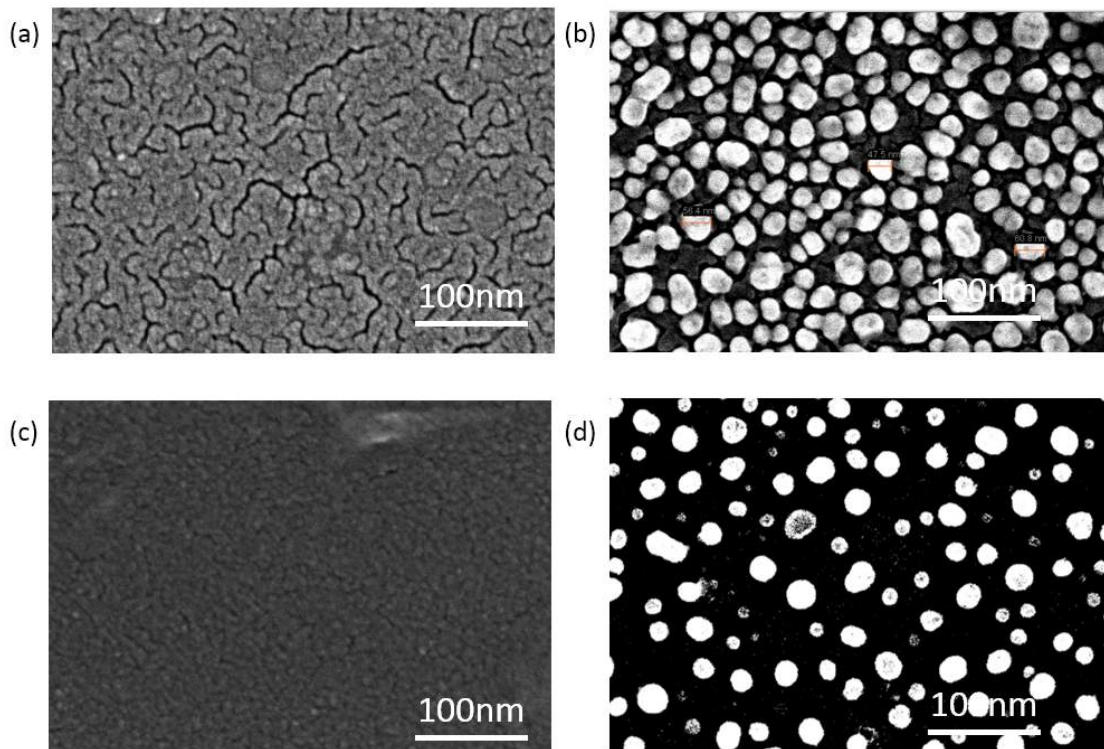


Figure 2.2: SEM images of (a) Au film and (b) Au NPs annealing at 500 °C; (c) Ag film and (d) Ag NPs annealing at 200 °C. The annealing times are both set to 30 minutes.

Influence of annealing temperature

After annealing with different temperatures while fixed the duration time, the

2.2. THERMAL ANNEALING OF PLASMONIC NPS

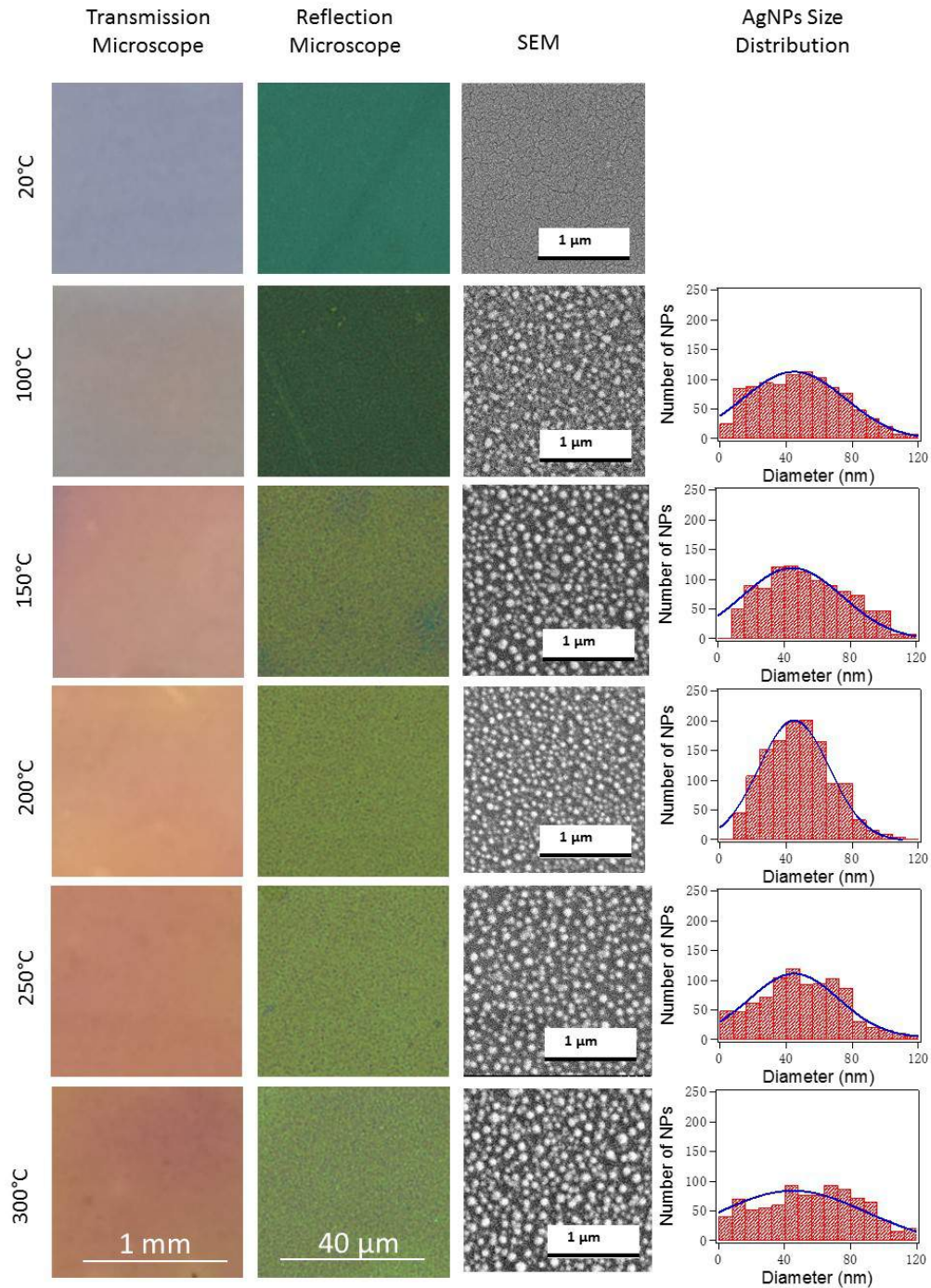


Figure 2.3: Results of Ag samples annealed with various temperatures by fixing the annealing duration at 30 min. The first column shows the transmission microscope images at large scale. The second column demonstrates the images taken in the reflection microscope. The third and fourth columns show the corresponding SEM images and Ag NPs size distributions, respectively.

2.2. THERMAL ANNEALING OF PLASMONIC NPS

plasmonic properties of the Ag film have dramatically changed as clearly shown in Fig. 2.3. The colorful images of transmission and reflection microscope change as the annealing temperature increasing. This is because, the resonance frequency of the NPs is affected by the NPs size and distribution, resulting in the color changes. The color changes from blue to orange, and then to dark red. The different annealing temperature results in the different average sizes of Ag NPs, as the SEM images illustrated in Fig. 2.3. As we can see in the SEM image, the Ag film starts changing to Ag NPs at 100 °C. When the temperature reaches 350 °C, all the film is evaporated, therefore we only show the results obtained with temperatures below 300 °C.

By analyzing the statistics of size distribution at various annealing temperatures, which is illustrated in the right column of figure 2.3, we found that the particle size slightly changes as a function of the annealing temperature. The best size distribution was obtained with 200 °C. This variation (size increases then decreases) is complicated together with the variation of particle height and also the number of particles. Therefore for Ag NPs, we adopted the annealing temperature as a key parameter to change the size of Ag NPs. Under 150 °C, the average size of Ag NPs is around 50 nm. If the temperature increase to 200 °C, the average size of the Ag NPs becomes smaller, about 40 nm. And then, if we continue to increase the annealing temperature, the average size will become bigger and bigger, and the size distribution is more scattered. Meanwhile, the peak is disappeared when the temperature reaches 350 °C, which implies that all the Ag film is evaporated from the substrate.

The distinction of the physical properties of Au or Ag NPs is reflected in the extinction spectrum, which is a combination of the absorption and scattering spectra. The plasmonic resonance of fabricated Au and Ag NPs is characterized by measuring the absorption spectra using a UV-Vis spectroscopy. Figure 2.4 (a, c) illustrates the influence of annealing temperatures on the formation of the Au and Ag NPs by the

2.2. THERMAL ANNEALING OF PLASMONIC NPS

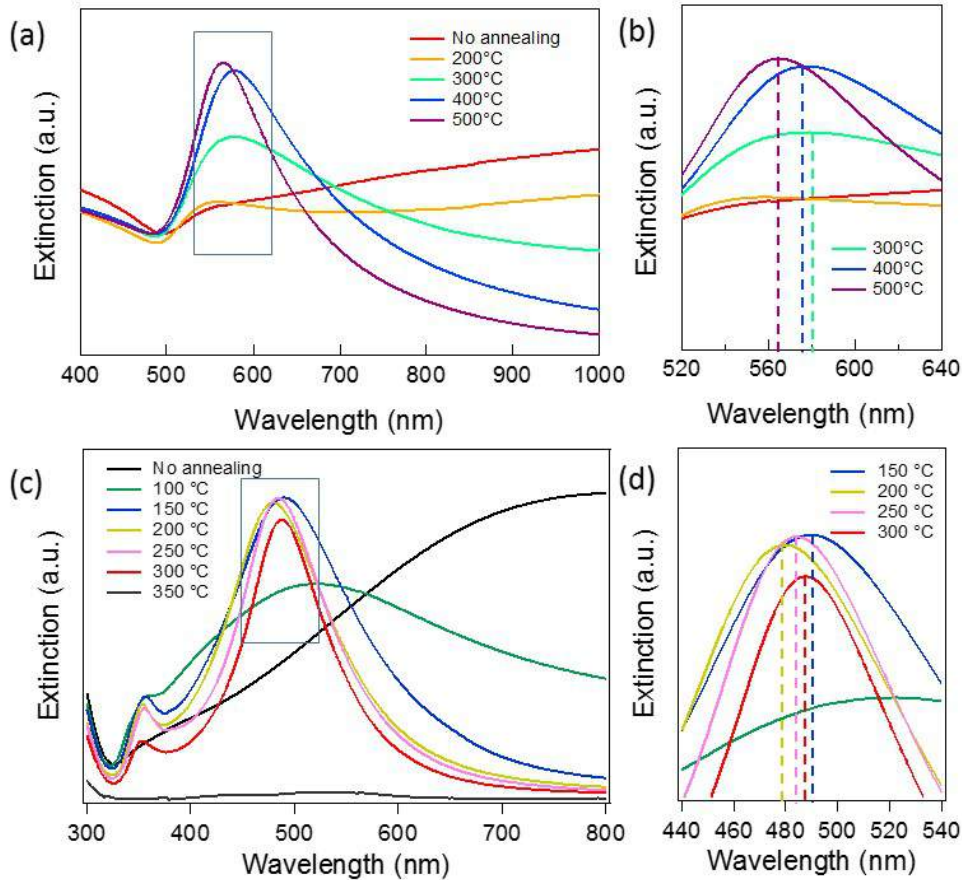


Figure 2.4: (a) The extinction (absorption and scattering combined) spectra of Au samples annealed with different temperatures in 30 minutes. (b) Detail of the extinction spectra. (c) The extinction spectra of Ag samples. (d) Detail of the extinction spectra.

thermal annealing method. We fixed the annealing duration time to 30 minutes and changed the annealing temperature from 200 °C to 500 °C for Au NPs, and from 100 °C to 350 °C for Ag NPs. From the combination of the SEM images and the Ag NPs distributions, we know that the dewetting effect happens when the annealing temperature reached 100 °C. When the temperature is chosen between 150 °C to 300 °C, the Ag NPs are formed, and the extinction peak, which means the combination of the absorption and the scattering, is almost unchanged. By studying more details in Fig. 2.4 (b, d), we found that, not like the Au NPs, where the extinction peak

shift in one direction, the extinction peak shifts of Ag NPs has a turning point in the annealing temperature of 200 °C. When the temperature increased from 100 to 200 °C, the extinction peak is blue shift. And when the temperature continues to increase from 200 to 300 °C, compared with 200 °C, the peak is redshift. This is consistent with the transmission microscope image, where we saw that the color changes from dark red to orange in 200 °C, and then become darker and darker again with high annealing temperatures.

Influence of annealing duration time

Besides the temperature, the annealing duration time is another important parameter in forming Ag NPs. We then fixed the temperature at 250 °C while changing the annealing time as 1, 5, 10, 30 and 45 minutes. By observing the microscope results, the sample color is hard to distinguish. This means that there is a little change in the position of the absorption peak. For studying in more detail the influence of the annealing time, we also studied the SEM images and size distribution of Ag NPs which can be referenced to the resonant spectra.

SEM images and corresponding size distributions are illustrated in Fig. 2.5. Using different annealing times, the average size of all Ag NPs is around 40 nm. The difference is that the numbers of NPs are gradually decreased when the annealing duration is increased. The extinction spectrum is measured and shown in Fig. 2.6 (a), where we can see that the peak intensity decreases when the annealing duration time increases, which is consistent with the number of NPs shown in Fig. 2.5. Figure 2.6 (b) shows, in more detail, the resonance peak as a function of the annealing time. The resonance peak does not shift, which is coherent with the sample color as explained before.

In conclusion, this dewetting method in an oven is suitable for fabricating Au and

2.2. THERMAL ANNEALING OF PLASMONIC NPS

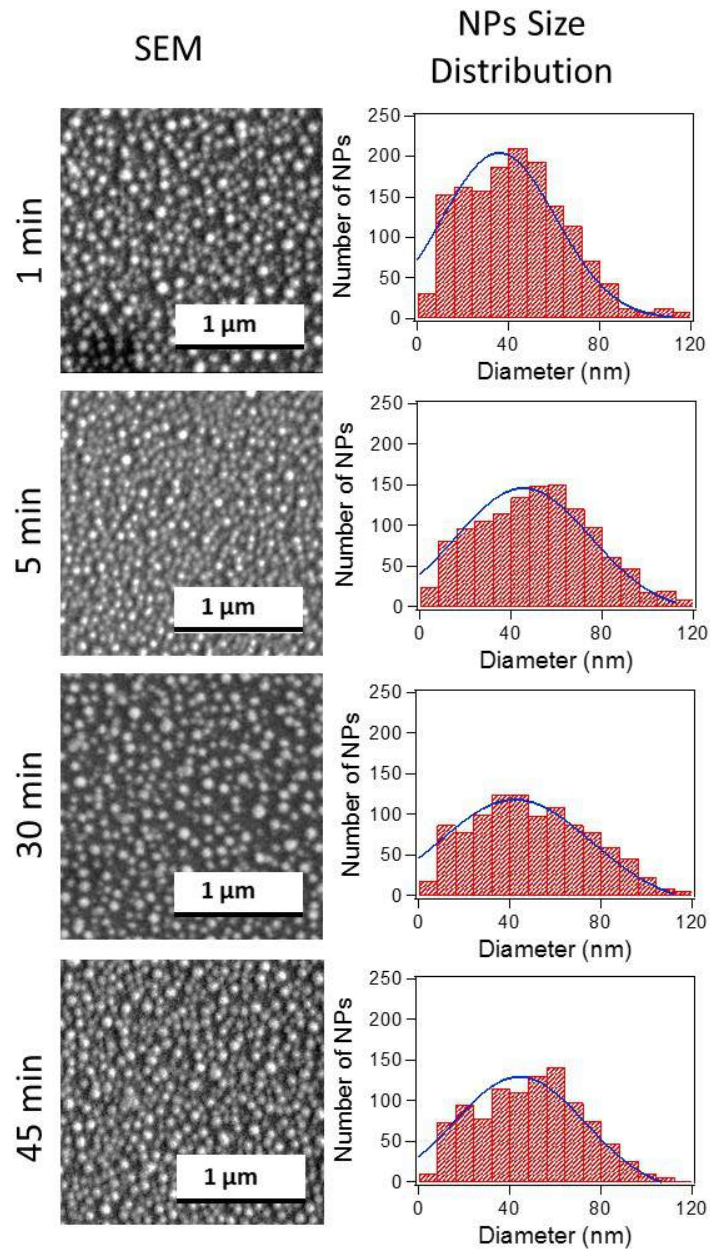


Figure 2.5: Results of Ag samples annealed with various annealing times while the annealing temperature was set to 250 °C. The first and second columns show the SEM images and Ag NPs size distribution, respectively.

Ag NPs in a large area, which has the advantage of rapid, easy and controllable fabrication. In order to understand the plasmonic properties of metallic NPs in monolayer,

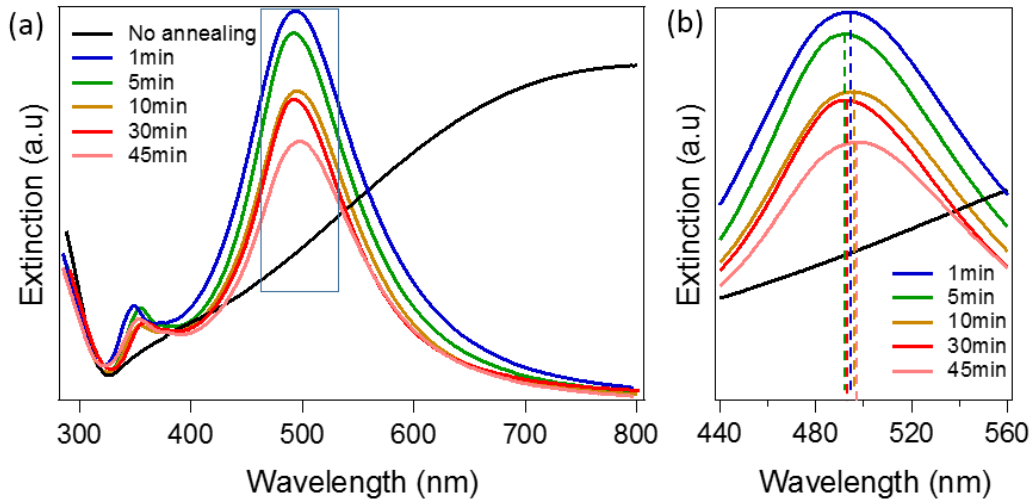


Figure 2.6: (a) The extinction (absorption and scattering combined) spectra of Ag samples annealed with different durations when the temperature was fixed to 250°C . (b) Detail of the extinction spectra.

as well as their size and shape dependence, we developed a simulation method based on a commercial Lumerical software.

2.3 Simulations of Au and Ag NPs by FDTD method

The Lumerical FDTD software is used to simulate the plasmonic resonance of metallic NPs. Not like the regular shape of Au or Ag NPs of other works [127,128], the metallic NPs fabricated in this work have a random shape, dispersed in a monolayer on a glass substrate. These NPs are also called nano-islands (NIs), which therefore need a particular simulation way to obtain their optical properties.

Figure 2.7 illustrates the reconstruction of randomly distributed metallic NPs in the FDTD model. This simulation method requires an SEM image and an AFM image. The SEM image is imported by Matlab in a 2D array, all the pixels are set to the grey mode. In this way, we can calculate the average size distribution and

2.3. SIMULATIONS OF AU AND AG NPS BY FDTD METHOD

count the numbers of the metallic NPs from the imported image. Figure 2.7 (a) demonstrates the top-view of NPs sizes and shapes in x - y coordinates. With the height estimated from the AFM image, as shown in Fig. 2.7 (b), the 3D surface is obtained and imported by FDTD software. Figure 2.7 (c) demonstrates the FDTD simulation configuration. The simulation area is bounded in the x - y plane where the periodical boundary conditions are defined. In z -direction, PML boundary conditions are applied to prevent any reflections. The absorbance spectra were calculated from Fourier transform time-dependent transmission monitor [94].

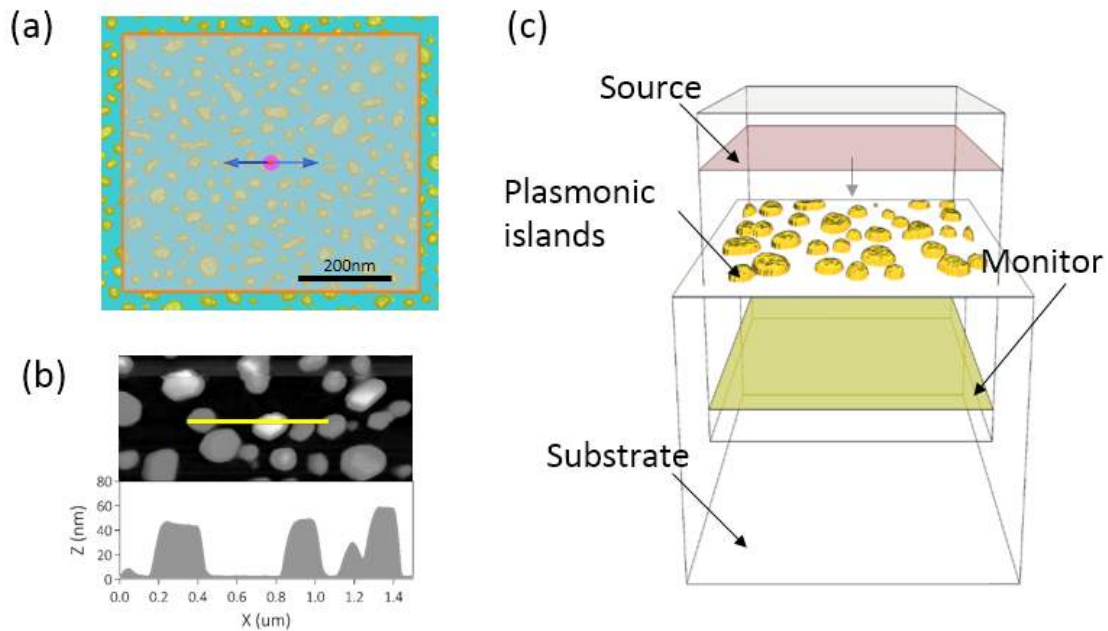


Figure 2.7: *FDTD model used to simulate the plasmonic resonance of metallic NPs on a glass substrate. (a) The imported data transformed from the SEM image by Matlab software. (b) The AFM image is used to obtain the height of NPs. (c) The Lumerical FDTD model set up to simulate the absorption of plasmonic NPs.*

Au NPs

Figure 2.8 (a) illustrates the absorption spectra measured from Au NPs and Au film. The resonant peak of Au NPs appears at 550 nm wavelength. Figure 2.8

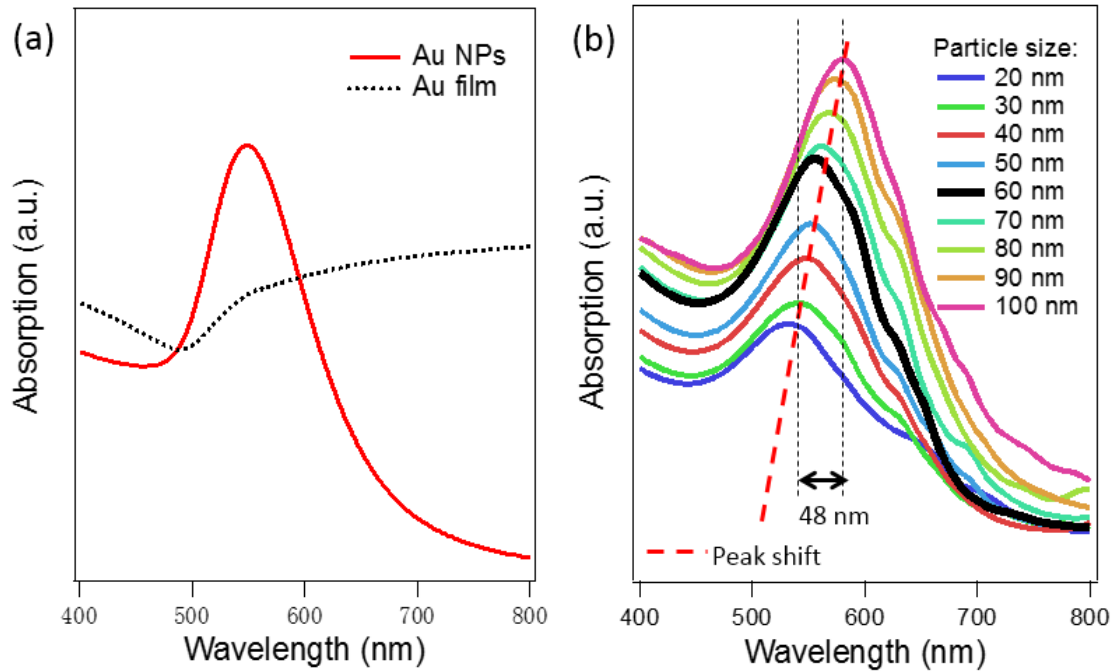


Figure 2.8: (a) The experimental absorption spectra of Au NPs and Au film. (b) The simulated absorption spectra of Au NPs with different average sizes of NP.

(b) shows the plasmonic resonant spectra of Au NPs having different average sizes obtained by the FDTD method. We can see that, if the particle size is assumed to be 50 nm, we obtained a very similar resonant spectrum as shown in Fig. 2.8 (b). This confirms the experimental results obtained during this work. Furthermore, when the average size of Au NPs became larger, the absorption peak is redshift. In this simulation, the size of Au NPs changes from 20 nm to 100 nm, resulting in a shift of about 48 nm for the resonant peak. That explains why we can use this Au NPs for nano color printer, and why we cannot change much the color.

Ag NPs

The FDTD method is also applied to obtain the absorption spectrum of Ag NPs. The SEM image in Fig. 2.2 (d) is imported to Lumerical software, in which the

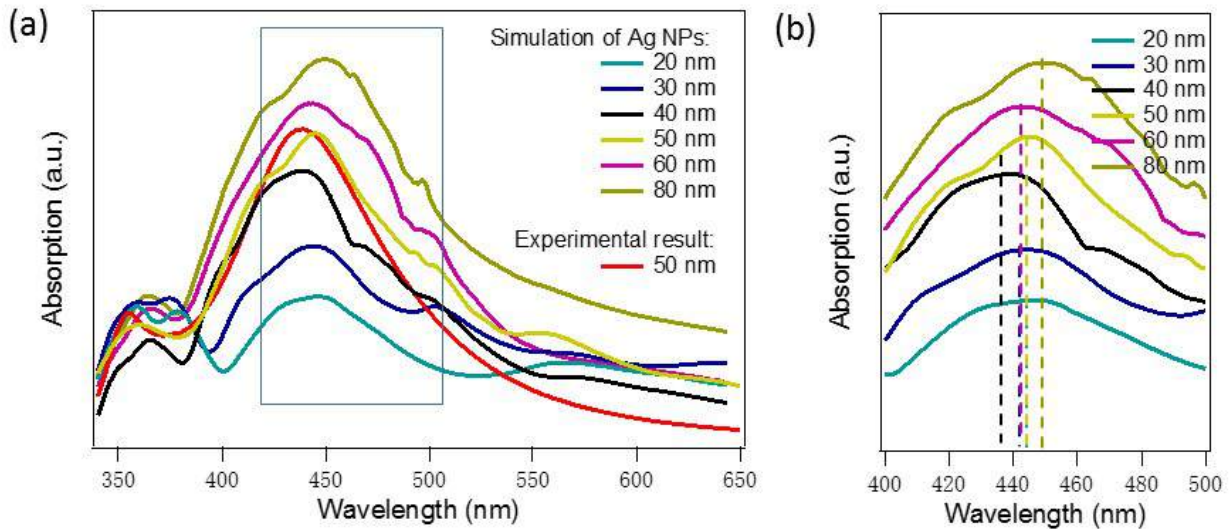


Figure 2.9: (a) Simulation plasmonic resonance spectra of the different average sizes of Ag NPs. The imported SEM image comes from the experiment whose plasmonic resonance spectra shows in the red curve. (b) Detail of the simulated peak position.

average size is calculated as 50 nm. Figure 2.9 (a) illustrates the simulated plasmonic resonance spectra of the different average sizes of Ag NPs. The imported SEM image comes from the experiment whose plasmonic resonance spectrum is also shown in the red curve. The simulation curve is not smooth for a limited simulation area having less Ag NPs than in the case of Au NPs, but the position of the main peak and the small peak is found on the same wavelength of the experimental one. Figure 2.9 (b) illustrates the detail of the simulation results of the absorption curve of Ag NPs having different average sizes. Unlike the Au NPs, the plasmonic resonance spectra of Ag NPs have two peaks. The main peak comes from the size distribution in the x - y plane, and the smaller one in the left is due to the height of Ag NPs [129]. In Fig. 2.9 (b), the resonance peak also has a shift when the size of NPs changes. This is consistent with the observable in experiment realized with different annealing temperatures.

Influence of environment

The environment around the plasmonic NPs is also a factor affecting the plasmonic

2.3. SIMULATIONS OF AU AND AG NPS BY FDTD METHOD

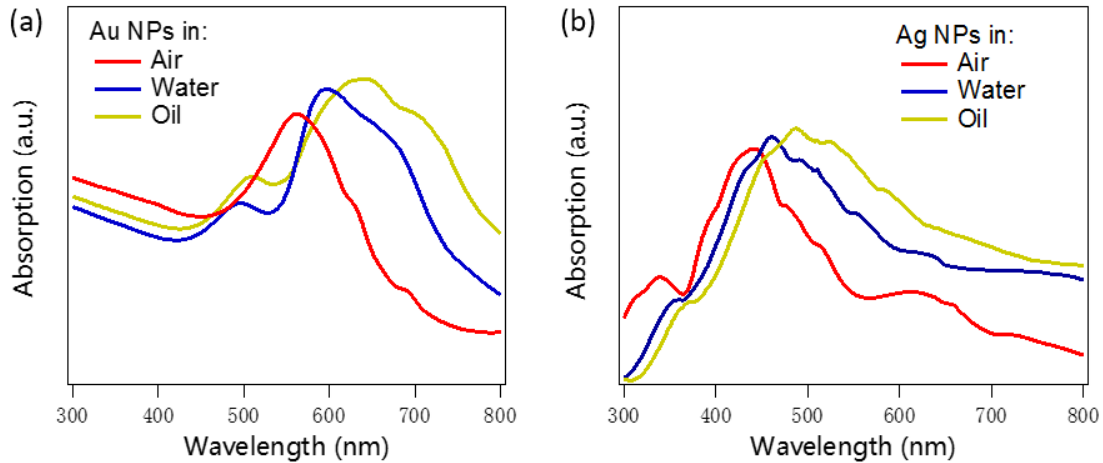


Figure 2.10: *FDTD simulation of the dependence of plasmonic properties of Au NPs (a) and Ag NPs (b) on environment.*

resonant peak. Here, we simulated the plasmonic properties of Au and Ag NPs located in the air, water, and oil environment to understand their dependence. Figure 2.10 illustrates the effect of the environment. In figure 2.10 (a), the absorption peak of Au NPs is redshift when we change the environment from air to water and to oil. This is because the plasmonic resonance of the NPs depends on the refractive index of the surrounding environment, where the refractive indices of air, water, and oil are 1, 1.33 and 1.6, respectively. In figure 2.10 (b), the plasmonic resonant peak of Ag NPs is also redshift when we change the environment from air to water, and then to oil.

From the simulation, we can confirm that even the shape of NPs is not perfectly circular or elliptical, and not uniform, the resonance peak still exists and as strong as in the case of perfect NP. By adjusting the size of the NPs, we can slightly change the resonant peaks, thus allowing applications like nano color printer. Compared to the perfect spherical NPs, the real NPs have a large resonant peak and not a smooth curve. The resonant peak of Au NPs is around 550 nm while the resonant peak of Ag NPs is around 450 nm in the air environment. We wonder if we make a mixed Au and

Ag NPs in the same sample, can we obtain a large plasmonic resonance range which can be interesting for a lot of applications.

2.4 Thermal annealing of Au + Ag films

Since the metallic NPs resonance frequency is related to material, we tried to form the NPs by combining Au and Ag materials. We expected that the plasmonic resonant peak would be a combination of resonant spectra obtained from pure Au NPs and Ag NPs.

From the previous results, we know that the annealing temperatures of Au and Ag NPs are not the same. For Ag NPs, the suitable dewetting temperature is ranging from 150 °C to 300 °C, but for Au NPs, the dewetting temperature is in between 300 °C and 500 °C [92]. So we'd like to set the annealing temperature at 300 °C which may be suitable to make the combined NPs.

In this experiment, all the samples are prepared by the evaporation method (Edwards, model: Auto 306) to deposit both the Au and Ag films. As the results shown previously, the thicknesses of Au and Ag films are set to 12 nm and 8 nm, respectively. We have prepared two kinds of deposition, an Au film on top or an Ag film on top of the other.

Figures 2.11 (a-b) illustrate the result of nanocomposite islands after annealing at 300 °C. This sample is prepared by depositing an Ag film on an Au film (Ag + Au). A transmission microscope image is illustrated in the insert figure showing the plasmonic color. For inverse deposition, i.e. an Au film deposited on an Ag film (Au + Ag), the results are shown in Fig. 2.11 (c-d). From the enlarged SEM images, we can see that NPs or NIs are not really formed but rather NIs with connections. The density of connected NIs of the (Ag + Au) sample is slightly weaker than that of the

2.4. THERMAL ANNEALING OF AU + AG FILMS

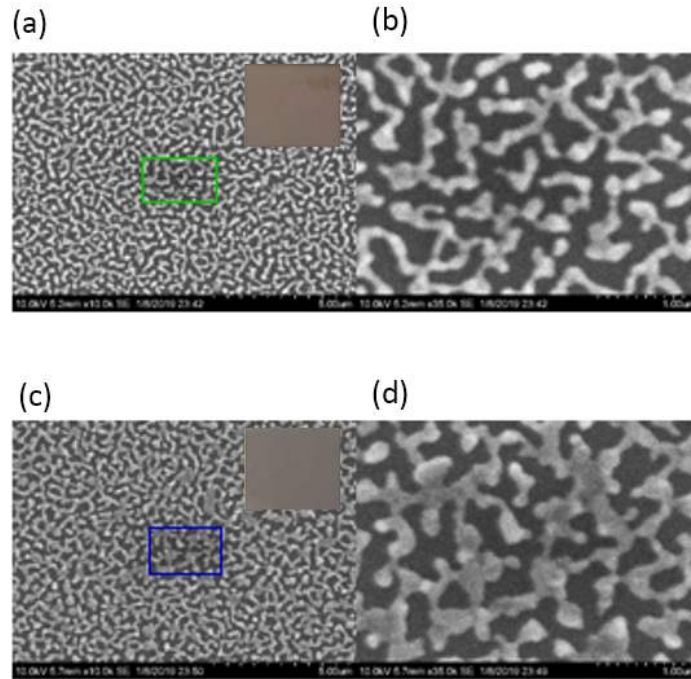


Figure 2.11: (a) SEM images of the annealed sample consisting of an Ag film on an Au film (Ag + Au). (b) Zoom in of (a). The insert is the transmission microscope image. (c) SEM image of annealed (Au + Ag) sample. (d) Zoom in of (c). Both of the annealing temperature and time are fixed at 300 °C and 30 minutes.

(Au + Ag) sample. This can be also observed from the microscope images, which show very similar colors.

We also performed the measurement of the absorption spectra of the nanocomposite samples and compared them with those obtained with pure Au or Ag materials, as shown in Fig. 2.12. The red and black curves present the pure Au and Ag NPs absorption spectra which are annealed with the same parameter. They all show the plasmonic resonant peaks due to the material nature and the NPs formation. And the grey and blue curves present the annealed structures of the (Ag + Au) and (Au + Ag) films. As we can see, there is no clear plasmonic resonant peak for the nanocomposite samples, which means that the mixed NPs are not formed at 300 °C. This is

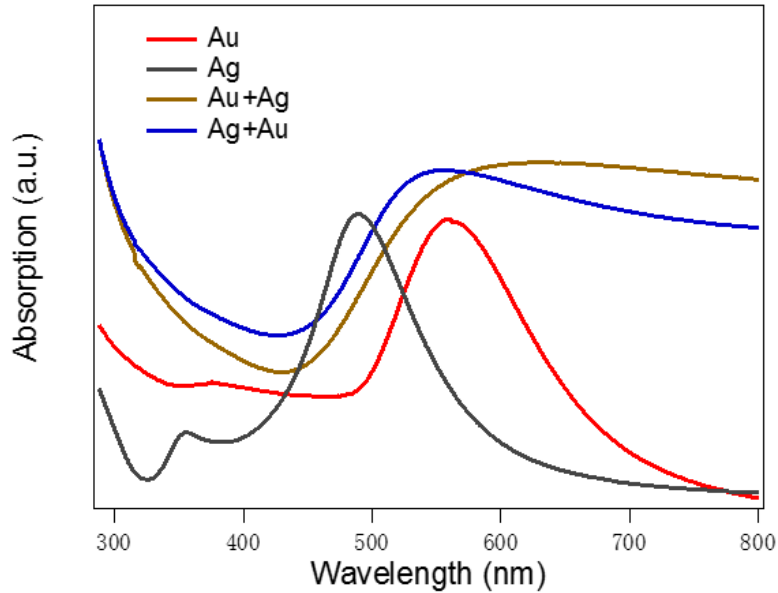


Figure 2.12: *The absorption spectra of thermal annealing of a combined Au and Ag films with an annealing temperature of 300 °C and an annealing duration of 30 minutes.*

consistent with the SEM images shown in Fig. 2.11, where the annealed films are represented as discontinued lines, but not NIs. These results, therefore, do not meet our expectations for the first test.

We have then attempted another method to obtain mixed NPs. Because the dewetting temperature of Au film is higher than that of Ag film, we first realized the Au NPs by the thermal annealing method using a pure Au material. Then the Ag film is deposited on the top of these Au NPs, which experiences another thermal annealing process. Figure 2.13 shows the annealing results of the corresponding sample. When the annealing temperature is increased from 100 °C to 300 °C, the Ag film is performed as the “bridge” to connect the Au NPs. When the annealing temperature reaching 400 °C and 500 °C, the shape of the mixed NPs appears clearly.

To confirm the existence of Ag material, we also performed the plasmonic resonant

2.4. THERMAL ANNEALING OF AU + AG FILMS

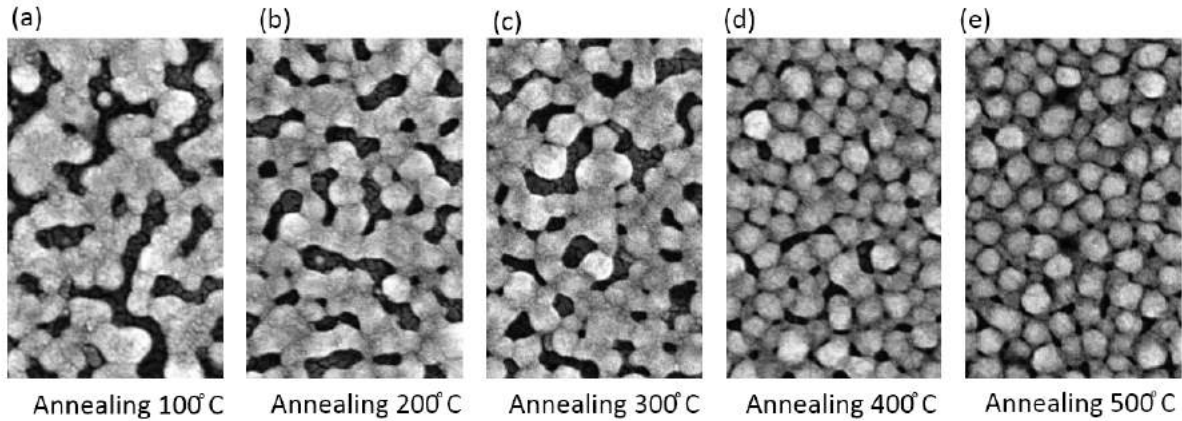


Figure 2.13: *Thermal annealing of an Ag film deposited on Au NPs. (a-e) SEM images of different samples obtained after annealing at different temperatures.*

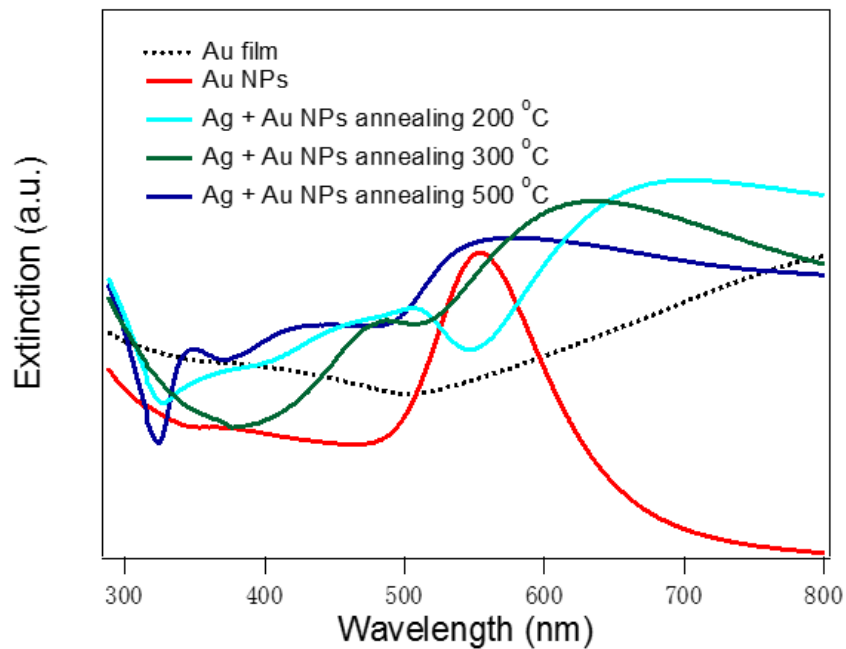


Figure 2.14: *The absorption spectrum of thermal annealing of an Ag film deposited on Au NPs with different annealing temperatures.*

measurement. Figure 2.14 shows the absorption spectra of Ag film covered the Au NPs with different annealing temperatures. Here, we see the existence of Ag after

2.4. THERMAL ANNEALING OF AU + AG FILMS

annealing at 500 °C, where there appears two peaks, the main peak (at about 560 nm) is at the resonance wavelength of pure Au NPs, and the smaller peak (at about 450 nm) is at the resonance wavelength of pure Ag NPs. To verify if the Ag covered on the Au NPs, we need another measurement method, such as Energy-dispersive X-ray spectroscopy (EDX), but this is out of time for this thesis.

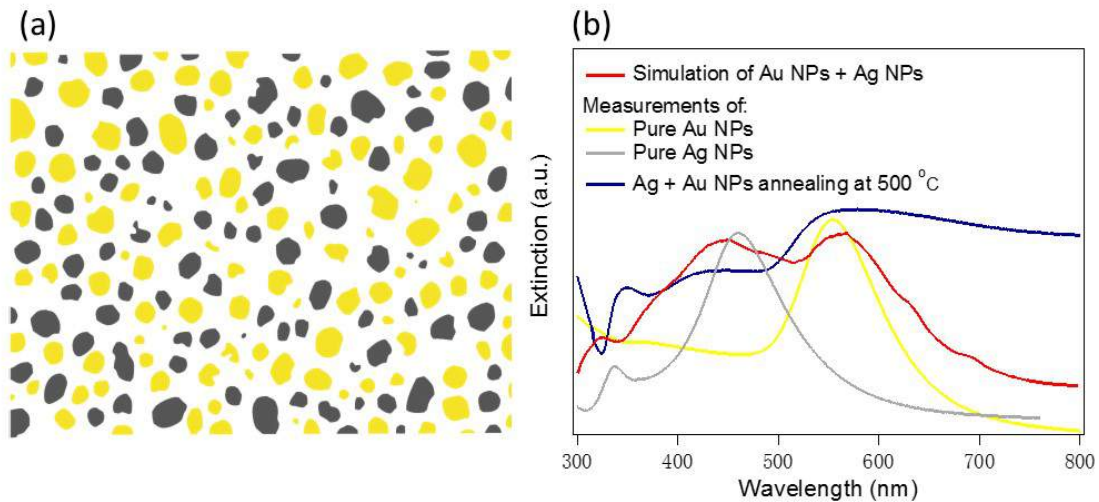


Figure 2.15: *FDTD simulation of mixed Au and Ag NPs. (a) Imported SEM image in which Au and Ag NPs are separated. (b) The simulated plasmonic spectra of mixed Au and Ag NPs, which is compared with the measurements.*

In order to understand the contribution of Ag and Au materials on the plasmonic resonant spectra of the combination, the FDTD simulations of mixed Au and Ag NPs have been also studied. In this simulation, half of NPs in the import SEM image are set as Au NPs (yellow color) and another half set as Ag NPs (grey color), as shown in Fig. 2.15 (a). The red curve in Fig. 2.15 (b) illustrates the simulated plasmonic resonance, where appears two main resonant peaks. The left peak represents the plasmonic resonant peak of Ag NPs while the right one corresponding to Au NPs. The experimental results of Au NPs, Ag NPs and (Ag + Au NPs) are also illustrated in Fig. 2.15 (b). Not like the pure Au NPs, the curve of (Ag + Au NPs) has a small

2.5. CONCLUSION

peak in the position of the peak from pure Ag NPs. This means the Ag still exist in the annealing of 500 °C in (Ag + Au NPs) film. The peak height of the simulation result is depending on the number of NPs. The simulated two peaks have the same height because the imported SEM image is set to have the same number of NPs to Au and to Ag. The resonant spectra of (Ag + Au NPs) shows the height of the peak at the position of Ag is smaller than Au, which means that the resonance of Ag covered Au NPs is much less than Au NPs itself. In another word, the Au NPs is not fully covered with Ag, only part of the Au NPs surface is covered.

To continue this idea, we can study different sizes of Au NPs and different thickness of covered Ag film. Moreover, we propose that the dewetting temperatures of the metallic films should overlapped, thus another material having the similar dewetting temperature can form better NPs.

2.5 Conclusion

In this chapter, we have theoretically and experimentally studied the formation of Au and Ag NPs by the dewetting method in an oven. The main results can be summarized as follows:

First, we demonstrate the Au and Ag NPs by the thermal dewetting method. By analyzing their SEM images, the morphologies, such as shape and size distribution, are characterized. We discussed annealing temperature and annealing duration to form Au and Ag NPs. At different annealing temperatures, the resonant peaks of Au or Ag NPs changed slightly, which corresponds to different average size distribution. And for different annealing durations, the intensity of resonant peaks is different, and it responds to different numbers of NPs.

Second, FDTD software is used to simulate the optical property of Au and Ag

2.5. CONCLUSION

NPs by importing SEM images of the random shape of NPs. When the average NPs size changes from 20 nm to 100 nm, the plasmonic resonant peaks of Au NPs are redshifted by 48 nm. For Ag NPs, when the average sizes are changed, the plasmonic resonant peaks also have the shift. Environmental impacts were also discussed. When the NPs are changed from air to water and then to oil, the resonant peaks shift red.

Third, the thermal annealing of a mixed Au and Ag film was studied. In the beginning, we tried to use the same annealing temperature, which can both form Au and Ag NPs separately, to form the combined Au and Ag NPs. We failed because they couldn't form NPs. After that, we tried to deposit the Ag on Au NPs. The resonance curve showed two peaks at the positions of the pure Au and Ag NPs. FDTD simulation results, which set half of the NPs as Au and the other half as Ag, are consistent with the peak position of the experiment, which means that Ag is covered the Au NPs.

Following this work, there are a lot of things to do, such as fabricating other metallic NPs, a new combined NPs, and studying their optical properties. These metallic NPs can be used in many applications, such as filters [130] and sensors [131]. In addition to forming large-area metallic NPs, small-area metallic NPs with required nanostructures have attracted more attention for widespread applications, which we will discuss in the next chapter.

Chapter 3

Direct laser writing of Au and Ag nanoparticles and nanostructures

3.1 Introduction

In the previous chapter, gold (Au) and silver (Ag) nanoparticles (NPs) are fabricated on the entire surface by an oven annealing method. Can we obtain Au and Ag NPs in a small area in order to realize plasmonics-based devices as desired? We proposed and demonstrated in this chapter a controllable method by using a laser annealing to fabricate on demand metallic NPs in desired areas.

The optically induced thermal effect is widely studied in laser-material interaction, especially in laser ablation [132, 133], laser cutting [134], etc. Recently, our lab [92] has demonstrated that it was possible to induce a thermal effect in a very small area by using a focused laser beam. This allowed to dewetting locally an Au film to realize Au NPs structure on demand [135]. In this work, we demonstrated that this optically induced thermal effect can be applied to other metallic materials, such as Ag film. In particular, by applying high laser power, we demonstrated for the first time the

3.2. OPTICALLY INDUCED THERMAL EFFECT: THEORY AND SIMULATION

fabrication of nanoholes array (NHA) in thick Au film. This is a direct technique without needing a polymeric template and the lift-off process.

In this chapter, we first study the optically induced thermal effect using the Comsol simulation method. We performed the simulation using a uniform metallic surface and compared the simulation results with those realized by the partial differential equation (PDE) method, which is already done in previous work [136]. Then, we demonstrated the optically induced thermal effect on a rough surface which corresponds to a real film to study the formation of NPs. Optically induced thermal effect on a thicker metal surface is also studied to check if we can use the direct laser writing (DLW) method to obtain plasmonic NHA structures. Then, we experimentally demonstrated the fabrication of Au and Ag NPs by the DLW method and compared them with the results obtained by the oven annealing method. Finally, we experimentally demonstrated the direct fabrication of Au NHA, with square and hexagon configurations, and theoretically studied their optical properties based on the SEM images and compared them with the ideal ones.

3.2 Optically induced thermal effect: theory and simulation

Following the theory applied for calculating thermal effect in polymeric material [137], we applied this theory of heat equation to calculate the heat distribution when a laser beam is focused on a metallic film. The heat equation is shown as:

$$\rho C_P \frac{\partial T}{\partial t} = k \nabla^2 T + S, \quad (3.1)$$

where ρ is the material density, C_P is the metallic heat capacity, k is the thermal

3.2. OPTICALLY INDUCED THERMAL EFFECT: THEORY AND SIMULATION

conductivity, and S can be calculated as a variation of light density in the material:

$$S = -\left(\frac{\partial I(r, z)}{\partial z}\right)_r = \mu_{\text{abs}}(1 - R_c)I(r, z)\exp(-\mu_{\text{abs}}z), \quad (3.2)$$

where $I(r, z)$ is the laser intensity, μ_{abs} is the absorption coefficient of the material, and R_c is the reflection coefficient. We note that the light beam propagates along z -direction.

We now need to apply this equation to find out the induced temperature in a real metallic sample. There are two kinds of simulation in dealing with the optically induced thermal effect. The description of the laws of physics for space- and time-dependent problems are usually expressed in terms of PDEs [138]. For the majority of geometries and problems, these PDEs cannot be solved with analytical methods. Instead, an approximation of the equations can be constructed, typically based upon different types of discretizations. These discretization methods approximate the PDEs with numerical model equations, which can be solved using numerical methods. The solution to the numerical model equations is, in turn, an approximation of the real solution to the PDEs. The finite element method (FEM) could be used to compute such approximations [139].

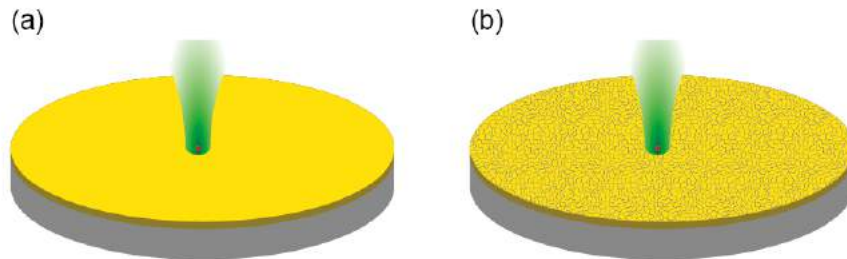


Figure 3.1: *Illustration of an ideal model, perfect uniform film (a) and a real model, rough film (b) of laser focusing on a metallic thin film.*

3.2. OPTICALLY INDUCED THERMAL EFFECT: THEORY AND SIMULATION

The optically induced thermal effect of the PDE method is widely studied by using the toolbox of Matlab software [136]. An ideal model has been proposed and applied to calculate induced thermal effect in different materials, such as SU8 [95]. In the PDE simulation, the optically induced thermal effect in the laser focus center is strong enough to reach the post bake temperature of SU8. Thus, by using laser-induced thermal effect instead of post bake, the smaller size of the nanostructure can be obtained. This method is also suitable for simulation of optically induced thermal effects in metallic materials. But it is only applied for the ideal model but not for the rough surface as a real sample. To simulate the optically induced thermal effect of a real rough surface, the FEM method of the Comsol simulation should be applied.

The models of an ideal and a rough surface are illustrated in Fig. 3.1, which are set into the Comsol software.

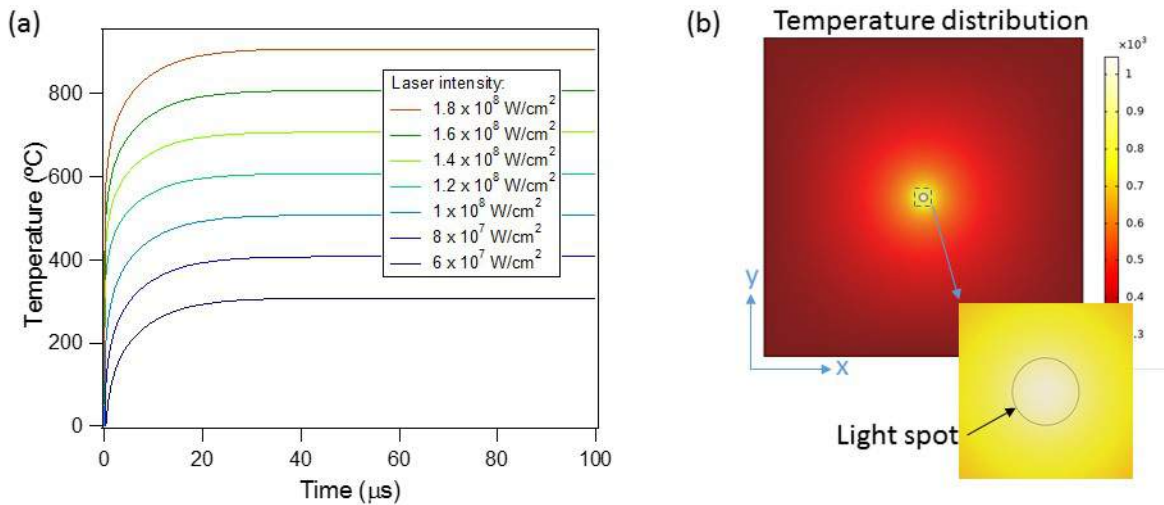


Figure 3.2: (a) Evolution of the induced temperature of a thin and uniform Au film with different laser powers in the focus center. (b) The induced temperature distribution around the focus point. The enlarged image illustrates the light spot.

Considering first the case of an Au uniform film having a thickness of 50 nm. The simulation parameters are used from the reference [94]: density of Au is 19.30 g/cm^3 ,

3.2. OPTICALLY INDUCED THERMAL EFFECT: THEORY AND SIMULATION

molar heat capacity is $25.418 \text{ J}/(\text{mol} \cdot \text{K})$, thermal conductivity is $318 \text{ W}/(\text{m} \cdot \text{K})$, absorption coefficient is $5.94 \times 10^7 \text{ m}^{-1}$, light densities in the material are from 0.6 to $1.8 \times 10^8 \text{ W}/\text{m}^{-2}$ which corresponding to a laser power from 80 to 240 mW, and the diameter of laser-focused area 300 nm.

In the laser focus center, the temperature with different laser powers over the laser exposes time is shown in Fig. 3.2 (a). The induced temperature is increasing obviously in the first $20 \mu\text{s}$, and it becomes stable when the exposure time duration is longer than $30 \mu\text{s}$. The stable temperatures depend on different incident laser powers. Figure 3.2 (b) illustrates the induced temperature distribution around the focus point, where the light spot is illustrated in the enlarged image.

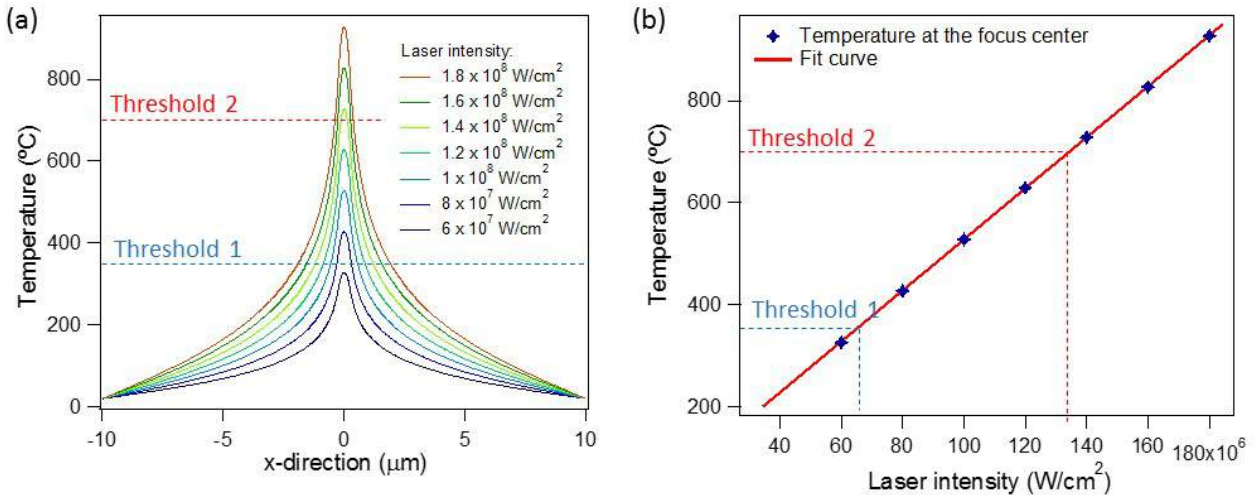


Figure 3.3: (a) The induced temperature profile along the x -direction obtained with different laser intensities. (b) The maximum induced temperature in the focus center changes with the laser intensity.

When the temperature becomes stable, we obtained a hot spot with the form quite similar to the light focusing spot. The temperature distribution along the x -direction is illustrated in Fig. 3.3 (a) as a function of laser intensities. The blue dotted line (threshold 1) indicates the temperature threshold for the dewetting effect of Au film.

3.2. OPTICALLY INDUCED THERMAL EFFECT: THEORY AND SIMULATION

This 350 °C value has been determined in previous work [92]. The red dotted line (threshold 2) illustrates the threshold of the evaporating temperature of 50 nm thick Au film, which was determined experimentally by the oven annealing method, to be around 700 °C. This temperature is much lower than the Au evaporation temperature of 1064 °C from the textbook [140]. This is because a thin rough Au film (50 nm) is easier to be evaporated than a thick Au crystal.

Figure 3.3 (b) illustrates the maximum induced temperature at the laser focus which linearly changes as a function of incident laser intensity. This result can be understood by looking at the heat equation shown in (3.1) and (3.2). In equation (3.2), the variable S is linearly changed with the laser intensity at a determined z . While the left side of the heat equation (3.1) becomes 0, the temperature value in the focus center linearly changed with S parameter, i.e. the laser intensity.

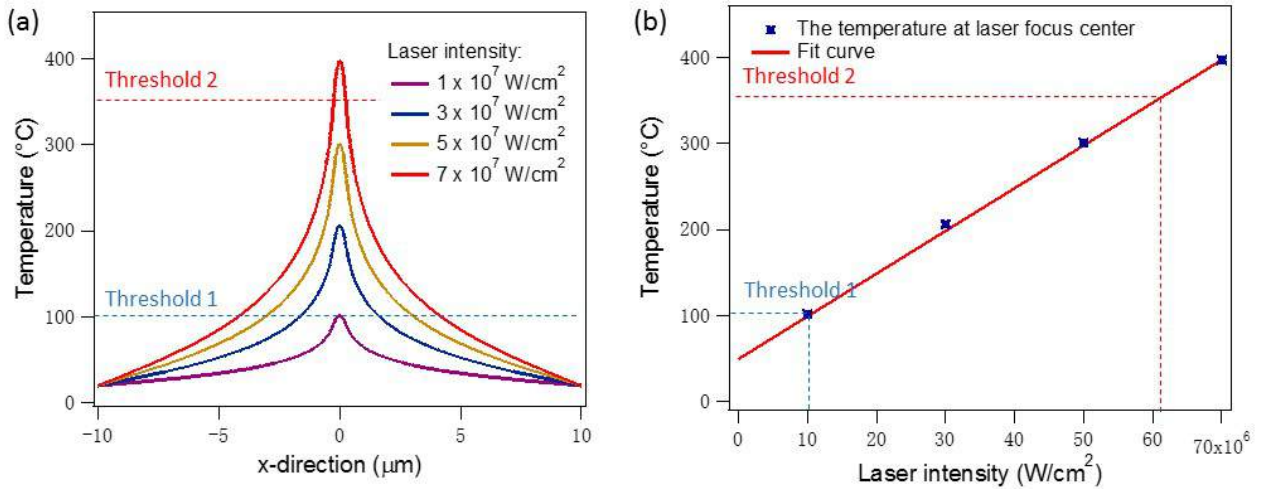


Figure 3.4: (a) Simulation result of the optically induced thermal effect of Ag film with a thickness of 8 nm by using Comsol software. (b) The maximum induced temperature in the laser focus center as a function of the laser intensity.

We realized the same simulation for Ag film. The optically induced thermal effect of Ag film is shown in Fig. 3.4. The parameters of Ag are chosen as [141]: den-

3.2. OPTICALLY INDUCED THERMAL EFFECT: THEORY AND SIMULATION

sity 10.49 g/cm^3 , molar heat capacity $25.35 \text{ J/(mol} \cdot \text{K)}$, thermal conductivity $235 \text{ W/(m} \cdot \text{K)}$, and absorption coefficient $8.35 \times 10^7 \text{ m}^{-1}$. The heat distribution in the x -direction is shown in Fig. 3.4 (a), in which the red dotted line (threshold 2) shows the threshold of evaporate temperature, and the blue dotted line (threshold 1) shows the NPs formation temperature. The suitable writing intensity by the DLW method is from $1 \times 10^7 \text{ W/cm}^2$ to $6.5 \times 10^7 \text{ W/cm}^2$, which seems lower than those required for Au film. In the laser focus center, the induced temperature also showed a linear dependence with the laser power or laser intensity as illustrated in Fig. 3.4 (b).

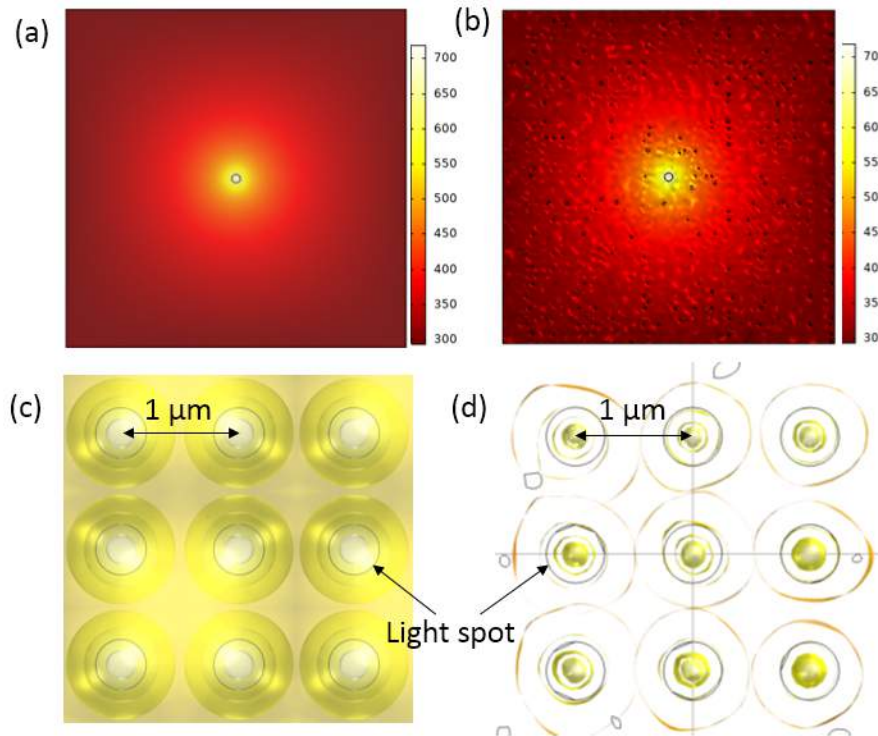


Figure 3.5: *Simulation of an array of hot spots induced in a 50-nm thickness of Au film. The optically induced heat distribution of one spot is illustrated in a uniform surface (a) and in a rough surface (b). The contour lines of the temperature distribution of light spots in the 2D array are illustrated in a uniform surface (c) and in a rough surface (d), where the black cycle is the light spot. The period of this simulated 2D structure is $1 \mu\text{m}$.*

3.2. OPTICALLY INDUCED THERMAL EFFECT: THEORY AND SIMULATION

In previous simulations, we assumed that the metallic films are perfectly uniform. But in practice, the films are rather rough, in particular with the very thin films due to the fabrication technique (sputtering). We, therefore, performed new simulations with rough film and compare the results with ideal cases.

We introduced a rough metallic surface by adding a random superimposed flexible function into a uniform metallic film. The simulation results obtained with uniform and rough Au films are shown in Fig. 3.5. In the uniform film, the heat transferred smoothly from the center area to the edge, but in the rough surface, the heat transfer is not homogeneously and uniformly. The iso-temperature curve shows that the distribution of the ideal model is a perfect circle, but for the rough surface, the contour curve is affected by the surface quality, which leads to a deformed circle. We expected that the DLW on real metallic thin film will create plasmonic NHAs, but the shapes and sizes of the holes will vary from this focusing spot to others. A non uniform NHA is therefore expected by this fabrication method.

Since the film roughness depends on the film thickness, and the induced temperature depends also on this parameter, we simulated the optically induced thermal effect with real samples having 12 nm and 50 nm thickness. The first sample (12 nm) is used for the fabrication of NPs by the dewetting method and the other (50 nm) is used for fabrication of NHA.

Figure 3.6 shows the heat distribution of these two kinds of thickness. Because the Au film obtained by the deposition method has a lot of “scratches” on the surface, the 12-nm Au film surface has many small “holes”, as shown in Fig. 3.6 (a). The thermal effect at the laser focusing area is therefore not continuous but stopped by these “holes”, as shown in Fig. 3.6 (b). When the induced temperature is high enough, it is easy to cut off the connection in the Au film to form Au NPs. For the 50-nm Au film, the Au film is more continuous, but the surface is still rough, as shown in Fig. 3.6

3.2. OPTICALLY INDUCED THERMAL EFFECT: THEORY AND SIMULATION

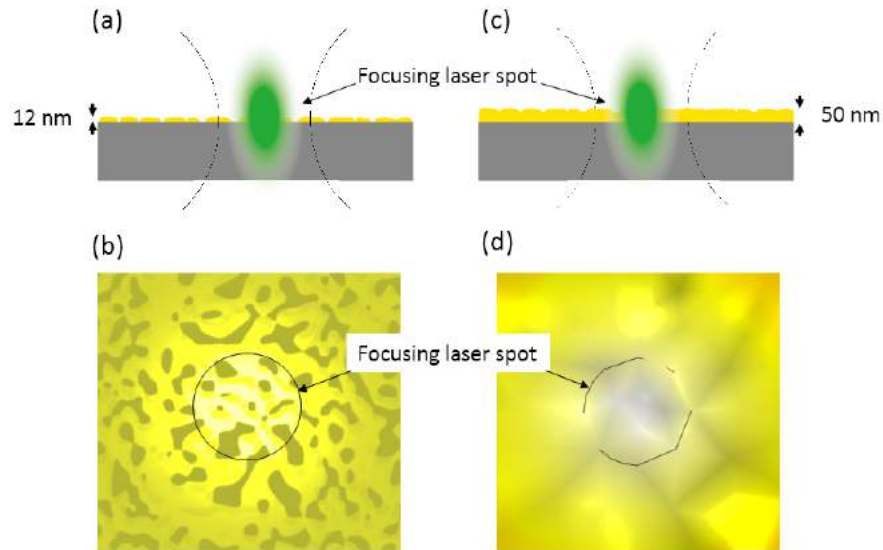


Figure 3.6: *The induced temperature distribution on Au films with 12-nm (a,b) and 50-nm (c,d) thickness. (a) and (c) illustrate the laser focusing, (b) and (d) illustrate the induced thermal effect, respectively.*

(c). The thermal effect at the laser focusing area is continuous, but still not uniform, as shown in Fig. 3.6 (d). When the laser-induced temperature is high enough, the Au material evaporates and forming Au nano-holes. These simulations using Comsol Multiphysics allowed us to understand correctly what happens when a laser beam is focused on the surface of a metallic sample. This suggests a way to realize metallic NHAs by an optical method without needing the use of a polymeric template and a lift-off method. The required laser power was predicted in the range of few milliwatts to dozens milliwatts, which is reasonable with a standard optical system.

3.3 Realization of plasmonic nanostructures by DLW method

3.3.1 Continuous-wave based DLW method

The direct laser writing (DLW) method based on focusing a light beam through a high numerical aperture (NA) objective lens (OL) is a simple and fast approach for plasmonic fabrication. The resolution of a common DLW technique is limited at hundreds of nanometers due to the diffraction limit effect at the focusing spot of the OL [142]. When an incident laser focuses on materials, the absorption effect [143] has two processes called photolytic and photothermal effect [144]. When the laser-induced excitation rate is lower than the thermalization rate, the photothermal effect is significant. So a continuous-wave (CW) laser is suitable for the photothermal process instead of a pulsed laser.

Recently, we have demonstrated a DLW system based on low one-photon absorption (LOPA) in photoresist materials, in which the optically induced thermal effect in the focus area inside the polymer film occurs to form the desired nanostructures. In this work, we demonstrated the use of this DLW to realize on-demand plasmonic nanostructure (PNS).

The DLW set up is described in Fig. 3.7, in which items are connected and each of them takes responsibility for each experimental condition and parameter. The light source used for all fabrications is a CW laser emitting at 532 nm. For Au and Ag, this light source is not really LOPA, but these metallic materials, with a very thin film, simply absorb the light beam and convert to heat. We, therefore, consider this fabrication as a simple OPA-based DLW technique. A combination of a half-wave plate ($\lambda/2$) and a polarizer (P) is employed to control the laser power from a few

3.3. REALIZATION OF PLASMONIC NANOSTRUCTURES BY DLW METHOD

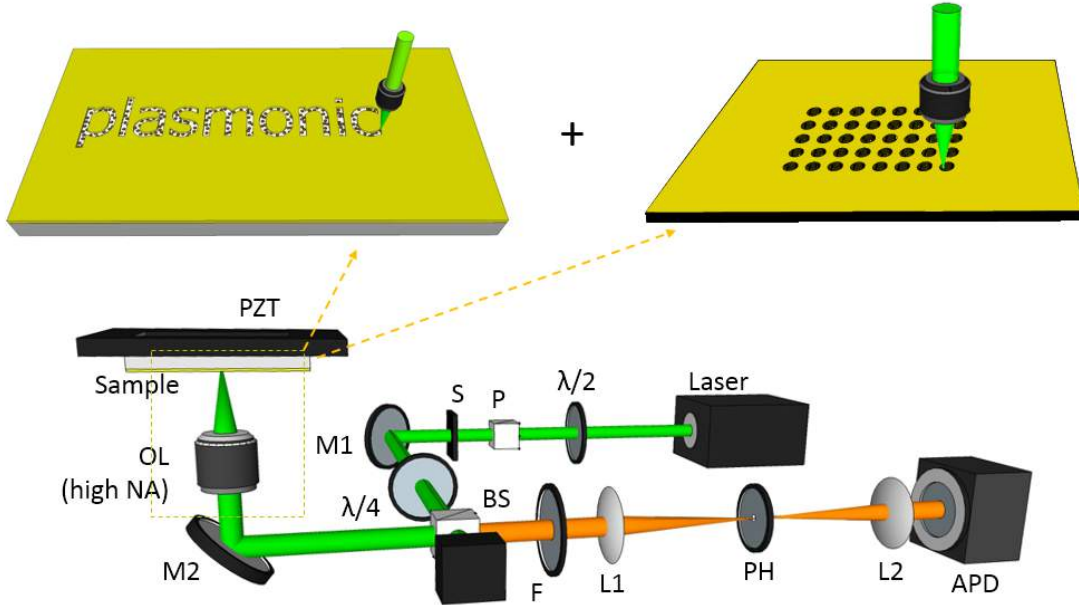


Figure 3.7: *Illustration of the DLW setup used to realize plasmonic nanostructures. $\lambda/2$: half-wave plate; P: polarizer; S, shutter; M1, M2: mirrors; $\lambda/4$: quarter-wave plate; BS: beam splitter; L1, L2: lens; PH: pinhole; APD: avalanche photodiode detector; OL: objective lens; PZT: piezoelectric translator.*

microwatts to 5 W (maximum of the laser power). The electronic shutter (S), which is synchronized with the movement of a piezoelectric translator (PZT), is used to control the exposure time. Then, a quarter-plate ($\lambda/4$) is placed in front of the OL in order to transfer the laser beam from linear polarization to circular polarization, preventing an anisotropy effect in the focus area and ensuring a perfect circular shape of the focusing spot. A high NA (NA=0.9, air immersion) is introduced to focus the laser beam into the sample, which is mounted on the PZT. The focusing spot position is determined by detecting the fluorescence emission of the metallic thin film. We note that at the very thin film, a metallic layer, such as Au and Ag, can absorb 532 nm light and partially convert energy to fluorescence while major part converts to thermal effect. Even the fluorescence signal is weak, but our confocal system still can

3.3. REALIZATION OF PLASMONIC NANOSTRUCTURES BY DLW METHOD

detect this signal thanks to the use of a high sensitive avalanche photodiode detector (APD).

The mechanism of the fabrication technique is to focus a 532 nm CW laser beam on a metallic film. When the laser beam is focused on a metallic film, the high-energy radiation is produced, generating a local temperature, called optically induced thermal effect, exceeding few hundreds of degrees in a short time. This high temperature allows the metallic film to be dewetted forming NPs or to be melted and evaporated forming nanoholes structures. The metallic NPs formed by optically induced local thermal effect is equivalent to the thermal annealing method, presented in chapter 2. Especially, the DLW technique allows metallic NPs to be formed only in the illuminated area, thus by moving the focusing position, plasmonic sub-micro patterns can be created on-demand. Furthermore, by using higher laser power, this DLW allows creating nanoholes in a thick metallic film. This enables a direct fabrication of plasmonic NHAs, for the first time by DLW method, without using a polymeric template and a lift-off method.

Technically, the combination of Matlab and Labview is used to obtain the writing trace of desired structures. First, the trace of the desired structure is calculated by Matlab, which records the position of each point or the beginning of the point and corresponding distance of writing direction. Then, this data is loaded by the Labview program, which controls the PZT's movement through the point-to-point method or scanning velocity method. With a suitable laser power, by controlling the writing trace linked with the shutter (S), the desired plasmonic patterns consisted of metallic NPs or NHAs can be obtained.

3.3.2 Realization of Au and Ag NPs

The Au film sample is prepared by using an Emitech K650 magnetron sputter on a glass substrate as shown in chapter 2. The thickness of the Au layer is about 12 nm, as measured by the Dektak profilometer. We have first scanned the sample line by line with a distance of 500 nm to form an area of 5×5 (μm^2) of Au NPs. The fabricated samples can be checked by eye, with a change of color, and also with an optical microscope and an electron scanning microscope (SEM).

The result obtained by the transmission microscope is shown in Fig. 3.8 (a). In this sample, different areas were obtained by changing the laser exposure dose with different laser powers and different scanning speeds. The vertical-direction indicates the patterns obtained with different laser powers, changing from strong to weak (38 mW - 2 mW) and the horizontal-direction indicates the patterns obtained with various scanning speeds ranging from 1 $\mu\text{m}/\text{s}$ to 40 $\mu\text{m}/\text{s}$, respectively. From these optical microscopes images, we can see that the sample color gradually changes with the laser exposure dose, from dark red to yellow, then to green. Figure 3.8 (b) shows an SEM image of the original Au film. We can see that the Au film is not uniform but consists of discontinuous random lines. In contrast, the SEM image shown in Fig. 3.8 (c) corresponding to the color yellow, confirms that the NPs are formed. The shape of the NPs like the islands, which can also be called the Au nano-islands (NIs). Moreover, the absorption spectra of fabricated small samples are measured and compared with the results obtained before fabrication showing a strong plasmonic resonant peak at around 550 nm. This result is consistent with those obtained by annealing in the oven, shown in chapter 2.

We have then demonstrated the advantages of the DLW method to fabricate many other Au NPs based plasmonic structures, with controllable colors and also sizes and

3.3. REALIZATION OF PLASMONIC NANOSTRUCTURES BY DLW METHOD

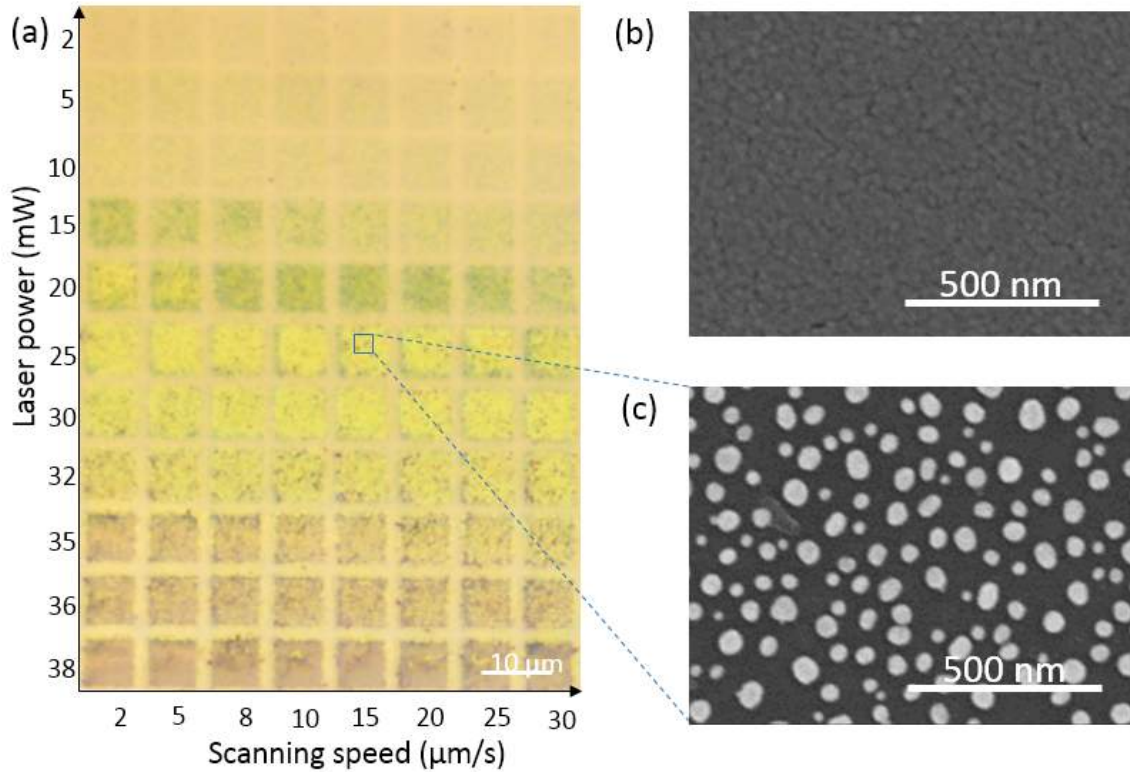


Figure 3.8: (a) Optical microscope images of Au NPs written by different laser powers and different scanning speeds. (b) SEM image of Au film before DLW. (c) SEM image of fabricated Au NIs in the yellow area.

shapes. These fabricated structures are very interesting for many applications, which were partially demonstrated and will be presented in chapter 4.

Similar to that, we also performed the fabrication of plasmonic structures using Ag thin film. The Ag layer is prepared by the evaporation method as explained in chapter 2. The metallic layer of the evaporation method is more uniform and has a higher density than that obtained by the deposition method. The thickness of Ag film is about 8 nm as the best thickness for fabrication of Ag NPs. The fabrication process of Ag NPs is the same as the formation of Au NPs, whose size can be controlled by adjusting the laser exposure dose and the scanning speed. We should note that the

3.3. REALIZATION OF PLASMONIC NANOSTRUCTURES BY DLW METHOD

color of Ag material is white when the Ag film is thicker, i.e. this material does not absorb at 532 nm. However, at a thickness of 8 nm, the Ag film (also Au film) shows a grey color, and this film absorbs strongly 532 nm laser beam.

We experimentally found that the temperature of transferring Ag film to Ag NPs is weaker than that of Au film, as explained in the simulation part. Therefore, the laser power used to form Ag NPs is lower than that required to form Au NPs, by using the same optical system.

The formation of Ag NPs can be clearly seen in Fig. 3.9 in term of color and corresponding SEM image. In this case, we also changed the laser exposure dose (power, exposure time, scanning speed, or distance between scanning lines) to change Ag NPs sizes. Therefore, the color of Ag NPs samples in the optical microscope changes from the natural color of Ag substrate to yellow, then gradually changes from blue to dark blue, thanks to different sizes and distribution of Ag NPs. Look closely at Fig. 3.9 (a), a laser power of 10 mW starts to transform a continuous Ag film into separated tiny Ag NPs. As the laser power increases to a higher value of 30 mW, Ag NPs become clearer and their sizes reach to about 50 nm (an average value with a variation of about ± 25 nm), which was calculated from the SEM image shown in Fig. 3.9 (b). This result shows the dependence of plasmonic effect (color) on the laser power, indicating that the size and distribution of Ag NPs play a vital role in the plasmonic effect of written samples.

Technically, there are three parameters to adjust the exposure doses in the focus area: writing speed or exposure time, period or distance between two scanning lines, and the laser power or laser intensity. For the scanning speed, the high scanning speed means the less time laser exposed in the same area, hence, the saturation is faded as speed becomes faster. This phenomenon occurs due to the fact that longer exposure time leads to a more uniform heat distribution around the focusing spot.

3.3. REALIZATION OF PLASMONIC NANOSTRUCTURES BY DLW METHOD

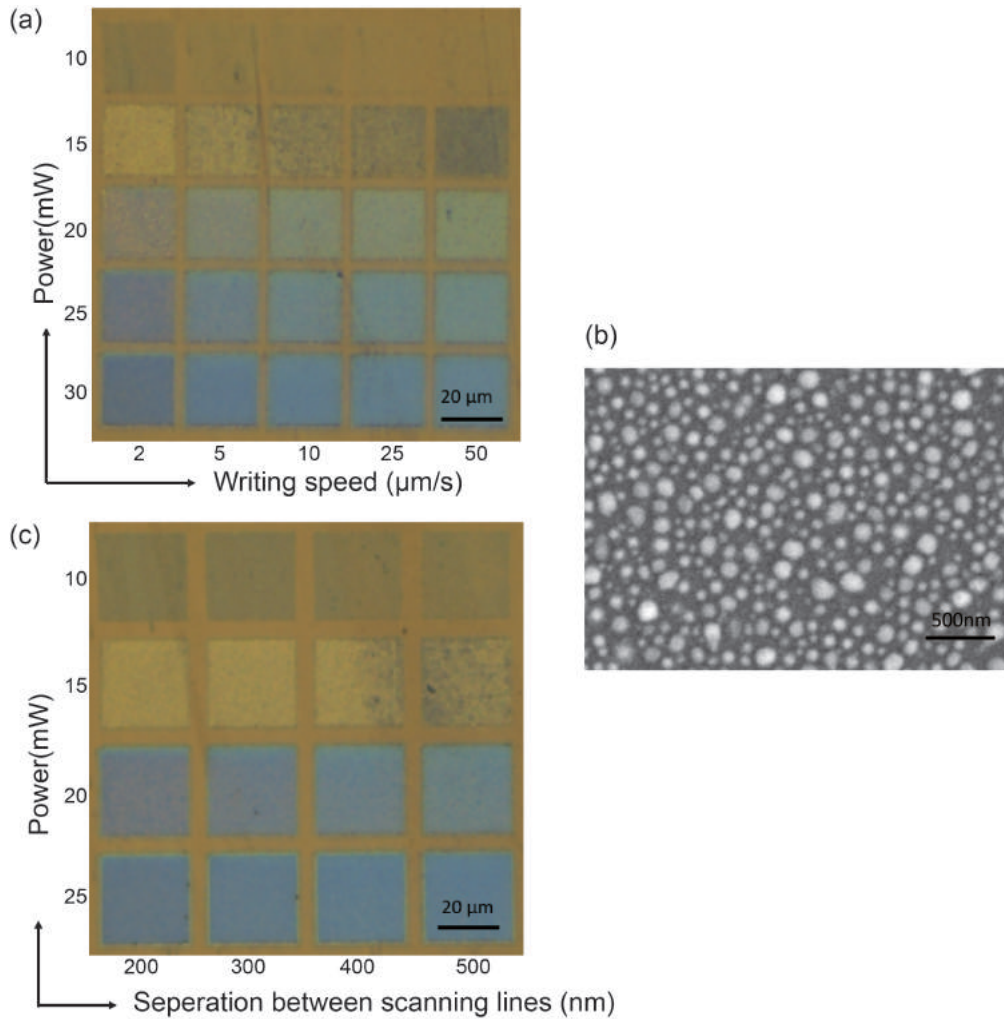


Figure 3.9: (a) Ag NPs fabricated by the DLW method with different writing speeds and laser powers. (b) Typical SEM image of Ag NPs in the blue area. (c) Ag NPs fabricated by the DLW method with different separations between scanning lines and different laser powers.

Aside from that, Ag NPs created with different separations between two scanning lines show a little change in the resulting color, as shown in figure 3.9 (c). That is because the OL used allows focusing the laser beam to a small spot of about 250 nm, which is already very small comparing to the distance between two scanning lines. The thermal effect makes the induced hot spot with a size larger than 250 nm. By changing the separation between lines or between focusing spots, the dose is then

3.3. REALIZATION OF PLASMONIC NANOSTRUCTURES BY DLW METHOD

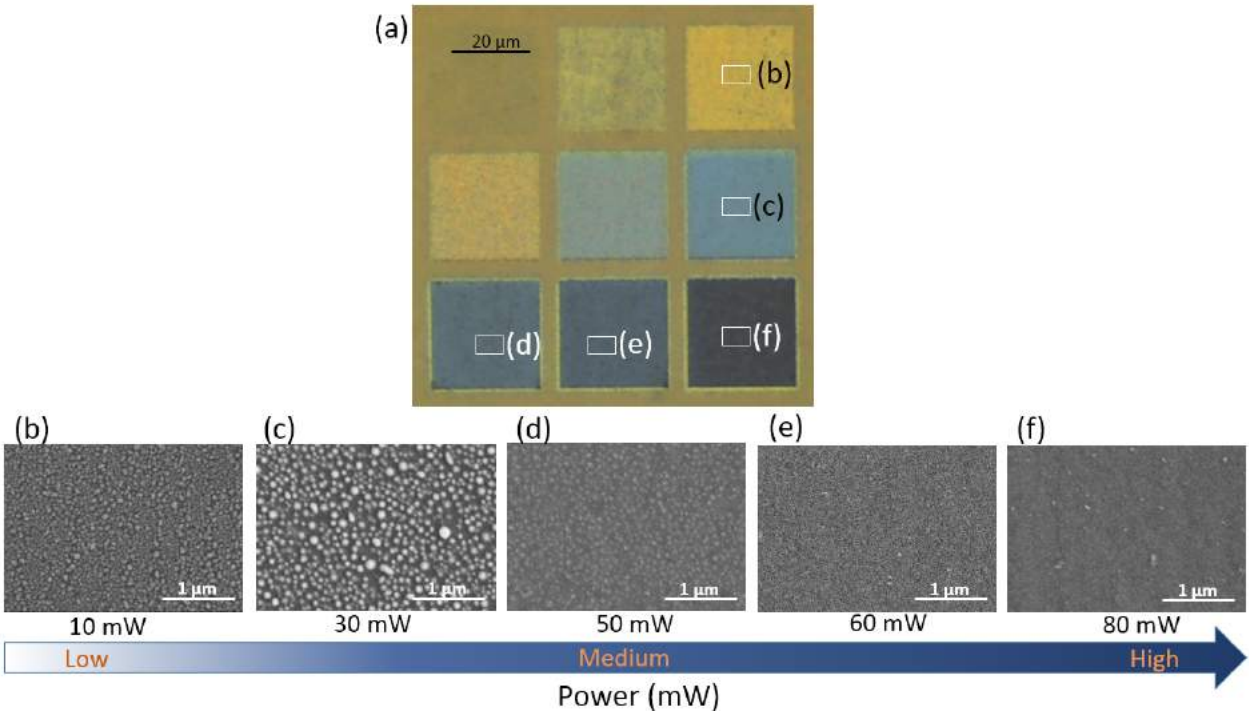


Figure 3.10: (a) Optical microscope image of Ag NPs samples fabricated by various exposure powers. Laser power from top left to bottom right: 5, 8, 10, 15, 20, 30, 50, 60 and 80 mW, respectively. (b-f) SEM images of Ag NPs obtained by different laser powers: 10, 30, 50, 60 and 80 mW, respectively.

changed, resulting in different Ag NPs sizes. However, we found that exposure time and period cannot be perceived as vital factors in creating Ag NPs samples that have distinguishable plasmonic effects. We may conclude that the laser power is the key parameter to change the size of Ag NPs, thus alter the plasmonic effect.

Then, we fixed the scanning speed and the distance between two scanning lines and varied the laser power. Figure 3.10 (a) illustrates the optical microscope image of color-changing by applying different laser powers: 2.5, 5, 10, 15, 20, 30, 50, 60, and 80 mW, respectively. For this result, the scanning speed is chosen as 5 $\mu\text{m/s}$ and the distance between scanning lines is 500 nm. The corresponding SEM images are shown in Fig. 3.10 (b-f). This suggests that the laser powers ranging from 10 mW

3.3. REALIZATION OF PLASMONIC NANOSTRUCTURES BY DLW METHOD

to 30 mW are optimum for the creation of Ag NPs by the DLW method. When the power is increased to 50 mW, the micro explosion phenomenon tends to happen, i.e. big Ag particles are exploded into very tiny particles. When the laser power reaches 80 mW, the Ag NPs are totally exploded, it's too small to be seen, or even totally evaporated, and only the substrate remains.

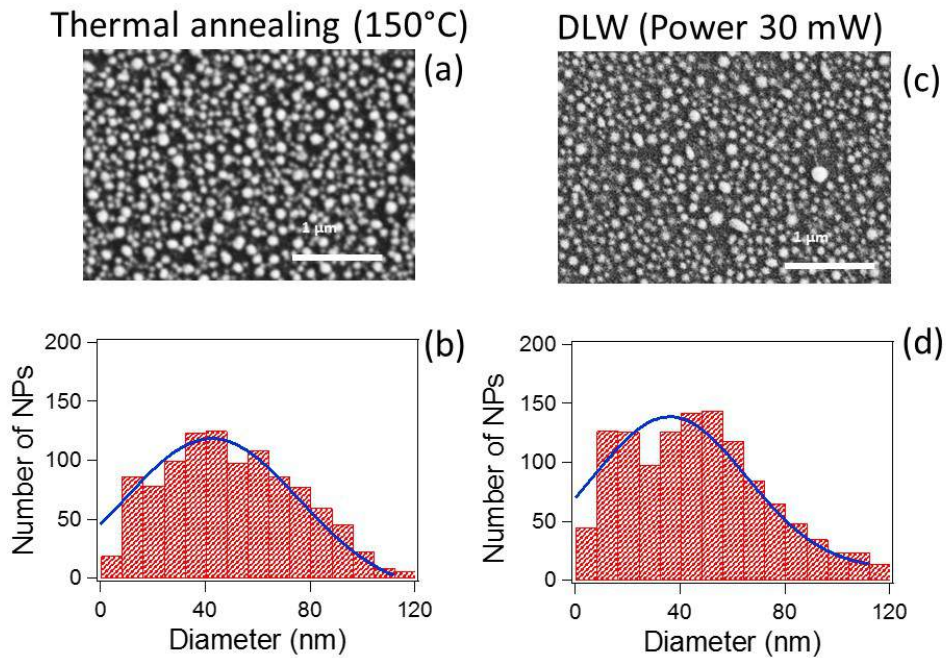


Figure 3.11: Comparison of Ag NPs fabricated by oven annealing and DLW methods. Ag NPs are obtained by (a-b) oven annealing at 150 °C and with 30 s duration, and (c-d) DLW method with a laser power of 30 mW, a scanning speed of 5 μm/s and a scanning period of 0.5 μm.

Since Ag NPs can be fabricated by the thermal annealing method and DLW method, we evaluate the equivalence of these two techniques by analyzing corresponding SEM images and size distribution of Ag NPs. Figure 3.11 illustrates the size distribution of Ag NPs created by thermal annealing method at 150 °C and with 30 s duration, and the size distribution of Ag NPs fabricated by DLW method with a laser power of 30 mW, a scanning speed of 5 μm/s and a scanning period of 0.5

3.3. REALIZATION OF PLASMONIC NANOSTRUCTURES BY DLW METHOD

μm . The two results are quite similar so that we can conclude that the optically induced temperature can reach very high and can be optically controlled. The great advantage is that, by using the DLW method, we can obtain desired patterns which is very interesting for many applications as it will be shown in the next chapter.

3.3.3 Realization of plasmonic nanostructure with metallic NPs

As mentioned before, the size of the focusing point is hundreds of nanometers because of the diffraction limit, which is much bigger than the size of metallic NPs. Thus, the small-period structure of PNS with single Au or Ag NPs inside is difficult to obtain. Besides, we also saw that the metallic NPs were totally evaporated with high laser power, e.g. 80 mW for Ag NPs. In this section, we propose to control the laser power and study the influence of separation between two scanning lines for the fabrication of 1D PNS containing multiple Au NPs.

To obtain 1D structure formed by Au NPs, we first investigated the Au NPs formed under a high laser power of 50 mW. With this laser power, the induced temperature is very high, resulting in a large thermal spot that form the Au NPs in a very large area, larger than the diffraction limited spot. Figure 3.12 (a) illustrate the 1D nanostructure lines of Au NPs separated by the Au film whose period is $2 \mu\text{m}$. Because the heat transfer curve has a greater width than the laser scanning area, the width of the Au NPs line is very large ($> 1 \mu\text{m}$). While decreasing the period to $1.2 \mu\text{m}$, all the Au film between the writing lines is transferred to form NPs, the 1D period structure is disappeared and all the writing area covered with Au NPs, as shown in Fig. 3.12 (b). When the laser writing period getting smaller, the 1D structure appears again. This 1D structure is made by Au NPs and blank space, where the next line writing is directly on the already formed NPs, making these NPs evaporated. The results obtained with a scanning period of $0.6 \mu\text{m}$ is shown in Fig. 3.12 (c).

3.3. REALIZATION OF PLASMONIC NANOSTRUCTURES BY DLW METHOD

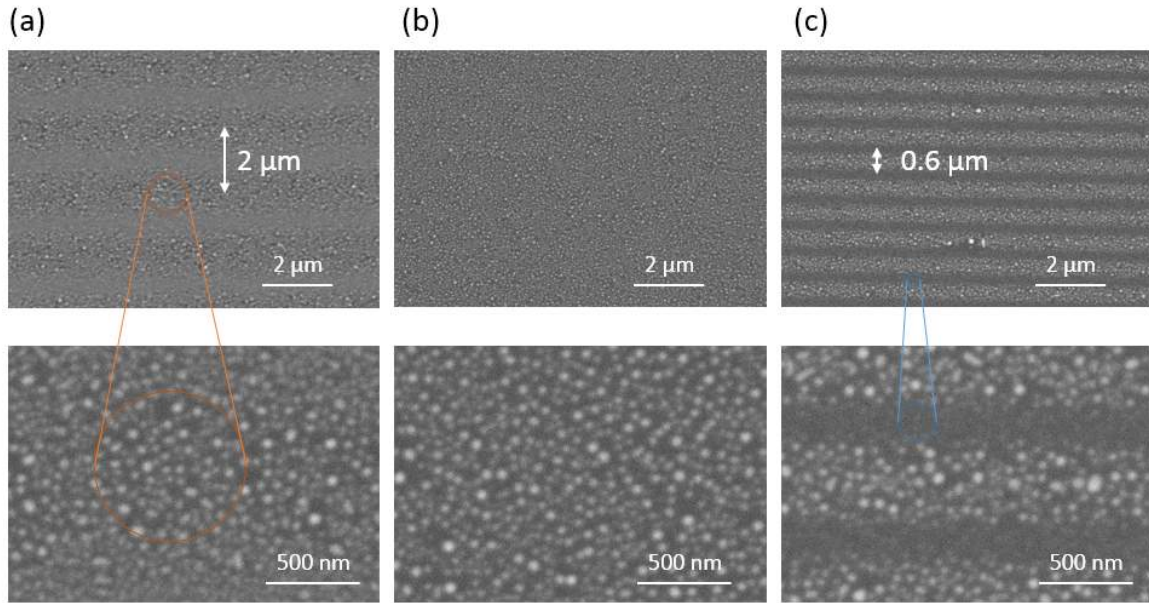


Figure 3.12: SEM images of 1D PNS formed by Au NPs of different periods: (a) $2 \mu\text{m}$, (b) $1.2 \mu\text{m}$, (c) $0.6 \mu\text{m}$. The laser power is 50 mW which can both form the Au NPs from 12-nm Au film and explode them with the second writing.

That can be also explained by the fact that when Au NPs already formed, the optically induced thermal effect is stronger, resulting in a higher induced temperature. Therefore the second writing, even with the same laser power, on the already formed NPs will easily evaporate these NPs. Then, we proposed a simple and rapid method to obtain this kind of 1D PNS of Au NPs by using a two-step fabrication method. First, a large area of Au NPs surface is obtained by the oven annealing method. Then, DLW on this sample of Au NPs can form the 1D structure with a smaller period.

The two-step results are shown in Fig. 3.13. The Au NPs are removed during the DLW process resulting in an air line. A stable periodic 1D structure is then obtained, where the lines of the Au NPs consist of 1 or 2 Au NPs as shown in the enlarged image in Fig. 3.13 (b). When the period reached 300 nm, which is close to the diffraction limit of the OL, only few NPs remain, the 1D structure still can be seen but not clear,

3.3. REALIZATION OF PLASMONIC NANOSTRUCTURES BY DLW METHOD

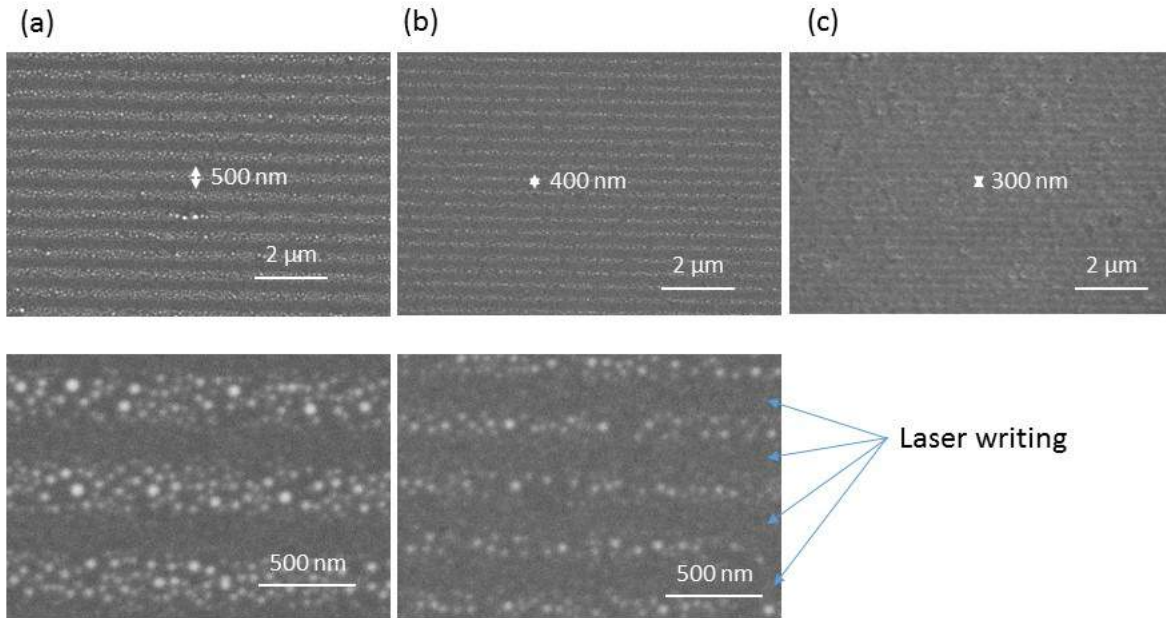


Figure 3.13: SEM images of 1D structures of Au NPs fabricated by two-step writing. The first step is the fabrication of the Au NPs by thermal annealing method in the oven. The second step is to perform DLW on the Au NPs sample with a laser power of 50 mW. (a-c) illustrate the period of 500 nm, 400 nm, and 300 nm, respectively.

as shown in Fig. 3.13 (c).

With this two-step method, we confirmed that the 1D structure of Au NPs with 400 nm period is reliable, which is very useful for potential applications, such as distributed feedback (DFB) laser, or plasmonic color printer.

3.3.4 Demonstration of direct fabrication of nanoholes arrays

We proposed in this section to show the results of different 2D plasmonic structures, fabricated by a direct method. The thickness of the Au layer is set to 50 nm and the laser power is chosen to be 160 mW. For such thick Au film, a higher laser power is required in order to induce a strong thermal effect, which can evaporate the thick Au film. Figure 3.14 shows the SEM images of fabricated Au NHAs of square and

3.3. REALIZATION OF PLASMONIC NANOSTRUCTURES BY DLW METHOD

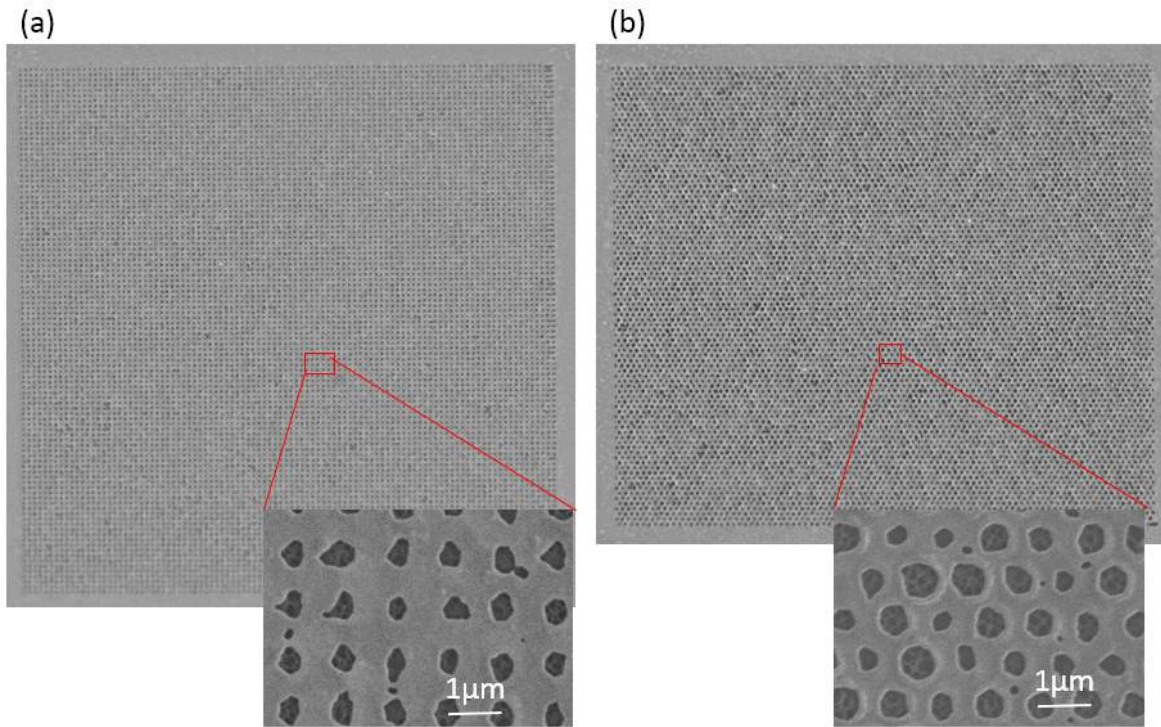


Figure 3.14: SEM images of $100 \times 100 \mu\text{m}$ square configuration (a) and $100 \times 86 \mu\text{m}$ hexagon configuration (b) of Au NHA. Inserts are the enlarged images.

hexagon configurations. The periods of square and hexagonal structures are $1 \mu\text{m}$ and $1.1 \mu\text{m}$, respectively. The focusing laser beam allowed totally evaporation of Au material, resulting in a submicro hole. The shape of the holes is random, which is due to the non-uniformity of the surface of the Au film as explained before. Together with the optically induced thermal effect, this evaporates non-uniformly the Au material, which is consistent with the simulation results shown in Fig. 3.5 (d).

Note that, we also tried to fabricate the Ag NHA. Unfortunately, not like the simulation results, which shows that with a laser power of 60 mW, one can obtain the Ag NHA. We don't obtain any structure with the Ag film even the laser power is increased up to 400 mW, which is much higher than that required for Au film. This can be explained by the fact that when the thickness of Ag film becomes important

3.3. REALIZATION OF PLASMONIC NANOSTRUCTURES BY DLW METHOD

(more than 30 nm in the experiment), the Ag film behaves like a mirror. All the light is reflected at the interface, and it has very low, even no absorption. This is of course not like when the thickness of Ag is very thin (8 nm), for which Ag still absorbed strongly light at 532 nm. Different solutions are proposed for patterning Ag NHAs, for example, using a laser wavelength in the UV domain, or covering Ag film with an absorbing material at 532 nm. We have tried the last solution by spin-coating a SU8 photoresist doped RhB on the top of the Ag film. We expected that RhB will absorb strongly 532 nm laser beam and induce a hot spot on the top of Ag film, which can, therefore, evaporate Ag material. Unfortunately, after many tests, Ag still exists and SU8/RhB becomes just solid on the top of Ag film. We think that it should be possible to obtain Ag NHAs by using a UV laser beam, but it is out of the scope of this thesis work.

We now tried to study theoretically if the plasmonic NHA fabricated by our method possesses a good plasmonic property as those obtained by other standard methods. We first simulated the plasmonic properties of ideal NHAs, i.e. with perfect circular holes, then simulated and compared with the results of real structures fabricated by our method. The FDTD simulations of an ideal model of Au NHA with a period of 1 μm are illustrated in Fig. 3.15. We first fixed the diameter of the Au NHA to 400 nm, and changed the thickness of the Au film from 10 nm to 90 nm (Fig. 3.15 (a)). Figure 3.15 (c) shows that the corresponding transmission spectra. Usually, the suitable thickness is fixed as 50 nm for the best plasmonic property. By this simulation, with 50 nm thickness, we confirmed that Au NHA possesses an extraordinary transmission peak at about 1550 nm. That is very interesting for applications such as a bandpass filter.

We then fixed the thickness of Au at 50 nm and changed the diameter of the Au holes (see Fig.3.15 (b)). Figure 3.15 (d) shows the dependence of plasmonic resonance

3.3. REALIZATION OF PLASMONIC NANOSTRUCTURES BY DLW METHOD

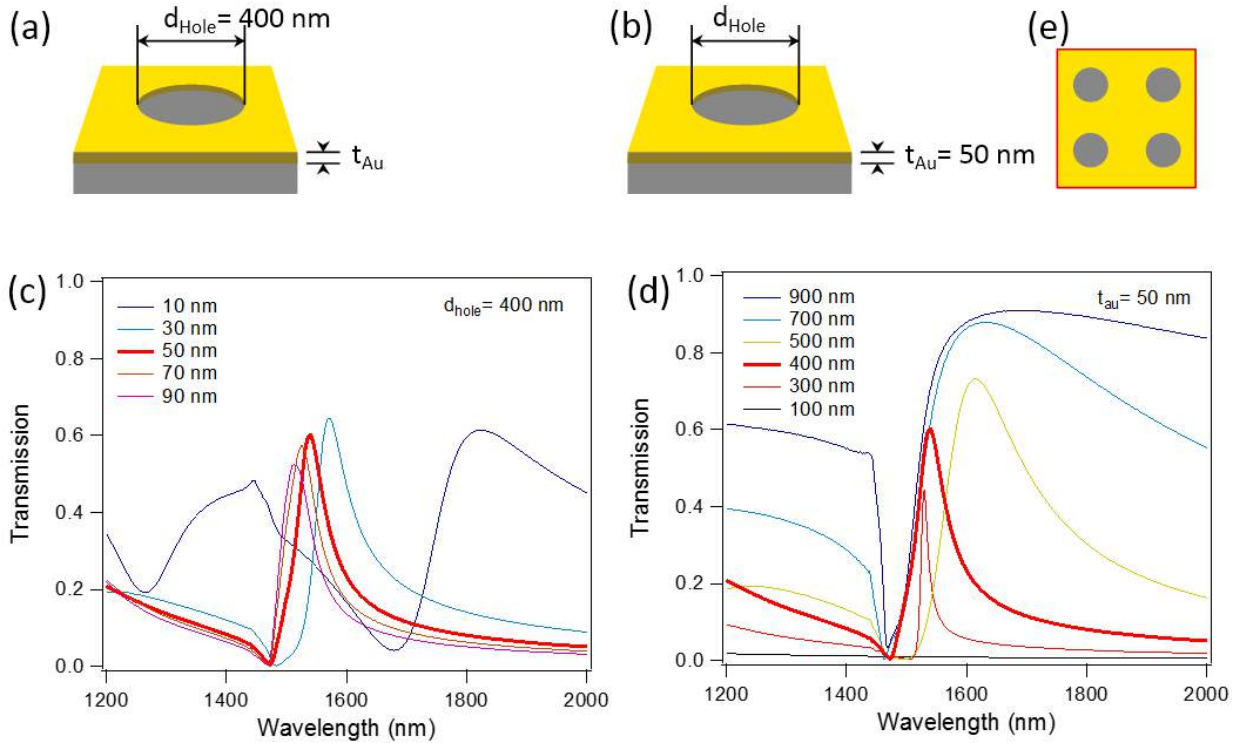


Figure 3.15: *The FDTD simulations of Au NHA. Illustrations of squared pattern with fixed hole size (a) and thickness of the Au film (b), respectively. Transmission spectra of different thicknesses (c) and different diameters of NHA (d). (e) shows the simulation area.*

of NHA on the diameter of the Au holes. The best result is obtained with 400 nm diameter and 50 nm thickness, for which it has a narrow peak and high transmission.

We also did a similar simulation for hexagonal patterns, as shown in Fig. 3.16. With a period of $1 \mu\text{m}$, the best transmission peak appears around the wavelength of 1450 nm. The transmission peak blue shift with the thicker film (Fig. 3.16 (c)), which has the same trend as the squared one. And for the same thickness of 50 nm, the transmission peak becomes redshift and wider when the diameter of the nanoholes increased (Fig. 3.16 (d)).

We then performed the simulations using real NHAs (square and hexagonal) and

3.3. REALIZATION OF PLASMONIC NANOSTRUCTURES BY DLW METHOD

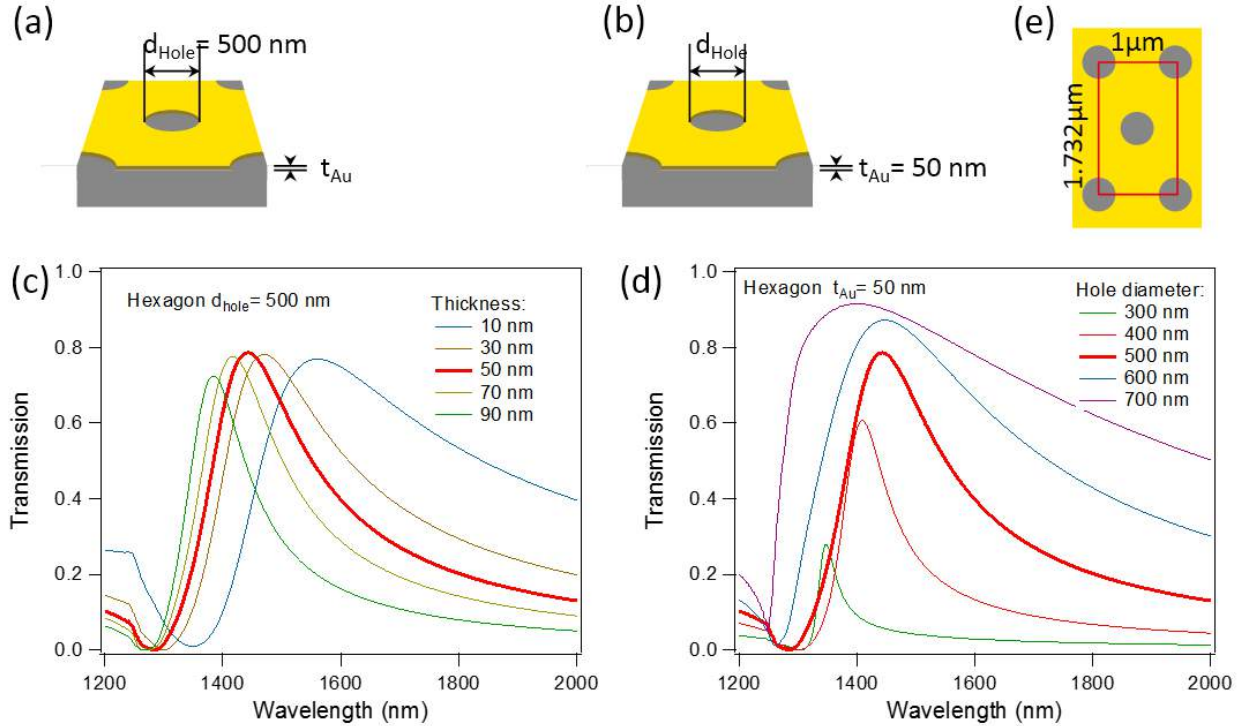


Figure 3.16: *FDTD simulations of Au NHA of hexagon pattern. Simulation models with a fixed hole size (a) and thickness (b), respectively. (c-d) Transmission spectra of Au NHAs having different thicknesses and different diameters. (e) shows the simulation area.*

compared them with the results of ideal ones. Figure 3.17 (a) illustrates the simulation results of the transmission spectrum of the real image of the square pattern, and corresponding results of the ideal model. For the real structure, the size and shape of the hole vary from this hole to others. We adopted the one having the diameter of an average hole around 500 nm to do simulations and compared the results with those obtained ideal one having the same diameter of 500 nm. These matched results show that even the shape of real NHA is not circular, they have the same transmission results. This means that the transmission spectra depends on the period and the average size of NHA, and not on the shape of every nanohole. This is similar to the result of plasmonic resonance of metallic NPs shown in chapter 2, for which the

3.3. REALIZATION OF PLASMONIC NANOSTRUCTURES BY DLW METHOD

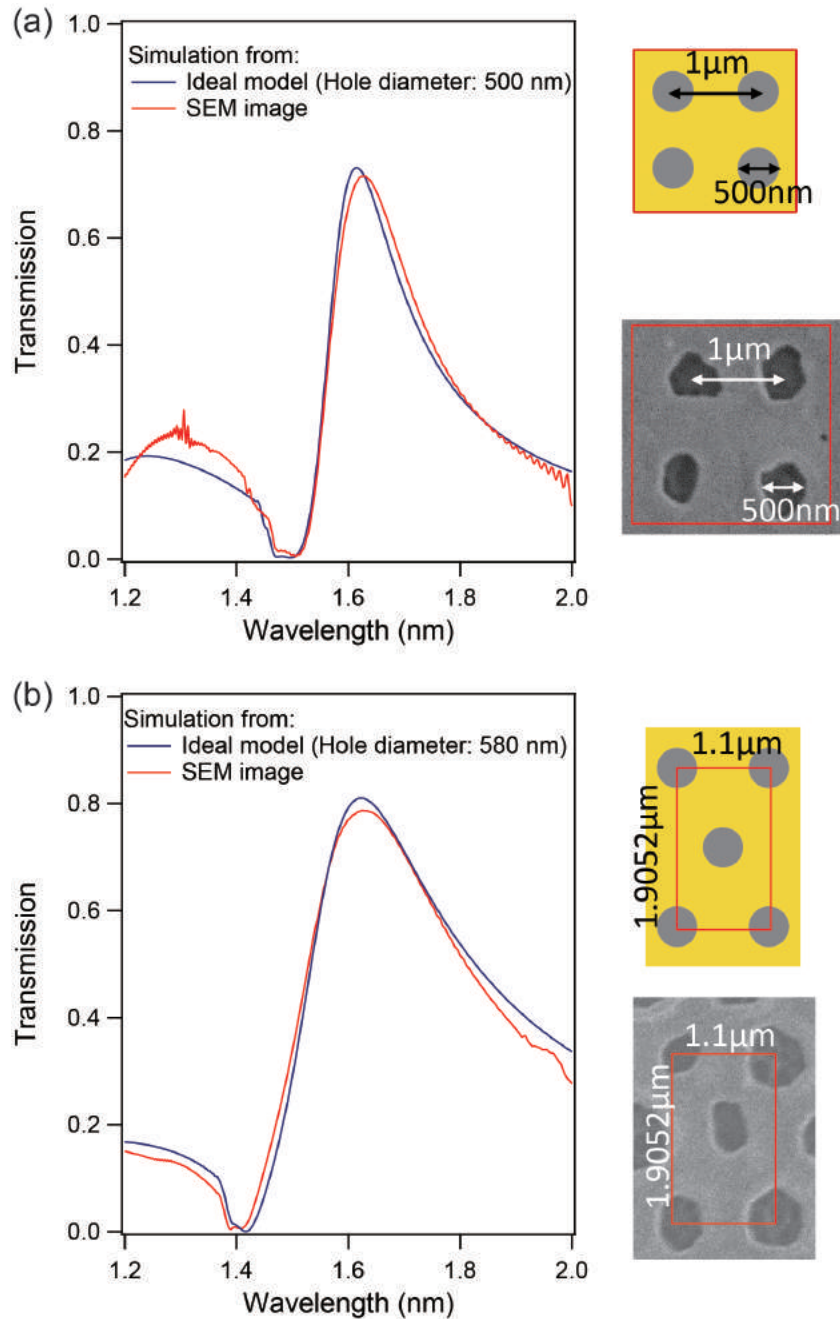


Figure 3.17: Comparison of transmission spectra of an ideal model and a real fabricated structure. (a) Results of a square NHA having a period of 1 μm . (b) Results of a hexagonal NHA having a period of 1.1 μm .

resonance spectra also depend on the average size of metallic NPs instead of the shape of each NP. Similar simulations have been also done for hexagonal structures. For this

3.3. REALIZATION OF PLASMONIC NANOSTRUCTURES BY DLW METHOD

real NHA, the size of the holes is varied between 500 and 600 nm. To match the results of the simulations, the diameter of 580 nm of the ideal model is assumed of which the transmission spectra is matched to the result from the real one, as shown in Fig. 3.17 (b).

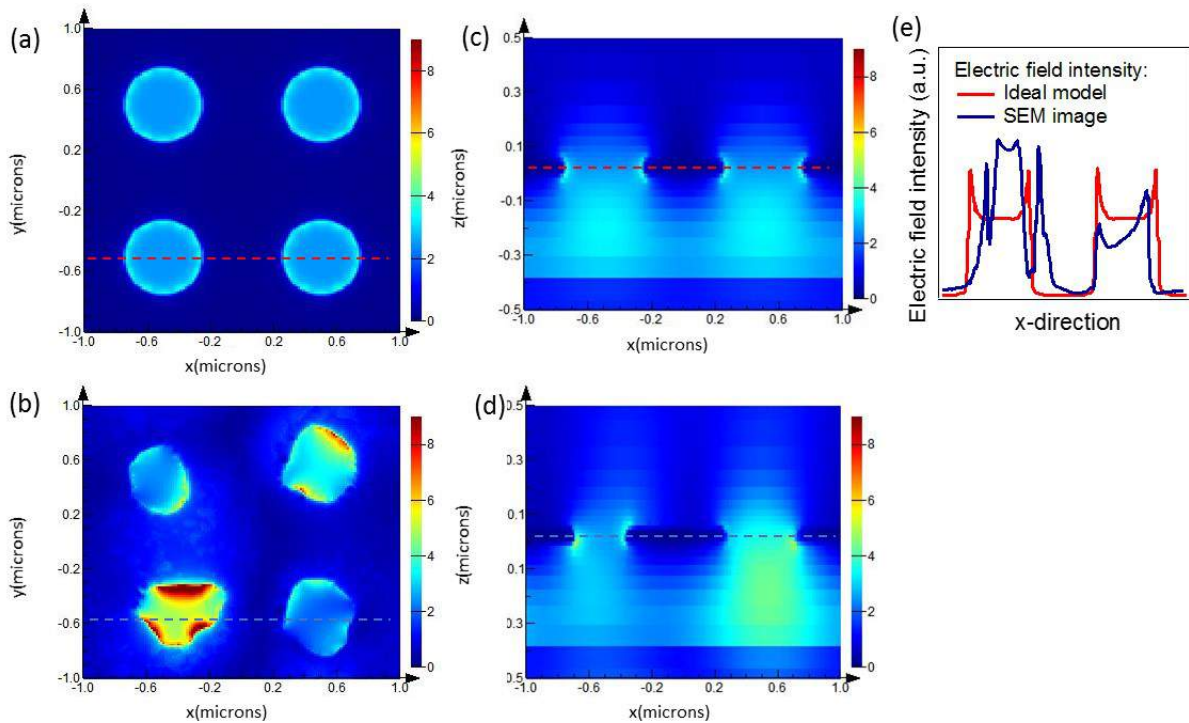


Figure 3.18: *Simulation of electric field distribution of Au NHA. (a),(c): Electric field distributions in the ideal model. (b),(d): Electric field distributions in the real structure. (e) Comparison of the electric field intensity corresponding to the dot lines in ideal and real structures.*

To further compare the ideal model with the experimental results, we did the simulation of electric field distribution around the nanohole of NHAs. Figure 3.18 (a) shows the electric field distribution in the $x-y$ plane of the Au nanohole, and Fig. 3.18 (c) shows the electric field distribution in the $y-z$ plane of an ideal NHA. In the real situation, the nanohole has a random shape. To do simulations, an SEM image of Au NHA obtained by the DLW method is imported to the simulation program. Figure

3.18 (b) and (d) show the electric fields in x - y and y - z planes, respectively of this real structure. We can clearly see that the electric field distribution is not uniform in this real structure due to the variation of the Au nanoholes, from this one to the other. The electric field intensities in the position of the nanoholes of ideal structure and real structure are extracted and compared as shown in Fig. 3.18 (e). The electric field distribution inside the real NHA is not uniform for every hole as the ideal one, but the average intensity is equivalent to that of the ideal one. However, the strong field in certain holes of the real NHA suggests that this structure can enhance the light-matter interaction, better than the ideal NHA. This is quite similar to Anderson localization effect in photonic structure and it should be interesting for some applications.

3.4 Conclusion of chapter 3

In this chapter, first, we have theoretically studied the optically induced thermal effect at a small area in a real metallic film. Not like the theoretical calculation of the PDE method by Matlab software, which only can solve the heat equation in an ideal model, we introduced the finite element method by using Comsol software to deal with the rough surface as in the experiment. We studied the induced temperature in the laser focus center as a function of the laser intensity and of the exposure time. It shows that the temperature will reach a stable value after 30 μ s, and the maximum induced temperature linearly changes as a function of the laser intensity. We applied the simulations for both Au and Ag materials. We found that the laser intensity required to obtain the Ag NPs is much lower than that required for Au NPs. The optically induced thermal effect of different thickness, 12 nm and 50 nm, respectively, is studied. For the 12 nm thick film, the high induced temperature is easy to cut off the connection in the metallic film to form the metallic NPs. But for the 50 nm thick film, it can form nano-holes when the localized induced temperature is high enough

3.4. CONCLUSION OF CHAPTER 3

to evaporate the metal. We studied the temperature distribution for a thick metallic film of 50 nm for two cases: perfect uniform and rough surface. With the same laser power, the laser focuses to create a perfect circular temperature spot for a uniform metallic film while in the case of rough surface, the temperature spot is irregular.

Second, we introduced the DLW method to fabricate the Au and Ag NPs and Au NHAs. We explained first the working principle of the system, and then how to combine the Matlab software works with the Labview program. By using this DLW system, we obtained the Au and Ag NPs with different particle sizes by controlling the laser power and the exposure time. The results of color and size changes are consistent with the FDTD simulations in the previous chapter. After that, the fabrication of PNS with Au or Ag NPs is demonstrated. A two-step writing method is suggested to improve the minimum period of the 1D structure, which shows a stable PNS with a minimum period of 400 nm.

Finally, we studied theoretically the optical properties and experimentally the fabrication of the Au NHAs. Two kinds of Au NHA structures, square and hexagon, are obtained on the 50-nm thickness Au layer. In the experiment, the periods of square and hexagonal structures are 1 μm and 1.1 μm , respectively. The experimental nanoholes show irregular shapes, which are consistent with the simulations due to the rough surface of the Au film. Then, the transmission spectrum of Au NHA of these two structures is studied. The high transmission peak appears around 1550 nm for the square structure and at 1450 nm for the hexagonal structure. Since the nanoholes are irregular, the electric field distribution and transmission of NHA are studied and compared to the ideal models. We found that even the electric field distributions of real structure and ideal model are very different at the nanoholes position but the transmission spectra are almost the same. This proved that the plasmonic resonances of Au NHA depend on the nanohole diameter, period, and structure, but not on the

3.4. CONCLUSION OF CHAPTER 3

nanohole's shape. However, the electric field distributions are quite inhomogeneous in real NHA, like Anderson localization. This suggests that these fabricated structures can strongly enhance light-matter interaction when the fluorescent layer is covered this NHA, for example.

Chapter 4

Applications of fabricated plasmonic nanostructures

4.1 Introduction

The plasmonic nanostructure (PNS) allows having many applications in different domains, from physics, to chemistry and biology. In the previous chapters, gold (Au) and silver (Ag) nanoparticles (NPs) have shown the color changes in the transmission or reflection microscope which are related to the different NPs sizes and their distribution, as well as the surrounding environment. Some applications, such as data storage and color printing were already suggested [145, 146].

In this chapter, we demonstrate several applications of fabricated PNS made of metallic NPs. First, we demonstrate the data storage application by showing the binary record, QR code and bar code, and direct text writing. Then, we demonstrate the application of color printing by using Au and Ag NPs with controllable particle sizes. We propose to improve the quality of the data storage method by using the fluorescence enhancement method, which makes plasmonic nanostructure easy to be

recognized. At last, we propose a random laser based on Au NPs, and show the preliminary investigation.

4.2 Data storage

Optical data storage is the use of light to record and to read the information to and from a memory device [147]. Storage can be achieved by using lasers to pattern a surface, such as on a compact disc, or altering the physical properties of a small volume inside a light-sensitive material. Here, we introduce some data storage method: binary recording, bar code, and QR code recording, and direct text writing.

Binary recording

In order to store data by the plasmonic method, the minimum structures should be studied first. Due to the induced thermal effect, the temperature can reach a high value at the focusing spot but also nearby. The metallic NPs can be therefore formed outside the illuminated area. Therefore, in order to generate Au or Ag NPs only in a region within the focus point, parameters such as power and scanning speed should be optimized.

Since our DLW method is similar to those of CDs and DVDs, we used this method to write binary code and compare it with standard CDs and DVDs. Figure 4.1 shows the comparison of a standard CD writing [148] and our plasmonic writing, where the writing PNSs are formed with Au NPs.

Figure 4.2 illustrates the SEM result of the binary writing realized by the DLW method on an Au film. The black dots and lines illustrate the writing area (Au NPs), while the grey part shows the background (Au initial film). The distance between lines is set to $1.4 \mu\text{m}$, and the minimum length of one data is set to $0.7 \mu\text{m}$. That

4.2. DATA STORAGE

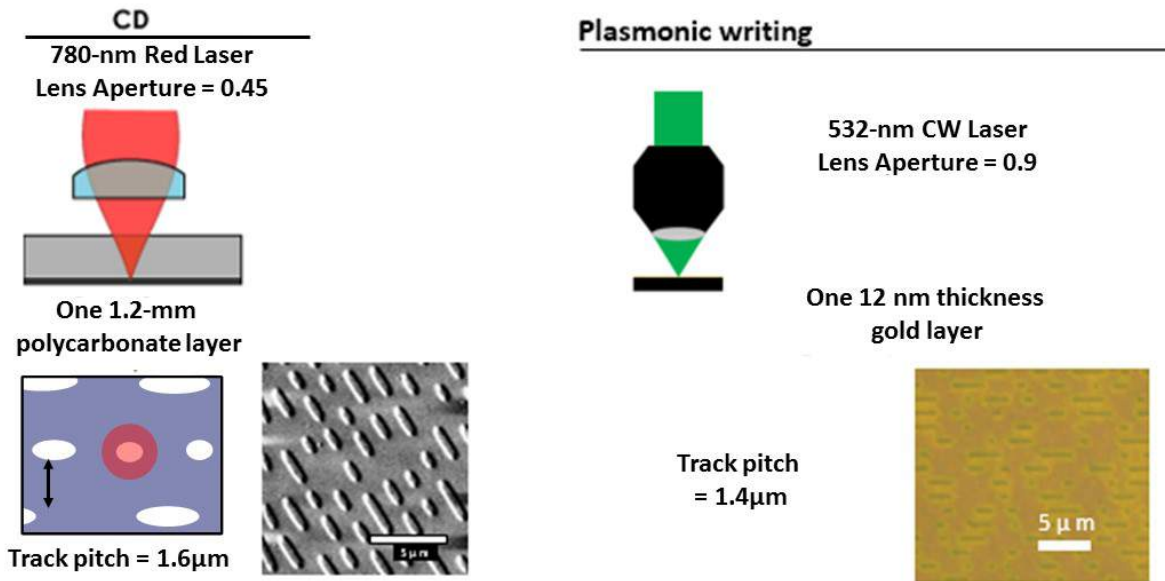


Figure 4.1: Comparison of a standard CD writing [148] and the DLW of PNS with Au NPs.

is due to the resolution of the used DLW system and also of the limited resolution of the optical microscope used to image the fabricated structures.

Table 4.1 shows the comparison of characteristics of the standard CD, DVD and this plasmonic writing with Au NPs. The capacity of the plasmonic writing is calculated to be 914 Mb for this example, which is better than that of a standard CD but less good than the capacity of a standard DVD. To enlarge the capacity of plasmonic writing, we need to make the period smaller. For this moment, the width of the writing is $0.7 \mu\text{m}$ for 12-nm Au film, where the Au NPs are formed inside. As explained before, due to the thermal effect, the NPs can be formed even outside of the focusing spot. Therefore, we should minimize this thermal factor to limit the formation of metallic NPs only inside the diffracted limit area of the focusing. Besides, we can also improve the light focusing spot size by using shorter wavelength and increasing the numerical aperture of the objective lens. If it is possible to create only one or two NP

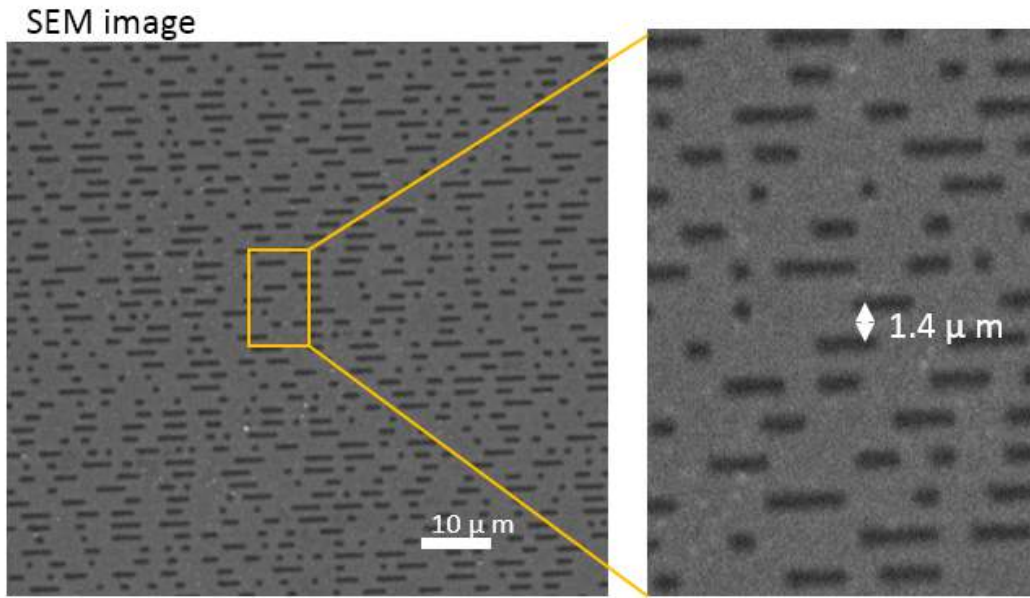


Figure 4.2: *SEM image of binary writing with the DLW method, the period is 1.4 μm .*

for a bit, this plasmonics-based data storage will have a good position as compared with DVD and blue-ray disks.

Bar code and QR code recording

Bar code (1D) is a fast, easy, and accurate data storage method enabling products to be tracked efficiently and accurately. Nowadays, with the help of embedded camera

	CD	DVD	Plasmonic writing
Capacity of the disk	700 MB	4.7 GB	914 MB
Wavelength of the writing laser	780 nm	650 nm	532 nm
Track pitch	1.6 μm	0.74 μm	1.4 μm
Min pit length	0.8 μm	0.4 μm	0.7 μm
Density	0.41 Gb/in ²	2.77 Gb/in ²	0.53 Gb/in ²
Recording materials	Dye layer	Dye layer	Gold layer
Numerical aperture (NA)	0.45	0.65	0.9

Table 4.1: Comparison of the similarities and differences between plasmonic writing with Au NPs, CDs and DVDs.

4.2. DATA STORAGE

devices of smart mobile phones, capturing bar code with their cameras and decoding them with software running on the phone become more and more popular. Besides, QR code (2D bar code) began to attract more attention in e-commerce because QR code not only provides a simple and inexpensive method to present diverse commerce data but also improves mobile user experience by convenient and easy operation. Nowadays, bar code and QR code are realized in millimeter size, which is easy to make fake products. Here we propose to realize these codes at microscale and in that way, “normal” people cannot copy and reproduce it.

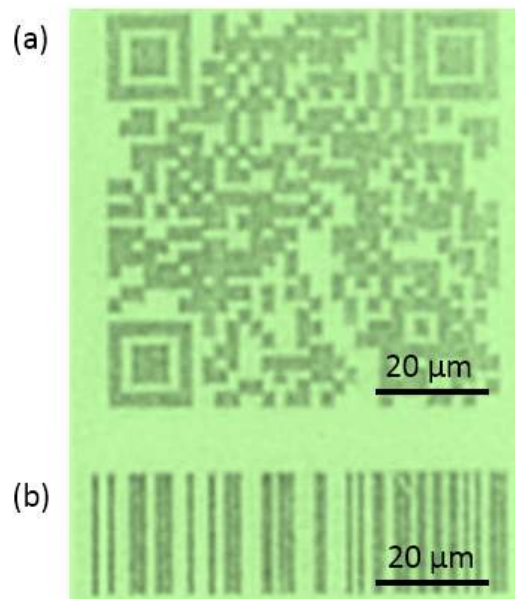


Figure 4.3: *Optical images of (a) QR code made on Au film by DLW method, which links to the website of the author’s laboratory and (b) an example of bar code.*

Figure 4.3 illustrates the realization of a QR code, which links to the website of our laboratory, and a bar code, respectively. The size of the QR code is 70×70 (μm^2). Observing and identifying it requires an optical microscope with a magnification of at least 400 times and a smartphone with a decoding software. For fabrication of these

4.2. DATA STORAGE

plasmonic structures, the laser power was 30 mW and the focusing spot is scanned with a speed of $100 \mu\text{m/s}$. The Au NPs were formed in the focus area, and the line width was estimated to be $0.7 \mu\text{m}$ from the SEM image. For testing, you can use your smartphone to scan the 2D image shown in Fig. 4.3 (a) to reach the website of our laboratory. This suggests a lot of potential applications in marking the objects at micro-scale, such as recording, tracking, and recognizing the micro-devices, and for high security.

Direct text writing

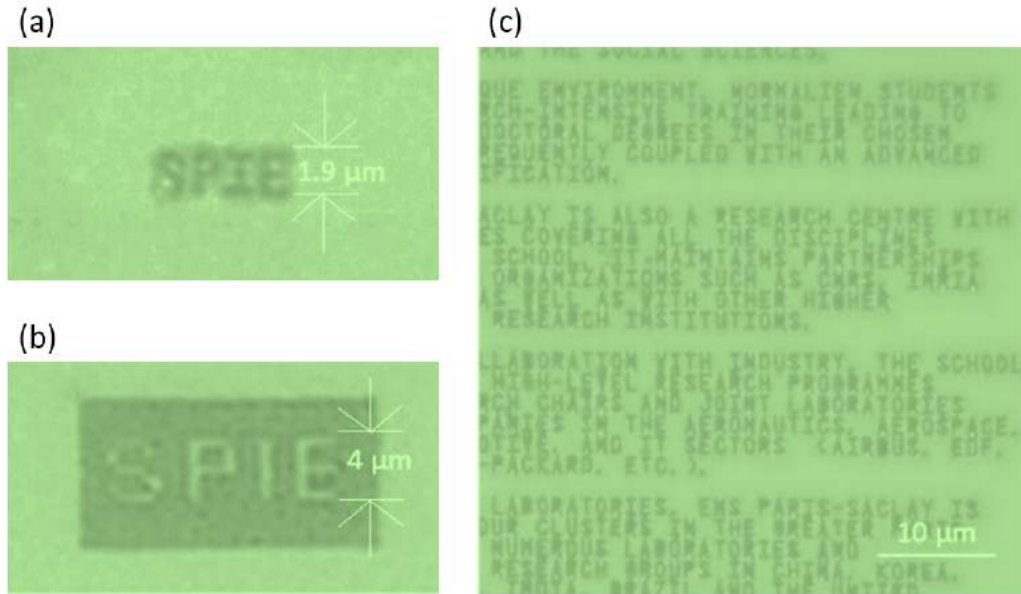


Figure 4.4: (a) Direct text writing of PNS with Au NPs at micro scale. The height of the “SPIE” letter is $1.9 \mu\text{m}$. (b) Inverse direct text writing of the “SPIE” letter. (c) Direct text writing in one page.

Figure 4.4 (a) shows another example of fabricated plasmonic structures: the “SPIE” word made by Au NPs. The height of this word is measured to be $1.9 \mu\text{m}$. Generally, any submicro scale text can be written by this DLW method and read by

4.2. DATA STORAGE

the plasmonic effect. Figure 4.4 (c) shows a full text at submicro scale. An inverse writing way can be implied with the DLW method as well. For that, the background was exposed with the laser to form Au NPs, and the non-exposed area is formed as the text. Figure 4.4 (b) illustrates the microscope image of the “SPIE” word, in which Au NPs were distributed as the background. The height of the inverse text is measured as $4\ \mu\text{m}$, which is bigger than that obtained by the direct writing way. The reason is that the overlap effect of Au NPs is formed at the edge of the line.

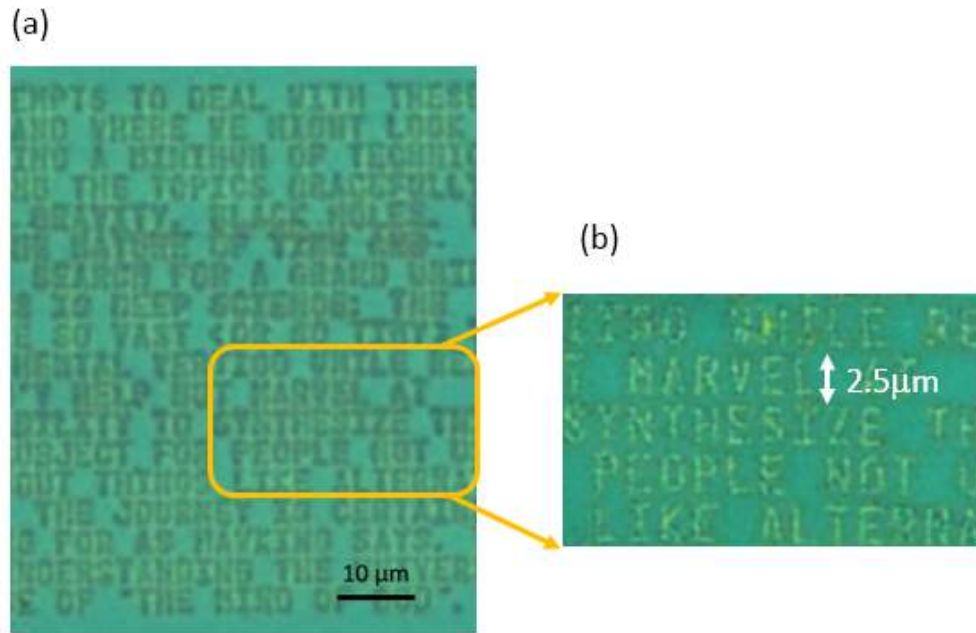


Figure 4.5: (a) Direct text writing at micro-scale on Ag NPs in one page. (b) In detail, the height of the letter is $2.5\ \mu\text{m}$.

Similar to Au material, we also realized microstructures, texts, codes on Ag film. Figure 4.5 illustrates the direct text writing of Ag NPs.

4.3 Color printer

It is well known that the plasmonic resonance depends strongly on NPs size, which itself depends on fabrication parameters, i.e. exposure dose. We have demonstrated the tuning of plasmonic color by changing the parameters of the exposure dose.

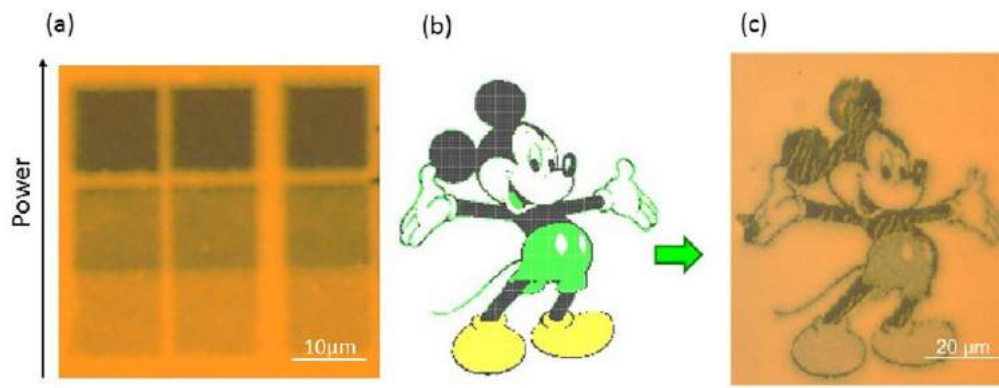


Figure 4.6: (a) Microscope image of Au NPs patterns fabricated by different laser powers. (b) The processed image of “Mickey Mouse” imported and transformed by Matlab. (c) The nano color printed image fabricated by the DLW method on Au film.

Figure 4.6 (a) shows the reflected optical microscope image of the fabricated structures $10 \times 10 (\mu\text{m}^2)$. As the laser exposure dose increases, the color changes from the natural color of the Au film to yellow, then to green.

We then applied this idea to realize nanostructures with different colors. An image of “Mickey Mouse” was imported to a Matlab program, and each pixel was transferred to an exact dose of the light exposure with three distinct colors: dark color, yellow, and green, as shown in Fig. 4.6 (b). For fabrication, the scanning speed is fixed at $10 \mu\text{m}/\text{s}$ and the laser power was set as 35 mW, 30 mW, and 25 mW for the production of dark, green, and yellow colors, respectively. Figure 4.6 (c) shows the corresponding plasmonic image at the micro scale. The image is successfully reproduced.

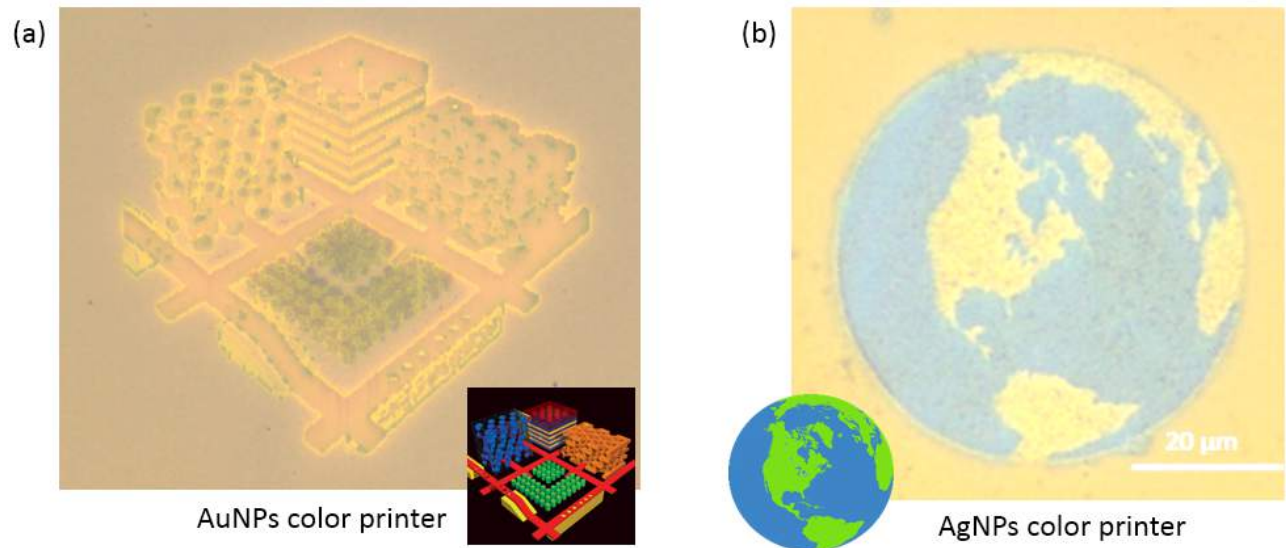


Figure 4.7: (a) The nano color printing of Au NPs patterns by the DLW method with different writing parameters. (b) The nano color printing of Ag NPs patterns. Insert image is the original image.

By playing with plasmonic NPs sizes, we even can produce more complicated 3D structures. Figure 4.7 (a) shows a 3D photonic crystal image by three different colors. The insert is the original image, which can be compared with the experimental result.

Similarly, we obtained the color printing of Ag NPs shown in Fig. 4.7 (b). The insert image is the original image of the “Earth”, of which the green color is replaced by the yellow color. We note that, the plasmonic spectra of Ag NPs does not vary much with their NPs size. Therefore, it is difficult to produce more colors with these Ag NPs, and the main color is located in the UV range.

4.4 Fluorescence enhancement

Metal nanostructures exhibit remarkable optical properties due to the excitation of their surface plasmons by an incident light, which results in a significant enhance-

4.4. FLUORESCENCE ENHANCEMENT

ment of the electromagnetic field at the NP surface. This enhanced near field can be used to design highly sensitive chemical and biosensors with specific plasmon resonances tailored by the NP geometry. Metallic NPs have been shown to enhance the fluorescence emission and decrease the molecular excited-state lifetimes of vicinal fluorophores [149]. The fluorescence enhancement is attributable to a combination of processes including enhanced absorption by the molecule, modification of the radiative decay rate of the molecule, and enhanced coupling efficiency of the fluorescent emission to the far-field [150].

We proposed to demonstrate the use of metallic NPs in a monolayer as the fluorescent enhancement medium. In this experiment, the Ag NPs covered with the RhB/PMMA mixture is used to measure the fluorescence enhancement.

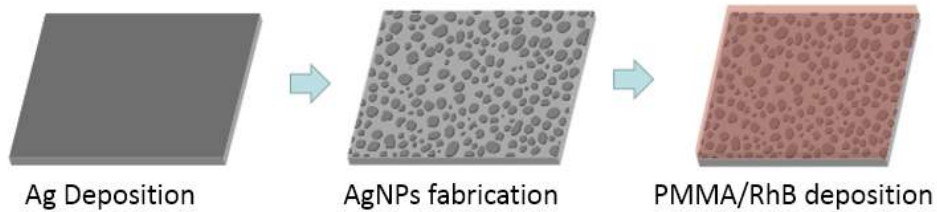


Figure 4.8: *The sample fabrication process of fluorescence enhancement.*

The fabrication process of plasmonics-enhanced fluorescence sample is illustrated in Fig. 4.8. The Ag NPs are obtained by using an oven annealing method (chapter 2) or the DLW method (chapter 3). Then a mixture of RhB and PMMA is deposited on top of Ag NPs sample to make the fluorophore filled around the NPs. By applying a CW laser whose wavelength is suitable for the absorption of the fluorophore covered with NPs, the fluorescence enhancement can be detected by the detection system.

Figure 4.9 (a) illustrates the fabrication method of mixed fluorophore solution. First, 1 *wt.*% of RhB is mixed in the PMMA solution with a magneto spin for about

4.4. FLUORESCENCE ENHANCEMENT

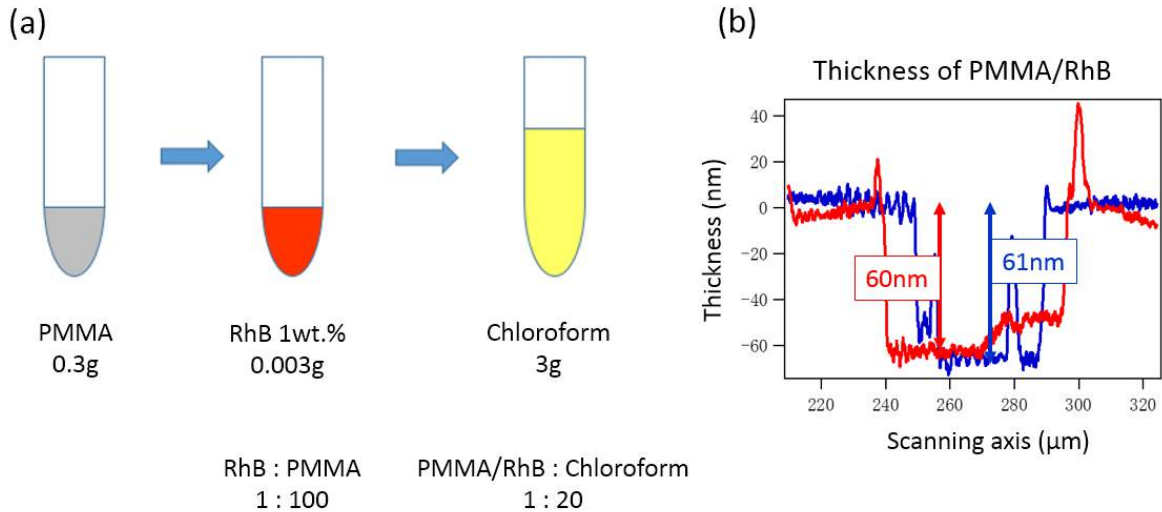


Figure 4.9: (a) The fabrication of the PMMA/RhB mixture. (b) The thickness of the spin-coated layers of the PMMA/RhB mixture.

24 hours. Then, the mixture is mixed with Chloroform solution with a ratio of 1 to 20. The fluorophore layer is spin-coated on a glass substrate to measure the thickness by the Dektak profilometer. The desired thickness of RhB/PMMA is about 60 nm, as shown in Fig. 4.9 (b), which is comparable to the size of Ag NPs. This thickness was chosen because the plasmonic field enhancement is near Ag NPs with an evanescent distance of less than 50 nm.

To obtain the fluorescence enhancement, first, we need to measure the absorption spectra to determine the wavelength of the incident laser. Figure 4.10 illustrates the absorption spectrum of Ag NPs, the fluorophore layer, and the fluorophore layer on Ag NPs. There are two absorption peaks in the fluorophore layer with Ag NPs. The left peak is mainly due to the Ag NPs, and the right one is due to the absorption of RhB. Between the two peaks, there still exists a strong absorption, ranging from 450 nm to 600 nm. This is a mixing between absorption of RhB and that of Ag NPs.

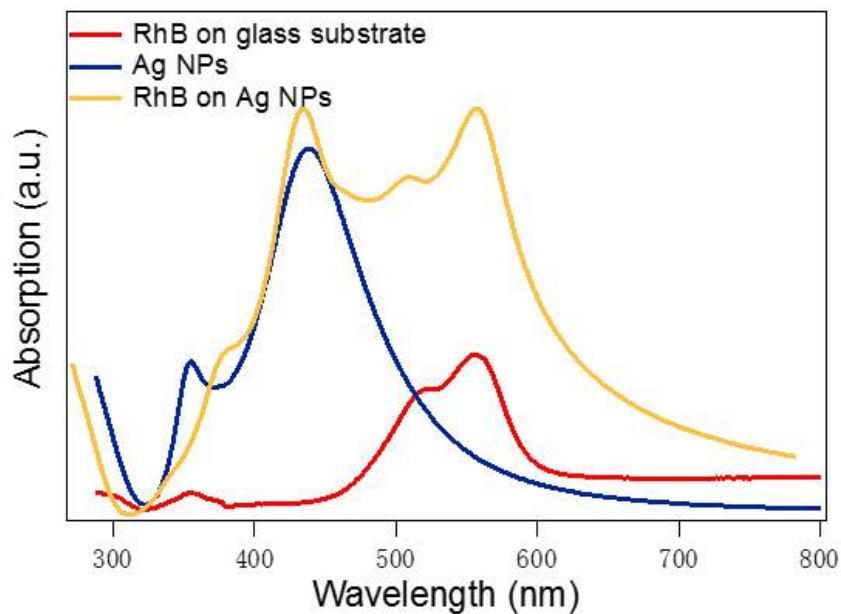


Figure 4.10: Absorption spectra of the fluorophore layer (*RhB*), *Ag NPs*, and fluorophore layer spin-coating on *Ag NPs*.

Therefore, we have used the DLW wavelength (532 nm) as the excitation light. The fluorescence signal is measured by a photon counter with putting a long pass filter (cut off wavelength is 580 nm) to stop the excitation light source.

Figure 4.11 illustrates the comparison of the fluorescence signal obtained before and after the deposition of *RhB/PMMA* mixture on the *Ag NPs* samples. In the experiment, *Ag NPs* samples are fabricated with different powers as 5, 10, 15, 20, 30, 40, 50, 80, and 100 mW, respectively. The fluorescence images have significant changes, as shown in Fig. 4.11 (e, f), of which the fluorescence scale is the same. The fluorescence intensity of *Ag NPs* is less stronger than the background of *Ag* film, as Fig. 4.11 (e) shows, but after spin-coating the *RhB/PMMA* layer on the top, the *Ag NPs* areas have a very strong fluorescence signal, as shows the bright yellow color in the same area of Fig. 4.11 (f). In the figures, bright color indicates more photons

4.4. FLUORESCENCE ENHANCEMENT

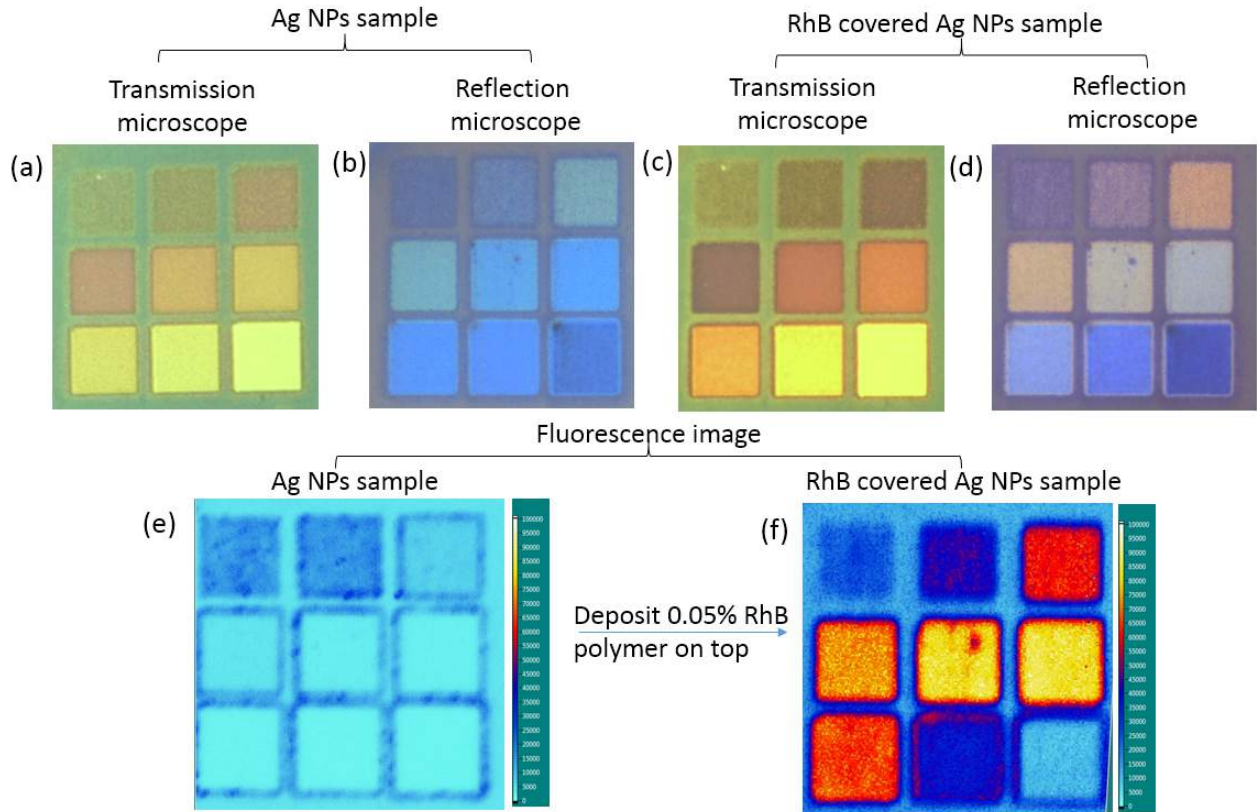


Figure 4.11: *The comparison of fluorescence enhancement before and after the deposition of RhB polymer on top of Ag NPs sample. (a,b) The transmission and reflection microscope image of pure Ag NPs samples fabricated by different laser power. (c, d) The transmission and reflection microscope images obtained after RhB deposition. (e, f) The fluorescence image with the samples obtained before and after deposit RhB, respectively.*

(fluorescence enhanced) appeared in a specific size of Ag NPs.

To quantitatively describe the fluorescence enhancement of RhB/PMMA covered Ag NPs, a fluorescence enhancement ratio is defined as:

$$ratio = \frac{\text{number of photons of the Ag NPs covered with RhB}}{\text{number of photons of the background covered with RhB}}$$

The number of photons of the Ag NPs covered with RhB/PMMA and correspond-

4.4. FLUORESCENCE ENHANCEMENT

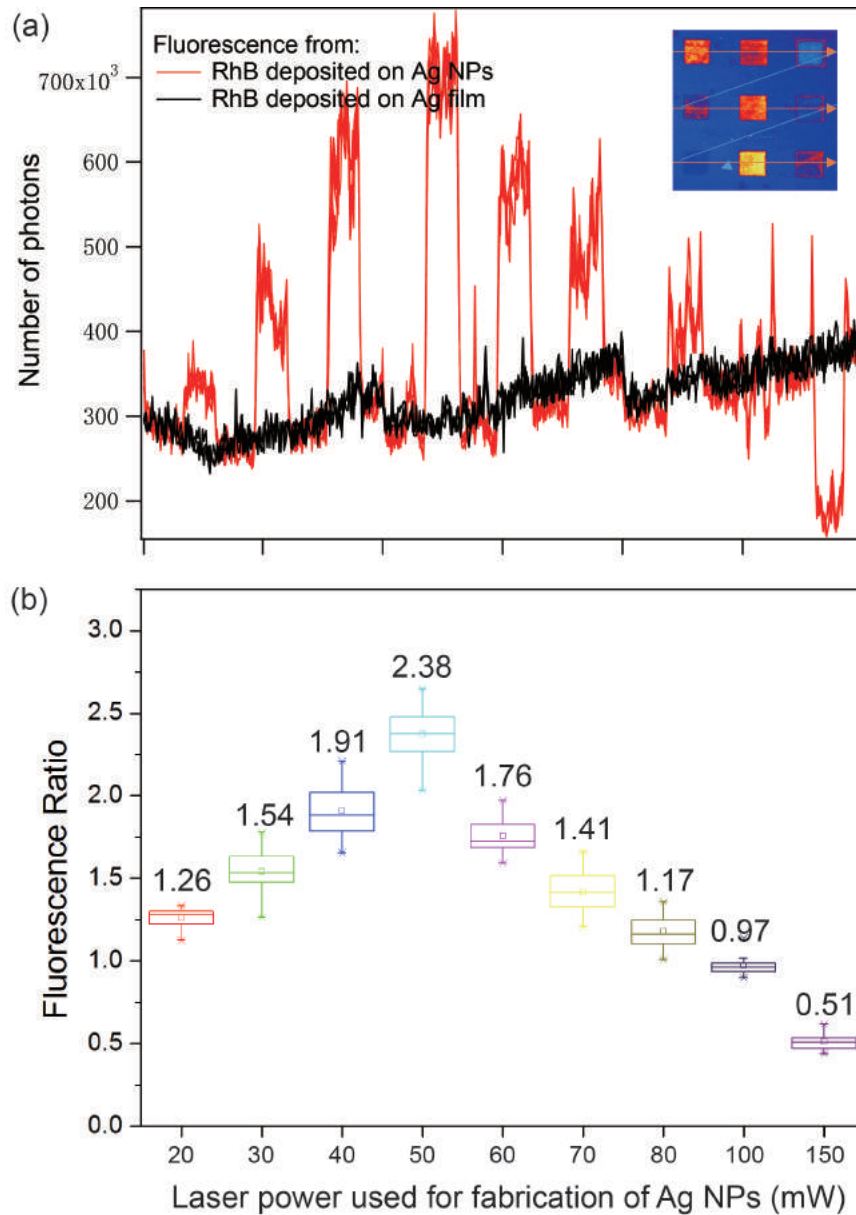


Figure 4.12: (a) Fluorescence signal measured in the x -direction of the RhB deposited in Ag NPs and in Ag film. (insert) The fluorescence image shows the selection of the fluorescence signal along 1 direction. (b) Calculation of fluorescence enhancement ratio of (a).

ing background (also covered RhB/PMMA) are illustrated in Fig. 4.12 (a). The insert figure of the fluorescence image shows the selection method. In the figure, the

4.4. FLUORESCENCE ENHANCEMENT

red curve shows the data of Ag NPs and the black curve shows the data from the background. The fluorescence enhancement ratio is calculated and illustrated in Fig. 4.12 (b). In this statistics figure, the centerline shows the average value, the top, and bottom of the bar box shows the 25 % and the 75 % of the data range, and the vertical line in top and bottom to the strip box show the first and the last 25 % data range. For the Ag NPs obtained with the writing powers of 10, 20, 30, and 40 mW, the fluorescence enhancement ratio is increased, the corresponding values are 1.26, 1.54, 1.91, and 2.38. The ratio reaches the maximum as the writing power reaches to 40 mW. Then, if the writing power continues to increase, the fluorescence enhancement ratio decreases. At 150 mW, the enhancement ratio is 0.51, which means all the Ag film is evaporated.

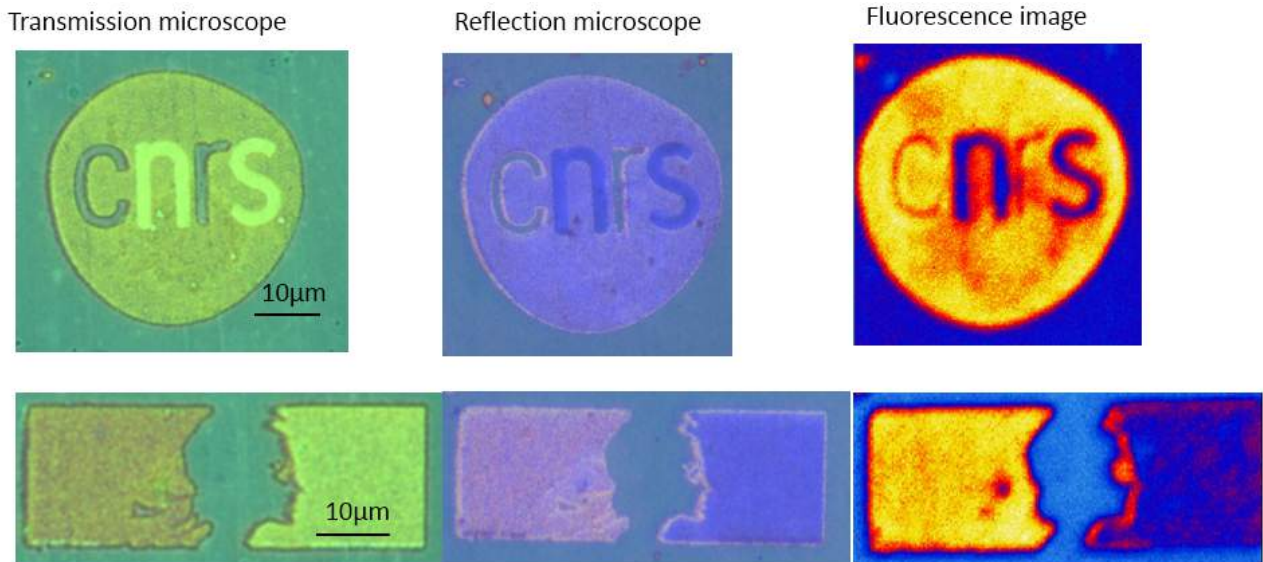


Figure 4.13: Comparison of color printing achieved by different observation methods. From left to right: transmission microscope, reflection microscope and fluorescence images of Ag NPs sample, covered with RhB/PMMA.

The fluorescence signal of the Ag NPs covered with RhB/PMMA is enhanced and reaches a factor of 2.38. This enhancement is still modest, but consistent with results published in literature [150]. Figure 4.13 illustrates different observations of color

printing images of the Ag NPs sample, which is covered with RhB/PMMA. The color printing is illustrated in different measurements: transmission microscopy, reflective microscopy, and fluorescent imaging. The reading from the fluorescence enhancement image has more contrast than the optical microscope images, so it is easier to be read and recognized.

4.5 Random laser based on a monolayer of Au NPs

Nowadays, random lasers based on LSPR have attracted more attention [151], because it is different from traditional cavity-based lasers. Indeed, random lasing results from the interaction of multiple light scattering events by dielectric or metallic scatters and the formation of closed-loop paths from the scattered light [152]. This feedback mechanism leads to resonating structures with a moderate Q factor. The gain in random lasers strongly depends on the medium scattering strength. Random lasers have demonstrated a low threshold and high-performance characteristics [153].

In this work, we demonstrated the random laser effect by the use of a monolayer of Au NPs. For that, we spin-coated an RhB layer on the top of the Au NPs monolayer, and excite the sample by a high energy pulsed laser.

The setup of the Au NPs based random laser is shown in Fig. 4.14. A pulsed laser with wavelength 532 nm, beam diameter 400 μm , repetition 5 Hz and pulse Width 1.7 ns, is incident to a convex lens having focal length of 50 mm. The pumping intensity is calculated by changing the distance between the NPs sample and the focusing lens. The lasing effect measured by a detector in the direction perpendicular to the pumping direction, as shown in Fig. 4.14.

Figure 4.15 illustrates the spectra of the random lasers based on Au NPs with a 1 wt.% RhB/SU8 polymer, whose thickness is set to 500 nm, 1000 nm, and 1500 nm,

4.5. RANDOM LASER BASED ON A MONOLAYER OF AU NPS

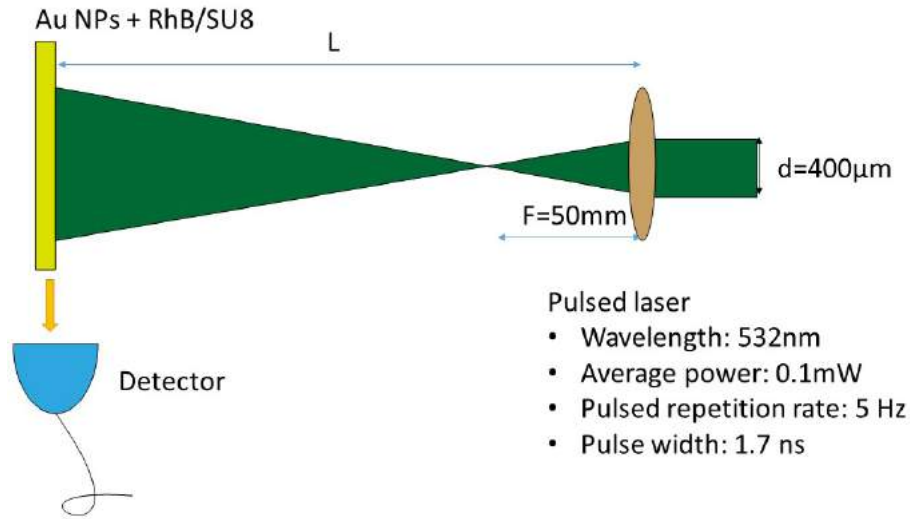


Figure 4.14: *Illustration of the setup used to study the random laser with Au NPs. The pumping intensity is controlled by changing the distance (L) between a convex lens and Au NPs samples.*

respectively. We have studied the evolution of emission spectra of the samples as a function of the pumping intensity. By changing the distance L , as can be seen in Fig. 4.15, at a particular pumping intensity of about $3.2 \times 10^6 \text{ W/cm}^2$, corresponding to a distance $L=9 \text{ cm}$, a narrow but intense peak appears at about 580 nm. This peak, however, is not really a laser emission because it is still too large. We believe that this is simply an amplified spontaneous emission (ASE) of this RhB/SU8 medium as it was observed often in a dye or excimer laser. In order to have a lasing effect, it requires probably a higher pumping intensity. However, as can be seen in Fig. 4.15, when the intensity is too high, the ASE peak disappears and the emission spectra decreases. That is due to the bleaching effect of RhB/SU8 as well as of Au NPs. Therefore, we cannot observe the true random laser based on Au NPs for this moment. A better condition, such as optimum pumping wavelength, better concentration of RhB in SU8, shorter pumping pulses width, or better RhB/SU8 thickness is necessary to study in order to obtain a random laser based on these fabricated Au NPs.

4.6. CONCLUSION AND DISCUSSION

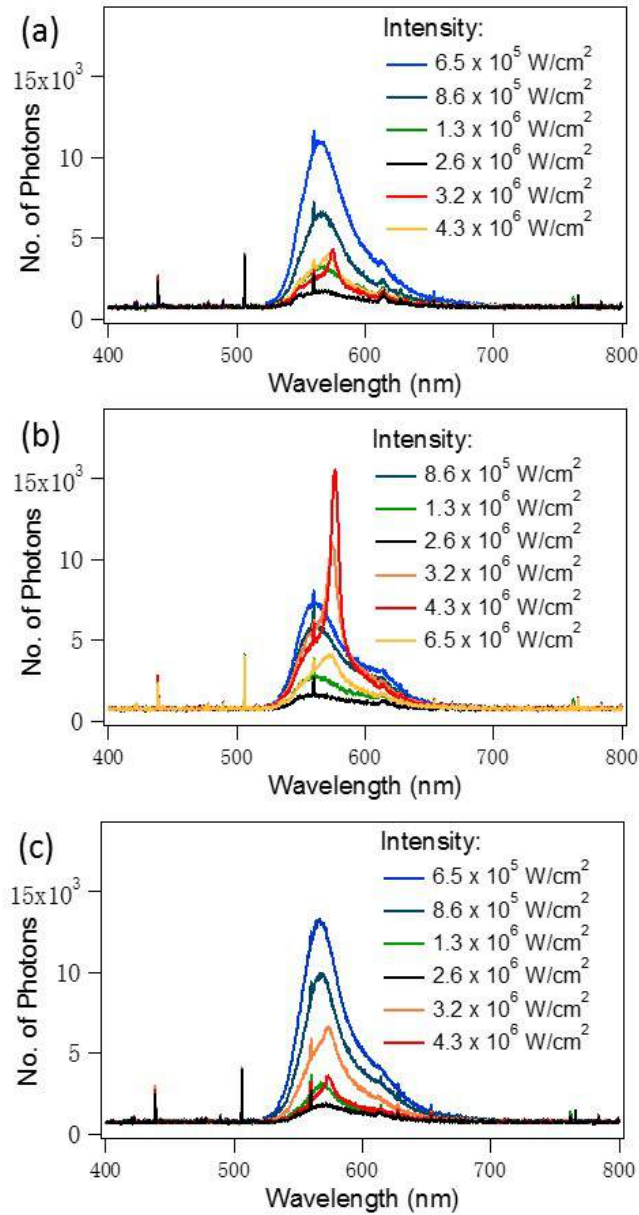


Figure 4.15: *Emission spectra of RhB/SU8 spin-coated on a monolayer of Au NPs as a function of the pumping intensity. The thickness of RhB/SU8 are 500 nm (a), 1000 nm (b), and 1500 nm (c), respectively.*

4.6 Conclusion and discussion

In this chapter, we demonstrated some applications of PNS based on Au and Ag NPs.

4.6. CONCLUSION AND DISCUSSION

First, we introduced a new data storage method by using Au or Ag NPs. Since our DLW writing method is similar to those of CDs and DVDs, we used this method to write the binary codes in metallic film and compare its capacity with those of standard CDs and DVDs. The capacity of the plasmonic writing is about 914 Mb for this moment, which is better than a standard CD but less good than the standard DVD. Then, the micrometer bar code and QR code recording are also demonstrated. An example of a QR code whose size is 70×70 (μm^2), which links to the website of our laboratory, is realized as a proof of principle. After that, we demonstrate direct text writing with Au and Ag NPs. The height of the letter of Au NPs is $1.9 \mu\text{m}$, while the height of the letter of Ag NPs is $2.5 \mu\text{m}$. This is because the Au NPs have a denser particle arrangement than the Ag NPs, so the edge between NPs and the unexposed Au film is clearer than the Ag one.

Second, we demonstrated the nano color printing of PNS with Au and Ag NPs. We introduced the tuning of plasmonic color by changing the parameters of the exposure dose. And then we applied this idea to realize nanostructures with different colors. To obtain different plasmonic colors, the scanning speeds, laser powers and the distance between scanning lines are varied. This allows the realization of different loved images at the microscale. The colors are however limited at red, yellow and green for Au NPs and at yellow and blue for Ag NPs. Because the localized plasmonic resonance of metallic NPs changes very weakly as a function of their size.

Third, we demonstrated fluorescence enhancement of Ag NPs covered with RhB/PMMA. Thanks to the field enhancement nearby the metallic NPs, the fluorescence of RhB/PMMA is enhanced by a factor up to 2.38. The enhancement ratio depends on the NPs size, which is controlled by the laser power of the DLW technique. By covering a plasmonic image with a thin RhB/PMMA, we showed that the fluorescence image of such a plasmonic structure is clearer with higher contrast.

4.6. CONCLUSION AND DISCUSSION

Finally, we demonstrated the first try to obtain a random laser of Au NPs. The preliminary result, by changing the film thickness and the pumping intensity shows that a strong amplified spontaneous emission was obtained. More study, such as excitation wavelength, film thickness, etc., should be done in the next, to demonstrate a real random laser. The DLW method has a great advantage to make a random laser with a desired laser beam and shape.

Conclusion and Prospects

In this work, we systematically studied the fabrication of large-area monolayer of Au and Ag NPs. We have demonstrated the fabrication of Au and Ag NPs by the thermal dewetting method in an oven. By analyzing their SEM images, the morphologies, such as shape and size distribution, are characterized. We discussed annealing temperature and annealing duration to form Au and Ag NPs. At different annealing temperatures, the resonant peaks of Au or Ag NPs changed slightly, which corresponds to different average size distribution. And for different annealing durations, the intensity of resonant peaks is different, and it responds to different numbers of NPs. Then, with the help of the Lumerical FDTD method, the optical properties of Au and Ag NPs were simulated by importing SEM images of the random shape of NPs. For Au NPs, the plasmonic resonant peaks are redshifted by 48 nm when the average NPs size changed from 20 nm to 100 nm. And for Ag NPs, when the average sizes are changed, the plasmonic resonant peaks also have the shift. Environmental impacts were also discussed. When the NPs are changed from air to water and then to oil, the resonant peaks shift red. We also studied a mixed Au and Ag NPs by this thermal annealing method. In the beginning, we tried to use the same annealing temperature, which can both form Au and Ag NPs separately, to form the combined Au and Ag NPs. We failed because they couldn't form NPs. After that, we tried to deposit the Ag on Au NPs. The resonance curve showed two peaks at the positions of the pure Au and Ag

4.6. CONCLUSION AND DISCUSSION

NPs. FDTD simulation results, which set half of the NPs as Au and the other half as Ag, are consistent with the peak position of the experiment, which means that Ag is covered on the Au NPs.

We demonstrated the optically induced thermal effect on the fabrication of metallic PNS in a small area. We theoretically studied the optically induced thermal effect in a real metallic film by using Comsol software, which can deal with the rough surface as in the experiment. We studied the induced temperature in the laser focus center as a function of the laser intensity and of the exposure time. It shows that the temperature will reach a stable value after 30 μ s, and the maximum induced temperature linearly changes as a function of the laser intensity. We applied the simulations for both Au and Ag materials. We found that the laser power required to obtain the Ag NPs is much lower than that required for Au NPs. The optically induced thermal effect of different thickness, 12 nm and 50 nm, respectively, is studied. For the 12 nm thick film, the high induced temperature is easy to cut off the connection in the metallic film to form the metallic NPs. But for the 50 nm thick film, it can form nano-holes when the localized induced temperature is high enough to evaporate the metal. We studied the temperature distribution for a thick metallic film of 50 nm for two cases: perfect uniform and rough surface. With the same laser power, the laser focuses to create a perfect circular temperature spot for a uniform metallic film while in the case of rough surface, the temperature spot is irregular. Then, the Au NPs, Ag NPs and Au NHAs are fabricated by using the DLW method. We explained first the working principle of the system, and then how to combine the Matlab software works with the Labview program. By using this DLW system, we obtained the Au and Ag NPs with different particle sizes by controlling the laser power and the exposure time. The results of color and size changes are consistent with the FDTD simulations. After that, a two-step writing method is suggested to improve the minimum period of the 1D structure, which

4.6. CONCLUSION AND DISCUSSION

shows a stable Au PNS with a minimum period of 400 nm. We also demonstrated the fabrication of the Au NHAs by using this DLW system and theoretically studied their optical properties. In the experiment, two kinds of Au NHA structures, square and hexagon, are obtained on the 50-nm thickness Au layer. The periods of square and hexagonal structures are 1 μm and 1.1 μm , respectively. The experimental nanoholes show irregular shapes, which are consistent with the simulations due to the rough surface of the Au film. Then, the transmission spectrum of Au NHA of these two structures is studied. The high transmission peak appears around 1550 nm for the square structure and at 1450 nm for the hexagonal structure. Since the nanoholes are irregular, the electric field distribution and transmission of NHA are studied and compared to the ideal models. We found that even the electric field distributions of real structure and ideal model are very different at the nanoholes position but the transmission spectra are almost the same. This proved that the plasmonic resonances of Au NHA depend on the nanohole diameter, period, and structure, but not on the nanoholes shape. This is similar to the result of the plasmonic resonance of metallic NPs, for which the resonance spectra also depend on the average size of metallic NPs instead of the shape of each NP.

Several applications of PNS based on Au and Ag NPs were demonstrated. A new data storage method by using Au or Ag NPs is first introduced. Since our DLW writing method is similar to those of CDs and DVDs, we used this method to write the binary codes in metallic film and compare its capacity with those of standard CDs and DVDs. The capacity of the plasmonic writing is about 914 Mb for this moment, which is better than a standard CD but less good than the standard DVD. Then, the micrometer bar code and QR code recording are also demonstrated. An example of a QR code whose size is 70×70 (μm^2), which links to the website of our laboratory, is realized as a proof of principle. After that, we demonstrate direct text writing with

4.6. CONCLUSION AND DISCUSSION

Au and Ag NPs. The height of the letter of Au NPs is $1.9 \mu\text{m}$, while the height of the letter of Ag NPs is $2.5 \mu\text{m}$. This is because the Au NPs have a denser particle arrangement than the Ag NPs, so the edge between NPs and the unexposed Au film is clearer than the Ag one. Then, we demonstrated the nano color printing of PNS with Au and Ag NPs. We introduced the tuning of plasmonic color by changing the parameters of the exposure dose. And then we applied this idea to realize nanostructures with different colors. To obtain different plasmonic colors, the scanning speeds, laser powers and the distance between scanning lines are varied. This allows the realization of different loved images at the microscale. The colors are however limited at red, yellow and green for Au NPs and at yellow and blue for Ag NPs. Because the localized plasmonic resonance of metallic NPs changes very weakly as a function of their size. After that, we demonstrated fluorescence enhancement of Ag NPs covered with RhB/PMMA. Thanks to the field enhancement nearby the metallic NPs, the fluorescence of RhB/PMMA is enhanced by a factor up to 2.38. The enhancement ratio depends on the NPs size, which is controlled by the laser power of the DLW technique. By covering a plasmonic image with a thin RhB/PMMA, we showed that the fluorescence image of such a plasmonic structure is clearer with higher contrast. At last, we demonstrated the first try to obtain a random laser of Au NPs. The preliminary result, by changing the film thickness and the pumping intensity shows that a strong amplified spontaneous emission was obtained.

Outlooks

There are many works should be done in the near future. In chapter 2, we have studied the fabrication of large-area monolayer of Au NPs, Ag NPs and mixed Au and Ag NPs. Following this work, there are a lot of things to do, such as fabricating other metallic NPs, a new combined NPs, and studying their optical properties. In

4.6. CONCLUSION AND DISCUSSION

chapter 3, we have demonstrated the fabrication of the Au NHAs by using the DLW method. Due to the rough surface of the Au film, the experimental nanoholes have irregular shapes. However, the electric field distributions are quite inhomogeneous in real NHA, like Anderson localization. Then, we propose a smaller period of this NHA to have the transmission spectra in the visible light range. We expect these fabricated structures can strongly enhance light-matter interaction when the fluorescent layer is covered with this NHA. In chapter 4, we demonstrated an application of random laser of Au NPs by using the DLW method for the first time. We have preliminary studied the affection of film thickness and pumping intensity. More study, such as excitation wavelength, film thickness, etc., should be done in the next, to demonstrate a real random laser. The DLW method has a great advantage to make a random laser with a desired laser beam and shape.

Bibliography

- [1] Maier, S. A., [*Plasmonics: fundamentals and applications*], Springer Science & Business Media (2007).
- [2] Freestone, I., Meeks, N., Sax, M., and Higgitt, C., “The lycurgus cupa roman nanotechnology,” *Gold bulletin* **40**(4), 270–277 (2007).
- [3] Colomban, P. and Tournié, A., “On-site raman identification and dating of ancient/modern stained glasses at the sainte-chapelle, paris,” *Journal of Cultural Heritage* **8**(3), 242–256 (2007).
- [4] Ulf, L., “Optical metamaterials : Invisibility cup,” *Nature Photonics* **1**, 207208 (2007).
- [5] Holister, P., Weener, J.-W., Román, C., and Harper, T., “Nanoparticles,” *Technology White Papers* **3**, 1–11 (2003).
- [6] Zayats, A. V., Smolyaninov, I. I., and Maradudin, A. A., “Nano-optics of surface plasmon polaritons,” *Physics reports* **408**(3-4), 131–314 (2005).
- [7] Kinsey, N., Ferrera, M., Shalaev, V., and Boltasseva, A., “A platform for practical plasmonics,” *SPIE Newsroom* (2014).

BIBLIOGRAPHY

- [8] Rojalin, T., Phong, B., Koster, H. J., and Carney, R. P., “Nanoplasmonic approaches for sensitive detection and molecular characterization of extracellular vesicles,” *Frontiers in chemistry* **7** (2019).
- [9] Aman, S., Khan, I., Ismail, Z., and Salleh, M. Z., “Impacts of gold nanoparticles on mhd mixed convection poiseuille flow of nanofluid passing through a porous medium in the presence of thermal radiation, thermal diffusion and chemical reaction,” *Neural Computing and Applications* **30**(3), 789–797 (2018).
- [10] Howes, P. D., Chandrawati, R., and Stevens, M. M., “Colloidal nanoparticles as advanced biological sensors,” *Science* **346**(6205), 1247390 (2014).
- [11] Zeng, B., Gao, Y., and Bartoli, F. J., “Ultrathin nanostructured metals for highly transmissive plasmonic subtractive color filters,” *Scientific reports* **3**, 2840 (2013).
- [12] Cheng, F., Gao, J., Luk, T. S., and Yang, X., “Structural color printing based on plasmonic metasurfaces of perfect light absorption,” *Scientific reports* **5**, 11045 (2015).
- [13] Haug, T., Klemm, P., Bange, S., and Lupton, J. M., “Hot-electron intraband luminescence from single hot spots in noble-metal nanoparticle films,” *Physical review letters* **115**(6), 067403 (2015).
- [14] Huang, X. and El-Sayed, M. A., “Plasmonic photo-thermal therapy (pptt),” *Alexandria journal of medicine* **47**(1) (2011).
- [15] Guler, U., Ndukaife, J. C., Naik, G. V., Nnanna, A. A., Kildishev, A. V., Shalaev, V. M., and Boltasseva, A., “Local heating with lithographically fabricated plasmonic titanium nitride nanoparticles,” *Nano letters* **13**(12), 6078–6083 (2013).

BIBLIOGRAPHY

- [16] Kim, J. S., Kuk, E., Yu, K. N., Kim, J.-H., Park, S. J., Lee, H. J., Kim, S. H., Park, Y. K., Park, Y. H., Hwang, C.-Y., et al., “Antimicrobial effects of silver nanoparticles,” *Nanomedicine: Nanotechnology, Biology and Medicine* **3**(1), 95–101 (2007).
- [17] Yu, P., Yao, Y., Wu, J., Niu, X., Rogach, A. L., and Wang, Z., “Effects of plasmonic metal core -dielectric shell nanoparticles on the broadband light absorption enhancement in thin film solar cells,” *Scientific Reports* **7**(1), 7696 (2017).
- [18] Wu, J., Yu, P., Susha, A. S., Sablon, K. A., Chen, H., Zhou, Z., Li, H., Ji, H., Niu, X., Govorov, A. O., Rogach, A. L., and Wang, Z. M., “Broadband efficiency enhancement in quantum dot solar cells coupled with multispiked plasmonic nanostars,” *Nano Energy* **13**, 827 – 835 (2015).
- [19] Kim, S.-S., Na, S.-I., Jo, J., Kim, D.-Y., and Nah, Y.-C., “Plasmon enhanced performance of organic solar cells using electrodeposited ag nanoparticles,” *Applied Physics Letters* **93**(7), 305 (2008).
- [20] Colvin, V., Schlamp, M., and Alivisatos, A. P., [*Light-emitting diodes made from cadmium selenide nanocrystals and a semiconducting polymer*], vol. 370, Nature Publishing Group (1994).
- [21] Kneipp, K., Haka, A. S., Kneipp, H., Badizadegan, K., Yoshizawa, N., Boone, C., Shafer-Peltier, K. E., Motz, J. T., Dasari, R. R., and Feld, M. S., “Surface-enhanced raman spectroscopy in single living cells using gold nanoparticles,” *Applied Spectroscopy* **56**(2), 150–154 (2002).
- [22] Boisselier, E. and Astruc, D., “Gold nanoparticles in nanomedicine: preparations, imaging, diagnostics, therapies and toxicity,” *Chemical society reviews* **38**(6), 1759–1782 (2009).

BIBLIOGRAPHY

- [23] Hoffman, A., Mills, G., Yee, H., and Hoffmann, M., “Q-sized cadmium sulfide: synthesis, characterization, and efficiency of photoinitiation of polymerization of several vinylic monomers,” *The Journal of Physical Chemistry* **96**(13), 5546–5552 (1992).
- [24] Hamilton, J. and Baetzold, R., “Catalysis by small metal clusters,” *Science* **205**(4412), 1213–1220 (1979).
- [25] Iravani, S., Korbekandi, H., Mirmohammadi, S. V., and Zolfaghari, B., “Synthesis of silver nanoparticles: chemical, physical and biological methods,” *Research in pharmaceutical sciences* **9**(6), 385 (2014).
- [26] Hurtado-Aviles, E. A., Torres, J. A., Trejo-Valdez, M., Urriolagoitia-Sosa, G., Villalpando, I., and Torres-Torres, C., “Acousto-plasmonic sensing assisted by nonlinear optical interactions in bimetallic au-pt nanoparticles,” *Micromachines* **8**(11) (2017).
- [27] Park, W., “Optical interactions in plasmonic nanostructures,” *Nano Convergence* **1**(1), 2 (2014).
- [28] Linic, S., Aslam, U., Boerigter, C., and Morabito, M., “Photochemical transformations on plasmonic metal nanoparticles,” *Nature materials* **14**(6), 567–576 (2015).
- [29] Gilman, J. J., “Utility of the plasmon theory of surface and interfacial energies,” *Science and Technology of Interfaces* , 195–206 (2002).
- [30] Prodan, E., Radloff, C., Halas, N. J., and Nordlander, P., “A hybridization model for the plasmon response of complex nanostructures,” *science* **302**(5644), 419–422 (2003).

BIBLIOGRAPHY

- [31] Jain, P. K. and El-Sayed, M. A., “Plasmonic coupling in noble metal nanostructures,” *Chemical Physics Letters* **487**(4-6), 153–164 (2010).
- [32] Salomon, A., Prior, Y., Fedoruk, M., Feldmann, J., Kolkowski, R., and Zyss, J., “Plasmonic coupling between metallic nanocavities,” *Journal of Optics* **16**(11), 114012 (2014).
- [33] Nordlander, P., Oubre, C., Prodan, E., Li, K., and Stockman, M., “Plasmon hybridization in nanoparticle dimers,” *Nano letters* **4**(5), 899–903 (2004).
- [34] Weissman, A., Galanty, M., Gachet, D., Segal, E., Shavit, O., and Salomon, A., “Spatial confinement of light onto a flat metallic surface using hybridization between two cavities,” *Advanced Optical Materials* **5**(10), 1700097 (2017).
- [35] Najiminaini, M., Vasefi, F., Kaminska, B., and Carson, J. J., “A three-dimensional plasmonic nanostructure with extraordinary optical transmission,” *Plasmonics* **8**(2), 217–224 (2013).
- [36] Li, X., Soler, M., Özdemir, C. I., Belushkin, A., Yesilköy, F., and Altug, H., “Plasmonic nanohole array biosensor for label-free and real-time analysis of live cell secretion,” *Lab on a chip* **17**(13), 2208–2217 (2017).
- [37] Lee, S. H., Bantz, K. C., Lindquist, N. C., Oh, S.-H., and Haynes, C. L., “Self-assembled plasmonic nanohole arrays,” *Langmuir* **25**(23), 13685–13693 (2009).
- [38] Nakamoto, K., Kurita, R., Niwa, O., Fujii, T., and Nishida, M., “Development of a mass-producible on-chip plasmonic nanohole array biosensor,” *Nanoscale* **3**(12), 5067–5075 (2011).
- [39] Henzie, J., Lee, J., Lee, M. H., Hasan, W., and Odom, T. W., “Nanofabrication of plasmonic structures,” *Annual review of physical chemistry* **60**, 147–165 (2009).

BIBLIOGRAPHY

- [40] Hao, F., Nehl, C. L., Hafner, J. H., and Nordlander, P., “Plasmon resonances of a gold nanostar,” *Nano letters* **7**(3), 729–732 (2007).
- [41] Khoury, C. G. and Vo-Dinh, T., “Gold nanostars for surface-enhanced raman scattering: synthesis, characterization and optimization,” *The Journal of Physical Chemistry C* **112**(48), 18849–18859 (2008).
- [42] Pérez-Juste, J., Pastoriza-Santos, I., Liz-Marzán, L. M., and Mulvaney, P., “Gold nanorods: synthesis, characterization and applications,” *Coordination chemistry reviews* **249**(17-18), 1870–1901 (2005).
- [43] Kim, F., Song, J. H., and Yang, P., “Photochemical synthesis of gold nanorods,” *Journal of the American Chemical Society* **124**(48), 14316–14317 (2002).
- [44] Busbee, B. D., Obare, S. O., and Murphy, C. J., “An improved synthesis of high-aspect-ratio gold nanorods,” *Advanced Materials* **15**(5), 414–416 (2003).
- [45] Murphy, C. J., “Nanocubes and nanoboxes,” *Science* **298**(5601), 2139–2141 (2002).
- [46] Yavuz, M. S., Cheng, Y., Chen, J., Cobley, C. M., Zhang, Q., Rycenga, M., Xie, J., Kim, C., Song, K. H., Schwartz, A. G., et al., “Gold nanocages covered by smart polymers for controlled release with near-infrared light,” *Nature materials* **8**(12), 935 (2009).
- [47] Skrabalak, S. E., Chen, J., Sun, Y., Lu, X., Au, L., Cobley, C. M., and Xia, Y., “Gold nanocages: synthesis, properties, and applications,” *Accounts of chemical research* **41**(12), 1587–1595 (2008).
- [48] Skrabalak, S. E., Chen, J., Au, L., Lu, X., Li, X., and Xia, Y., “Gold nanocages for biomedical applications,” *Advanced Materials* **19**(20), 3177–3184 (2007).

BIBLIOGRAPHY

- [49] Wiley, B., Sun, Y., Chen, J., Cang, H., Li, Z.-Y., Li, X., and Xia, Y., “Shape-controlled synthesis of silver and gold nanostructures,” *Mrs Bulletin* **30**(5), 356–361 (2005).
- [50] Xia, Y. and Halas, N. J., “Shape-controlled synthesis and surface plasmonic properties of metallic nanostructures,” *MRS bulletin* **30**(5), 338–348 (2005).
- [51] Haes, A. J., Haynes, C. L., McFarland, A. D., Schatz, G. C., Van Duyne, R. P., and Zou, S., “Plasmonic materials for surface-enhanced sensing and spectroscopy,” *MRS bulletin* **30**(5), 368–375 (2005).
- [52] Kumbhar, A. S., Kinnan, M. K., and Chumanov, G., “Multipole plasmon resonances of submicron silver particles,” *Journal of the American Chemical Society* **127**(36), 12444–12445 (2005).
- [53] Millstone, J. E., Park, S., Shuford, K. L., Qin, L., Schatz, G. C., and Mirkin, C. A., “Observation of a quadrupole plasmon mode for a colloidal solution of gold nanoprisms,” *Journal of the American Chemical Society* **127**(15), 5312–5313 (2005).
- [54] Shuford, K. L., Ratner, M. A., and Schatz, G. C., “Multipolar excitation in triangular nanoprisms,” *The Journal of chemical physics* **123**(11), 114713 (2005).
- [55] Henzie, J., Shuford, K. L., Kwak, E.-S., Schatz, G. C., and Odom, T. W., “Manipulating the optical properties of pyramidal nanoparticle arrays,” *The Journal of Physical Chemistry B* **110**(29), 14028–14031 (2006).
- [56] Kelly, K. L., Coronado, E., Zhao, L. L., and Schatz, G. C., “The optical properties of metal nanoparticles: the influence of size, shape, and dielectric environment,” (2003).

BIBLIOGRAPHY

- [57] Krenn, J. R., Schider, G., Rechberger, W., Lamprecht, B., Leitner, A., Aussenegg, F. R., and Weeber, J., “Design of multipolar plasmon excitations in silver nanoparticles,” *Applied Physics Letters* **77**(21), 3379–3381 (2000).
- [58] Jain, P. K., Lee, K. S., El-Sayed, I. H., and El-Sayed, M. A., “Calculated absorption and scattering properties of gold nanoparticles of different size, shape, and composition: applications in biological imaging and biomedicine,” *The journal of physical chemistry B* **110**(14), 7238–7248 (2006).
- [59] Murphy, C. J., Sau, T. K., Gole, A. M., Orendorff, C. J., Gao, J., Gou, L., Hunyadi, S. E., and Li, T., “Anisotropic metal nanoparticles: synthesis, assembly, and optical applications,” (2005).
- [60] Tesler, A. B., Maoz, B. M., Feldman, Y., Vaskevich, A., and Rubinstein, I., “Solid-state thermal dewetting of just-percolated gold films evaporated on glass: development of the morphology and optical properties,” *The Journal of Physical Chemistry C* **117**(21), 11337–11346 (2013).
- [61] Huang, J., Kim, F., Tao, A. R., Connor, S., and Yang, P., “Spontaneous formation of nanoparticle stripe patterns through dewetting,” *Nature materials* **4**(12), 896 (2005).
- [62] Do, M. T., Tong, Q. C., Luong, M. H., Lidiak, A., Ledoux-Rak, I., and Lai, N. D., “Fabrication and characterization of large-area unpatterned and patterned plasmonic gold nanostructures,” *Journal of Electronic Materials* **45**(5), 2347–2353 (2016).
- [63] Ma, F., Hong, M. H., and Tan, L. S., “Laser nano-fabrication of large-area plasmonic structures and surface plasmon resonance tuning by thermal effect,” *Appl. Phys. A* **93**, 907 (2008).

BIBLIOGRAPHY

- [64] Lee, F. Y., Fung, K. H., Tang, T. L., Tam, W. Y., and Chan, C., “Fabrication of gold nano-particle arrays using two-dimensional templates from holographic lithography,” *Current Applied Physics* **9**, 820 (2009).
- [65] Green, T., “Gold etching for microfabrication,” *Gold Bulletin* **47**(3), 205–216 (2014).
- [66] Lee, R. E., “Microfabrication by ion-beam etching,” *Journal of Vacuum Science and Technology* **16**(2), 164–170 (1979).
- [67] Tuma, J., Lyutakov, O., Huttel, I., Siegel, J., Heitz, J., Kalachyova, Y., and Svorcik, V., “Silver nano-structures prepared by oriented evaporation on laser-patterned poly(methyl methacrylate),” *Journal of Materials Science* **48**, 900905 (2013).
- [68] Brodie, I. and Muray, J. J., [*The physics of microfabrication*], Springer Science & Business Media (2013).
- [69] Koukharenko, E., Moktadir, Z., Kraft, M., Abdelsalam, M., Bagnall, D., Vale, C., Jones, M., and Hinds, E. A., “Microfabrication of gold wires for atom guides,” *Sensors and Actuators A: Physical* **115**(2-3), 600–607 (2004).
- [70] Do, M. T., Tong, Q. C., Luong, M. H., Lidiak, A., Ledoux-Rak, I., and Lai, N. D., “Fabrication and characterization of large-area unpatterned and patterned plasmonic gold nanostructures,” *Journal of Electronic Materials* **45**, 23472353 (2016).
- [71] Xu, L., Tan, L. S., and Hong, M. H., “Tuning of localized surface plasmon resonance of well-ordered ag/au bimetallic nanodot arrays by laser interference lithography and thermal annealing,” *Applied optics* **50**(31), G74–G79 (2011).

BIBLIOGRAPHY

- [72] Zheng, M., Yu, M., Liu, Y., Skomski, R., Liou, S., Sellmyer, D. J., Petryakov, V., Verevkin, Y. K., Polushkin, N., and Salashchenko, N., “Magnetic nanodot arrays produced by direct laser interference lithography,” *Applied Physics Letters* **79**(16), 2606–2608 (2001).
- [73] Favazza, C., Kalyanaraman, R., and Sureshkumar, R., “Robust nanopatterning by laser-induced dewetting of metal nanofilms,” *Nanotechnology* **17**, 42294234 (2006).
- [74] Berean, K. J., Sivan, V., Khodasevych, I., Boes, A., Gaspera, E. D., Field, M. R., and Kalantar-Zadeh, A. Mitchell, G. R. K., “Laser-induced dewetting for precise local generation of au nanostructures for tunable solar absorption,” *Advanced Optical Materials* **4**, 1247–1254 (2016).
- [75] He, R., Zhou, X., Fu, Y., and Zhang, Y., “Near-field optical experimental investigation of gold nanohole array,” *Plasmonics* **6**, 171 (2011).
- [76] Si, G., Jiang, X., Lv, J., Gu, Q., and Wang, F., “Fabrication and characterization of well-aligned plasmonic nanopillars with ultrasmall separations,” *Nano. Res. Lett.* **9**, 299 (2014).
- [77] Song, Y. and Elsayed-Ali, H. E., “Aqueous phase ag nanoparticles with controlled shapes fabricated by a modified nanosphere lithography and their optical properties,” *Appl. Surf. Sci.* **256**, 5961 (2010).
- [78] Bechelany, M., Maeder, X., Riesterer, J., Hankache, J., Lerose, D., Christiansen, S., Michler, J., and Philippe, L., “Synthesis mechanisms of organized gold nanoparticles: Influence of annealing temperature and atmosphere,” *Cryst. Growth Des.* **10**, 587 (2010).

BIBLIOGRAPHY

- [79] Hicks, E. M., Zou, S., Schatz, G. C., Spears, K. G., Van Duyne, R. P., Gunnarsson, L., Rindzevicius, T., Kasemo, B., and Käll, M., “Controlling plasmon line shapes through diffractive coupling in linear arrays of cylindrical nanoparticles fabricated by electron beam lithography,” *Nano letters* **5**(6), 1065–1070 (2005).
- [80] Sun, S. and Leggett, G. J., “Matching the resolution of electron beam lithography by scanning near-field photolithography,” *Nano Letters* **4**(8), 1381–1384 (2004).
- [81] Grigorenko, A. N., Geim, A. K., Gleeson, H. F., Zhang, Y., Firsov, A. A., Khrushchev, I. Y., and Petrovic, J., “Nanofabricated media with negative permeability at visible frequencies,” *Petrovic, Nature* **438**, 355 (2005).
- [82] Steinbruck, A., Choi, J. W., Fasold, S., Menzel, C., Sergeyev, A., Pertsch, T., and Grange, R., “Plasmonic heating with near infrared resonance nanodot arrays for multiplexing optofluidic applications,” *RSC Adv.* **4**, 61898 (2014).
- [83] Dial, O., Cheng, C.-C., and Scherer, A., “Fabrication of high-density nanostructures by electron beam lithography,” *Journal of Vacuum Science & Technology B: Microelectronics and Nanometer Structures Processing, Measurement, and Phenomena* **16**(6), 3887–3890 (1998).
- [84] Glass, R., Arnold, M., Bluemmel, J., Kueller, A., Moeller, M., and Spatz, J. P., “Micro-nanostructured interfaces fabricated by the use of inorganic block copolymer micellar monolayers as negative resist for electron-beam lithography,” *Advanced Functional Materials* **13**(7), 569–575 (2003).
- [85] Feng, J., Tuominen, M. T., and Rothstein, J. P., “Hierarchical superhydrophobic surfaces fabricated by dual-scale electron-beam-lithography with well-ordered secondary nanostructures,” *Advanced Functional Materials* **21**(19), 3715–3722 (2011).

BIBLIOGRAPHY

- [86] Tong, Q. C., Luong, M. H., Trang, T. M., Rimmel, J., Do, M. T., Kieu, D. M., Ghasemi, R., Nguyen, D. T., and Lai, N. D., “Realization of desired plasmonic structures via a direct laser writing technique,” *Journal of Electronic Materials* **46**, 36953701 (2017).
- [87] Hetherington, J. S., “Electron beam devices and processes,” (Jan. 14 1964). US Patent 3,118,050.
- [88] Tseng, A. A., Chen, K., Chen, C. D., and Ma, K. J., “Electron beam lithography in nanoscale fabrication: recent development,” *IEEE Transactions on electronics packaging manufacturing* **26**(2), 141–149 (2003).
- [89] Gao, H., Henzie, J., and Odom, T. W., “Direct evidence for surface plasmon-mediated enhanced light transmission through metallic nanohole arrays,” *Nano letters* **6**(9), 2104–2108 (2006).
- [90] Kwak, E.-S., Henzie, J., Chang, S.-H., Gray, S. K., Schatz, G. C., and Odom, T. W., “Surface plasmon standing waves in large-area subwavelength hole arrays,” *Nano Letters* **5**(10), 1963–1967 (2005).
- [91] Gonçalves, M. R., Makaryan, T., Enderle, F., Wiedemann, S., Plettl, A., Marti, O., and Ziemann, P., “Plasmonic nanostructures fabricated using nanosphere-lithography, soft-lithography and plasma etching,” *Beilstein journal of nanotechnology* **2**(1), 448–458 (2011).
- [92] Tong, Q. C., “Direct laser writing of polymeric and metallic nanostructures via optically induced local thermal effect,” *Doctor Thesis* **chapter 5**, 64 (2016).
- [93] Melngailis, J., “Focused ion beam technology and applications,” *Journal of Vacuum Science & Technology B: Microelectronics Processing and Phenomena* **5**(2), 469–495 (1987).

BIBLIOGRAPHY

- [94] Luong, M. H., “Theoretical and experimental investigations of plasmonic nanostructures and applications,” *Master Thesis* **chapter 2**, 13 (2016).
- [95] Tong, Q. C., Nguyen, D. T. T., Do, M. T., Luong, M. H., Journet, B., Ledoux-Rak, I., and Lai, N. D., “Direct laser writing of polymeric nanostructures via optically induced local thermal effect,” *Applied Physics Letters* **108**(18), 183104 (2016).
- [96] Khan, I., Saeed, K., and Khan, I., “Nanoparticles: Properties, applications and toxicities,” *Arabian Journal of Chemistry* **12**(7), 908–931 (2019).
- [97] Kravets, V., Neubeck, S., Grigorenko, A., and Kravets, A., “Plasmonic blackbody: Strong absorption of light by metal nanoparticles embedded in a dielectric matrix,” *Physical Review B* **81**(16), 165401 (2010).
- [98] Wang, Y., Hong, B. H., and Kim, K. S., “Size control of semimetal bismuth nanoparticles and the uv- visible and ir absorption spectra,” *The Journal of Physical Chemistry B* **109**(15), 7067–7072 (2005).
- [99] Zhu, J., Liu, Q. H., and Lin, T., “Manipulating light absorption of graphene using plasmonic nanoparticles,” *Nanoscale* **5**(17), 7785–7789 (2013).
- [100] Prabhu, R. R. and Khadar, M. A., “Characterization of chemically synthesized cds nanoparticles,” *Pramana* **65**(5), 801–807 (2005).
- [101] Lal, S., Link, S., and Halas, N. J., “Nano-optics from sensing to waveguiding,” *Nature photonics* **1**(11), 641 (2007).
- [102] Krenn, J. R., Ditlbacher, H., Schider, G., Hohenau, A., Leitner, A., and Aussenegg, F. R., “Surface plasmon micro-and nano-optics,” *Journal of microscopy* **209**(3), 167–172 (2003).

BIBLIOGRAPHY

- [103] Canfield, B. K., Kujala, S., Jefimovs, K., Turunen, J., and Kauranen, M., “Linear and nonlinear optical responses influenced by broken symmetry in an array of gold nanoparticles,” *Optics express* **12**(22), 5418–5423 (2004).
- [104] Danckwerts, M. and Novotny, L., “Optical frequency mixing at coupled gold nanoparticles,” *Physical Review Letters* **98**(2), 026104 (2007).
- [105] Haruta, M., “Catalysis of gold nanoparticles deposited on metal oxides,” *Cattech* **6**(3), 102–115 (2002).
- [106] Daniel, M.-C. and Astruc, D., “Gold nanoparticles: assembly, supramolecular chemistry, quantum-size-related properties, and applications toward biology, catalysis, and nanotechnology,” *Chemical reviews* **104**(1), 293–346 (2004).
- [107] Lytton-Jean, A. K. and Mirkin, C. A., “A thermodynamic investigation into the binding properties of dna functionalized gold nanoparticle probes and molecular fluorophore probes,” *Journal of the American Chemical Society* **127**(37), 12754–12755 (2005).
- [108] Leff, D. V., Ohara, P. C., Heath, J. R., and Gelbart, W. M., “Thermodynamic control of gold nanocrystal size: experiment and theory,” *The Journal of Physical Chemistry* **99**(18), 7036–7041 (1995).
- [109] Moyano, D. F., Rana, S., Bunz, U. H., and Rotello, V. M., “Gold nanoparticle-polymer/biopolymer complexes for protein sensing,” *Faraday discussions* **152**, 33–42 (2011).
- [110] Saha, K., Agasti, S. S., Kim, C., Li, X., and Rotello, V. M., “Gold nanoparticles in chemical and biological sensing,” *Chemical reviews* **112**(5), 2739–2779 (2012).

BIBLIOGRAPHY

- [111] Caro, C., Castillo, P. M., Klippstein, R., Pozo, D., and Zaderenko, A. P., “Silver nanoparticles: sensing and imaging applications,” *Silver nanoparticles* , 201–24 (2010).
- [112] Marra, J., Voetz, M., and Kiesling, H.-J., “Monitor for detecting and assessing exposure to airborne nanoparticles,” *Journal of Nanoparticle Research* **12**(1), 21–37 (2010).
- [113] Huang, X., Jain, P. K., El-Sayed, I. H., and El-Sayed, M. A., “Gold nanoparticles: interesting optical properties and recent applications in cancer diagnostics and therapy,” (2007).
- [114] Inoue, M., Hayashi, Y., Takizawa, H., and Suganuma, K., “Nanoparticle fabrication,” in [*Nanopackaging*], 219–242, Springer (2018).
- [115] Yamanaka, S., Suzuma, A., Fujimoto, T., and Kuga, Y., “Production of scallop shell nanoparticles by mechanical grinding as a formaldehyde adsorbent,” *Journal of nanoparticle research* **15**(4), 1573 (2013).
- [116] Damonte, L., Zélis, L. M., Soucase, B. M., and Fenollosa, M. H., “Nanoparticles of zno obtained by mechanical milling,” *Powder Technology* **148**(1), 15–19 (2004).
- [117] Zeng, H., Sun, S., Sandstrom, R., and Murray, C., “Chemical ordering of fept nanoparticle self-assemblies by rapid thermal annealing,” *Journal of magnetism and magnetic materials* **266**(1-2), 227–232 (2003).
- [118] Jovic, N. G., Masadeh, A. S., Kremenovic, A. S., Antic, B. V., Blanusa, J. L., Cvjeticanin, N. D., Goya, G. F., Antisari, M. V., and Bozin, E. S., “Effects of thermal annealing on structural and magnetic properties of lithium ferrite

BIBLIOGRAPHY

- nanoparticles,” *The Journal of Physical Chemistry C* **113**(48), 20559–20567 (2009).
- [119] Philip, J., Gnanaprakash, G., Panneerselvam, G., Antony, M., Jayakumar, T., and Raj, B., “Effect of thermal annealing under vacuum on the crystal structure, size, and magnetic properties of zn fe 2 o 4 nanoparticles,” *Journal of Applied Physics* **102**(5), 054305 (2007).
- [120] Roco, M., “Nanoparticles and nanotechnology research,” *Journal of Nanoparticle Research* **1**(1), 1 (1999).
- [121] Hoepfner, S., Maoz, R., Cohen, S. R., Chi, L., Fuchs, H., and Sagiv, J., “Metal nanoparticles, nanowires, and contact electrodes self-assembled on patterned monolayer templatesa bottom-up chemical approach,” *Advanced Materials* **14**(15), 1036–1041 (2002).
- [122] Khatoon, H., Nasir, J., Shafiq, M., and Rizvi, S. H. H., [*Nanotechnology. Synthesis techniques of silver nanoparticles*], Anchor Academic Publishing (2016).
- [123] Lee, J.-M. and Kim, B.-I., “Thermal dewetting of pt thin film: Etch-masks for the fabrication of semiconductor nanostructures,” *Materials Science and Engineering: A* **449**, 769–773 (2007).
- [124] Monkawa, A., Ikoma, T., Yunoki, S., Ohta, K., and Tanaka, J., “A dewetting process to nano-pattern collagen on hydroxyapatite,” *Materials Letters* **60**(29-30), 3647–3650 (2006).
- [125] Hayashi, Y., Inoue, M., Takizawa, H., and Sugauma, K., “Nanoparticle fabrication,” in [*Nanopackaging*], 109–120, Springer (2008).
- [126] Buffat, P. and Borel, J. P., “Size effect on the melting temperature of gold particles,” *Physical review A* **13**(6), 2287 (1976).

BIBLIOGRAPHY

- [127] Tan, S. J., Zhang, L., Zhu, D., Goh, X. M., Wang, Y. M., Kumar, K., Qiu, C.-W., and Yang, J. K., “Plasmonic color palettes for photorealistic printing with aluminum nanostructures,” *Nano letters* **14**(7), 4023–4029 (2014).
- [128] Genet, C. and Ebbesen, T. W., “Light in tiny holes,” in [*Nanoscience And Technology: A Collection of Reviews from Nature Journals*], 205–212, World Scientific (2010).
- [129] Pradhan, N., Pal, A., and Pal, T., “Silver nanoparticle catalyzed reduction of aromatic nitro compounds,” *Colloids and Surfaces A: Physicochemical and Engineering Aspects* **196**(2-3), 247–257 (2002).
- [130] Kallman, E. N., Oyanedel-Craver, V. A., and Smith, J. A., “Ceramic filters impregnated with silver nanoparticles for point-of-use water treatment in rural guatemala,” *Journal of Environmental Engineering* **137**(6), 407–415 (2011).
- [131] Pandey, S., Goswami, G. K., and Nanda, K. K., “Green synthesis of biopolymer–silver nanoparticle nanocomposite: An optical sensor for ammonia detection,” *International journal of biological macromolecules* **51**(4), 583–589 (2012).
- [132] Yung, W. K., Liu, J., Man, H., and Yue, T., “355 nm nd: Yag laser ablation of polyimide and its thermal effect,” *Journal of Materials Processing Technology* **101**(1-3), 306–311 (2000).
- [133] Küper, S. and Stuke, M., “Femtosecond uv excimer laser ablation,” *Applied Physics B* **44**(4), 199–204 (1987).
- [134] Yilbas, B., “Laser cutting quality assessment and thermal efficiency analysis,” *Journal of Materials Processing Technology* **155**, 2106–2115 (2004).
- [135] Tong, Q. C., Luong, M. H., Tran, T. M., Rimmel, J., Do, M. T., Kieu, D. M., Ghasemi, R., Nguyen, D. T., and Lai, N. D., “Realization of desired plasmonic

BIBLIOGRAPHY

- structures via a direct laser writing technique,” *Journal of Electronic Materials* **46**(6), 3695–3701 (2017).
- [136] Nguyen, D. T. T., “Controlled coupling of nanoparticles to polymer-based photonic structures,” *Doctor Thesis* **chapter 2**, 22 (2018).
- [137] Nguyen, D. T. T., Tong, Q. C., Ledoux-Rak, I., and Lai, N. D., “One-step fabrication of submicrostructures by low one-photon absorption direct laser writing technique with local thermal effect,” *Journal of Applied Physics* **119**, 013101 (Jan. 2016).
- [138] Díaz, J. I. and Lions, P.-L., [*Nonlinear partial differential equations and free boundaries*], vol. 106, Pitman London (1985).
- [139] Zienkiewicz, O. C., Taylor, R. L., Nithiarasu, P., and Zhu, J., [*The finite element method*], vol. 3, McGraw-hill London (1977).
- [140] Singh, S. C., Zeng, H., Guo, C., and Cai, W., [*Nanomaterials: processing and characterization with lasers*], John Wiley & Sons (2012).
- [141] Pozo, D., [*Silver nanoparticles*], BoD–Books on Demand (2010).
- [142] Fischer, J. and Wegener, M., “Three-dimensional optical laser lithography beyond the diffraction limit,” *Laser & Photonics Reviews* **7**, 22–44 (Jan. 2013).
- [143] Brown, M. S. and Arnold, C. B., “Fundamentals of laser-material interaction and application to multiscale surface modification,” in [*Laser Precision Microfabrication*], 91–120, Springer (2010).
- [144] Wang, J., Chen, Y., Chen, X., Hao, J., Yan, M., and Qiu, M., “Photothermal reshaping of gold nanoparticles in a plasmonic absorber,” *Optics express* **19**(15), 14726–14734 (2011).

BIBLIOGRAPHY

- [145] Mao, F., Davis, A., Tong, Q. C., Luong, M. H., Nguyen, C. T., Ledoux-Rak, I., and Lai, N. D., “Direct laser writing of gold nanostructures: application to data storage and color nanoprinting,” *Plasmonics* **13**(6), 2285–2291 (2018).
- [146] Mao, F., Davis, A., Tong, Q. C., Luong, M. H., Nguyen, C. T., Ledoux-Rak, I., and Lai, N. D., “Direct laser coding of plasmonic nanostructures for data storage applications,” in [*Nanophotonics VII*], **10672**, 106722Z, International Society for Optics and Photonics (2018).
- [147] Burke, W. J., Kressel, H., and Ettenberg, M., “Optical memory with injection laser as light source and detector,” (Dec. 23 1980). US Patent 4,241,423.
- [148] Lambert, S. and Ropiequet, S., [*CD ROM. The New Papyrus: The Current and Future State of the Art.*], ERIC (1986).
- [149] Ramalingam, M., Tiwari, A., Ramakrishna, S., and Kobayashi, H., [*Integrated biomaterials for biomedical technology*], vol. 6, John Wiley & Sons (2012).
- [150] Bardhan, R., Grady, N. K., Cole, J. R., Joshi, A., and Halas, N. J., “Fluorescence enhancement by au nanostructures: nanoshells and nanorods,” *ACS nano* **3**(3), 744–752 (2009).
- [151] Zhai, T., Zhang, X., Pang, Z., Su, X., Liu, H., Feng, S., and Wang, L., “Random laser based on waveguided plasmonic gain channels,” *Nano letters* **11**(10), 4295–4298 (2011).
- [152] Popov, O., Zilbershtein, A., and Davidov, D., “Random lasing from dye-gold nanoparticles in polymer films: enhanced gain at the surface-plasmon-resonance wavelength,” *Applied physics letters* **89**(19), 191116 (2006).

BIBLIOGRAPHY

- [153] Heydari, E., Flehr, R., and Stumpe, J., “Influence of spacer layer on enhancement of nanoplasmon-assisted random lasing,” *Applied Physics Letters* **102**(13), 133110 (2013).

Title : Realization of desired Au and Ag nanostructures by optically induced local thermal effect: Application to data storage and color printer

Keywords : Plasmonics, DLW, gold and silver nanoparticles, data storage, nano color printing, fluorescence enhancement, random laser.

Abstract : This work focuses on the investigation of plasmonic Gold (Au) and Silver (Ag) nanoparticles (NPs) by using optically induced local thermal dewetting technique and their applications. Firstly, Au and Ag NPs are fabricated by a thermal annealing method using a hot oven. This technique allows obtaining Au and Ag NPs, which are randomly distributed in a large area. The NPs sizes and properties are controlled by annealing conditions, such as annealing temperature and duration. Plasmonic properties of Au and Ag NPs are experimentally characterized and compared with the simulation ones performed by the FDTD method. These large-area Au and Ag NPs are demonstrated to be useful for applications in fluorescence enhancement and random laser. Secondly, we demonstrate a robust way to realize desired plasmonic nanostructures by using a direct laser writing method. This technique bases on optically induced local thermal effect allowing the realization of NPs at a small area, i.e. focusing area. By moving thus the laser spot, any desired plasmonic structure can be realized. The NPs sizes and distributions can be controlled by exposure doses (laser power and exposure time) and moving trajectory of the focusing spot resulting in different reflection or transmission colors. By focusing a continuous-wave laser at 532 nm on Au films having 50 nm thickness, we demonstrated for the first time the direct fabrication of plasmonic nanoholes array. These fabricated structures are demonstrated to be very potential for many applications such as data storage, color nanoprinter, fluorescence enhancement, and plasmonics based random laser.

Titre : Réalisation des nanostructures désirées en or et en argent par effet thermique local induit optiquement: Application au stockage de données et à l'imprimante couleur

Keywords : DLW, Plasmonique, nanoparticules d'or, nanoparticules d'argent, nano-imprimante, stockage de données, laser, fluorescence.

Résumé : Ce travail se concentre sur l'étude des nanoparticules (NPs) d'or (Au) et d'argent (Ag) en utilisant la technique de démouillage thermique induite optiquement et leurs applications. Premièrement, les NPs d'Au et d'Ag sont fabriquées par un procédé de recuit thermique utilisant un four chaud. Cette technique permet d'obtenir des NPs d'Au et d'Ag distribuées de manière aléatoire en grande surface. La taille et les propriétés des NPs sont contrôlées par les conditions de recuit, telles que la température et le temps de recuit. Les propriétés plasmoniques des NPs d'Au et d'Ag sont caractérisées et comparées expérimentalement avec celles de la simulation réalisée par la méthode FDTD. Il a été démontré que ces NPs d'Au et d'Ag en grande surface sont utiles pour des applications comme l'amélioration de la fluorescence et le laser aléatoire à base de l'effet plasmonique. Deuxièmement, nous avons démontré un moyen robuste pour réaliser des nanostructures plasmoniques souhaitées en utilisant la méthode d'écriture directe par laser. Cette technique repose sur un effet thermique local induit optiquement permettant la réalisation des NPs dans une petite zone, à savoir une zone de focalisation. En déplaçant ainsi le spot de focalisation, toute structure plasmonique souhaitée en 1D et 2D peut être réalisée. La taille et la distribution des NPs peuvent être contrôlées par des doses d'exposition (durée d'exposition et puissance du laser) et par le trajectoire du mouvement du spot de focalisation. De plus, en focalisant un laser continu à 532 nm sur un film d'Au ou d'Ag ayant une épaisseur de 50 nm, nous avons démontré pour la première fois la fabrication directe d'un réseau de nano-trous plasmonique. Il a été démontré que ces structures fabriquées présentaient un fort potentiel pour de nombreuses applications telles que le stockage de données, l'imprimante couleur, l'amélioration de la fluorescence et le laser aléatoire.

Titre : Réalisation des nanostructures désirées en or et en argent par effet thermique local induit optiquement: Application au stockage de données et à l'imprimante couleur

Keywords : DLW, Plasmonique, nanoparticules d'or, nanoparticules d'argent, nano-imprimante, stockage de données, laser, fluorescence.

Dans ce travail, nous avons systématiquement étudié la fabrication de monocouches à grande surface de nanoparticules (NPs) d'or (Au) et d'argent (Ag). Nous avons démontré la fabrication de NPs Au et Ag par la méthode de démouillage thermique dans un four (Fig. 1 (a) et (d)). En analysant leurs images SEM, les morphologies d'abord et la distribution des tailles, sont caractérisées. Nous avons discuté de la température de recuit et de la durée du recuit pour former des Au et Ag NPs. À différentes températures de recuit, les pics résonants des NPs d'Or ou d'Argent ont légèrement changé, ce qui correspond à une distribution de taille moyenne différente (Fig. 1 (b) et (e)). Et pour différentes durées de recuit, l'intensité des pics résonants est différente, et elle répond à différents nombres de NPs. Ensuite, à l'aide de la méthode FDTD, les propriétés optiques des Au et Ag NPs ont été simulées en important des images SEM de la forme aléatoire des NPs. Pour les NPs Au, les pics de résonance plasmonique sont décalés vers le rouge de 48 nm lorsque la taille moyenne des NPs passe de 20 nm à 100 nm (Fig. 1 (c)). Et pour les Ag NPs, lorsque les tailles moyennes sont passées de 20 nm à 40 nm, les pics de résonance sont décalés vers le bleu, puis décalés vers le rouge lorsque la taille moyenne dépasse 40 nm (figure 1 (f)). Les impacts environnementaux ont également été discutés. Lorsque les NPs passent de l'air à l'eau puis à l'huile, les pics de résonance passent au rouge (Fig. 1 (g)). Nous avons également étudié un mixte Au et Ag NPs par cette méthode de recuit thermique. Au début, nous avons essayé d'utiliser la même température de recuit, qui peut former les Au et Ag NPs séparément, pour former les Au et Ag NPs combinés. Nous avons échoué car ils ne pouvaient pas former de NPs. Après cela, nous avons essayé de déposer l'Ag sur les Au NPs (Fig. 1 (h)). La courbe de résonance a montré deux pics aux positions des NPs purs d'Or et d'Argent. Les résultats de la simulation FDTD, qui définissent la moitié des NPs comme Or et l'autre moitié comme Argent, sont cohérents avec la position de pointe de l'expérience (Fig.1 (i)), ce qui signifie que

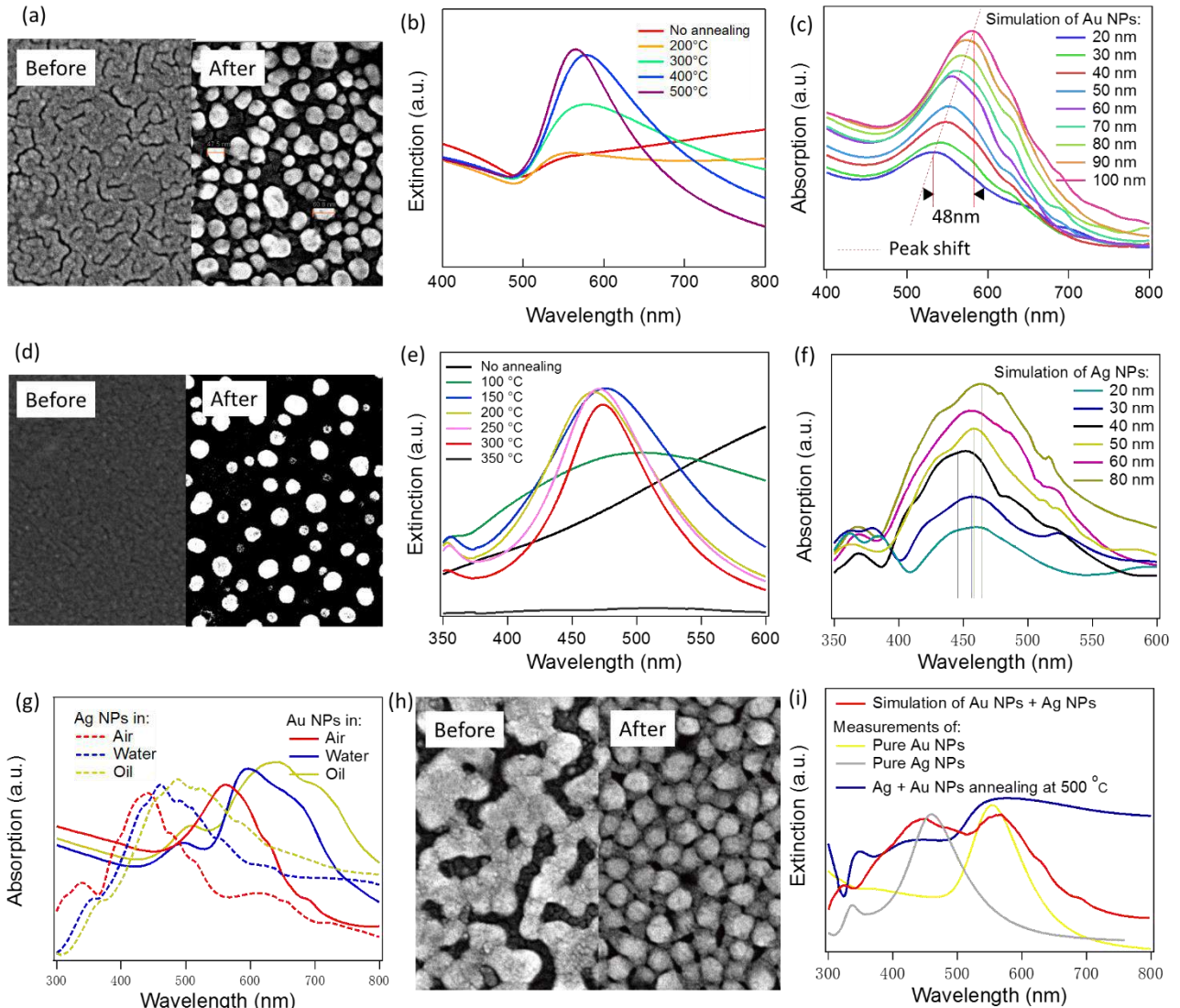


Figure 1: (a) Comparaison des images SEM du film Au et des Au NPs (film Au recuit). (b) Les spectres d'extinction (absorption et diffusion combinées) d'échantillons d'Au recuits à différentes températures en 30 minutes. (c) Les spectres d'absorption simulés de Au NPs avec différentes tailles moyennes de NPs. (d) Comparaison des images SEM d'un film d'Ag et NPs d'Ag. (e) Les spectres d'extinction d'échantillons d'Ag recuits à différentes températures. (f) Les spectres d'absorption simulés NPs d'Ag avec différentes tailles moyennes de NPs. (g) Simulation FDTD de la dépendance des propriétés plasmoniques des Au NPs et Ag NPs sur l'environnement. (h) Comparaison d'images SEM d'un film d'Ag couvert sur Au NPs et après recuit à 500 ° C. (i) Le spectre d'absorption du recuit thermique.

Ag est couvert sur les Au NPs.

Nous avons démontré l'effet thermique induit optiquement sur la fabrication de PNS métalliques dans une petite zone. Nous avons théoriquement étudié l'effet thermique induit optiquement dans un film métallique réel en utilisant le programme Comsol (Fig. 2 (a)), qui peut traiter la surface rugueuse comme dans l'expérience. Nous avons étudié la température induite dans le centre de focalisation du laser en fonction de l'intensité du laser et du temps d'exposition (Fig. 2 (b)). Il montre que la température atteindra une valeur stable après 30 μ s et que la température maximale induite change linéairement en fonction de l'intensité du laser. Nous avons appliqué les simulations pour les matériaux Au et Ag. Nous avons constaté que la puissance laser nécessaire pour obtenir les NPs d'Ag est bien inférieure à celle requise pour les NPs d'Au (Fig. 2 (c)). L'effet thermique induit optiquement de différentes épaisseurs, 12 nm et 50 nm, respectivement, est étudié (Fig. 2 (d)). Pour le film de 12 nm d'épaisseur, la température induite élevée est facile à couper la connexion dans le film métallique pour former les NPs métalliques. Mais pour le film de 50 nm d'épaisseur, il peut former des nano-trous (NHA) lorsque la température induite localisée est suffisamment élevée pour évaporer le métal. Nous avons étudié la distribution de température d'un film métallique épais de 50 nm pour deux cas: une surface parfaitement uniforme et l'autre rugueuse. Avec la même puissance laser, le laser se concentre pour créer un point de température circulaire parfait pour un film métallique uniforme tandis que dans le cas d'une surface rugueuse, le point de température est irrégulier. Ensuite, les Au NPs, Ag NPs et Au NHA sont fabriqués en utilisant la méthode DLW. Nous avons d'abord expliqué le principe de fonctionnement du système, puis comment combiner le logiciel Matlab avec le programme Labview. En utilisant ce système DLW, nous avons obtenu les Au et Ag NPs avec différentes tailles de particules en contrôlant la puissance du laser et le temps d'exposition (Fig. 2 (e) et (f)). Les résultats des changements de couleur et de taille sont cohérents avec les simulations FDTD. Après cela, une méthode d'écriture en deux étapes est suggérée pour améliorer la période minimale de la structure 1D, qui montre un PNS Au stable avec une période minimale de 400 nm.

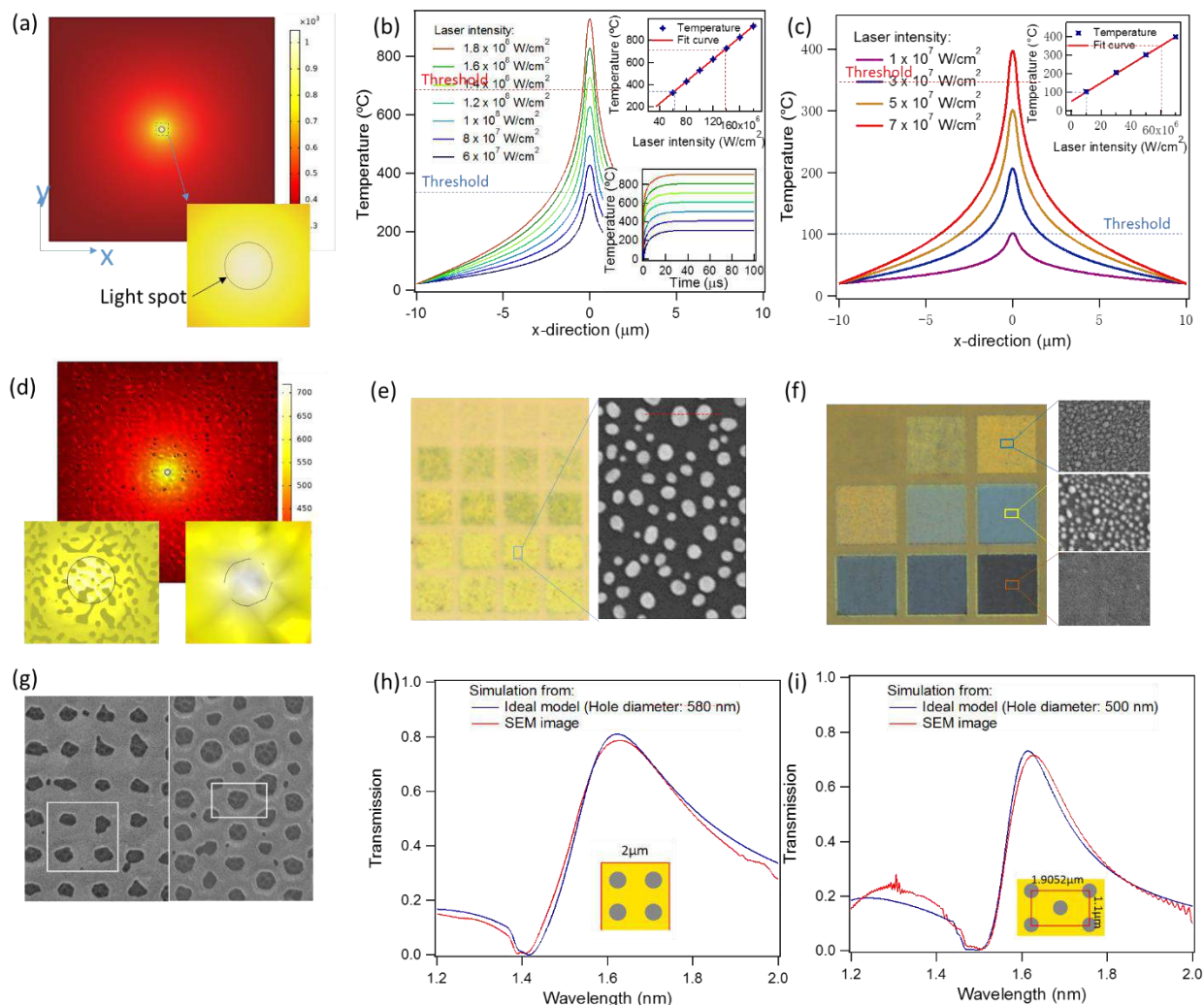


Figure 2: (a) La distribution de température induite autour du point focal à l'aide du programme Comsol. (b) Le profil de température induit du film Au le long de la direction x obtenu avec différentes intensités laser. Insérer le chiffre est le maximum et l'évolution de la température induite dans le centre de mise au point. (c) Le profil de température induit du film Au. Insérer le chiffre correspond aux variations de température induites maximales avec l'intensité du laser. (d) Comparaison de la distribution de température induite sur des films Au minces (12 nm) et épais (50 nm). (e) Au NPs obtenus par la méthode DLW avec différents paramètres d'écriture. L'insertion est l'image SEM correspondante. (f) Ag NPs obtenus par la méthode DLW. (g) Au NHA avec 2 configurations obtenues par la méthode DLW. (h, i) Comparaison des spectres de transmission d'un modèle idéal et d'une structure fabriquée réelle de configurations carrées et hexagonales, respectivement.

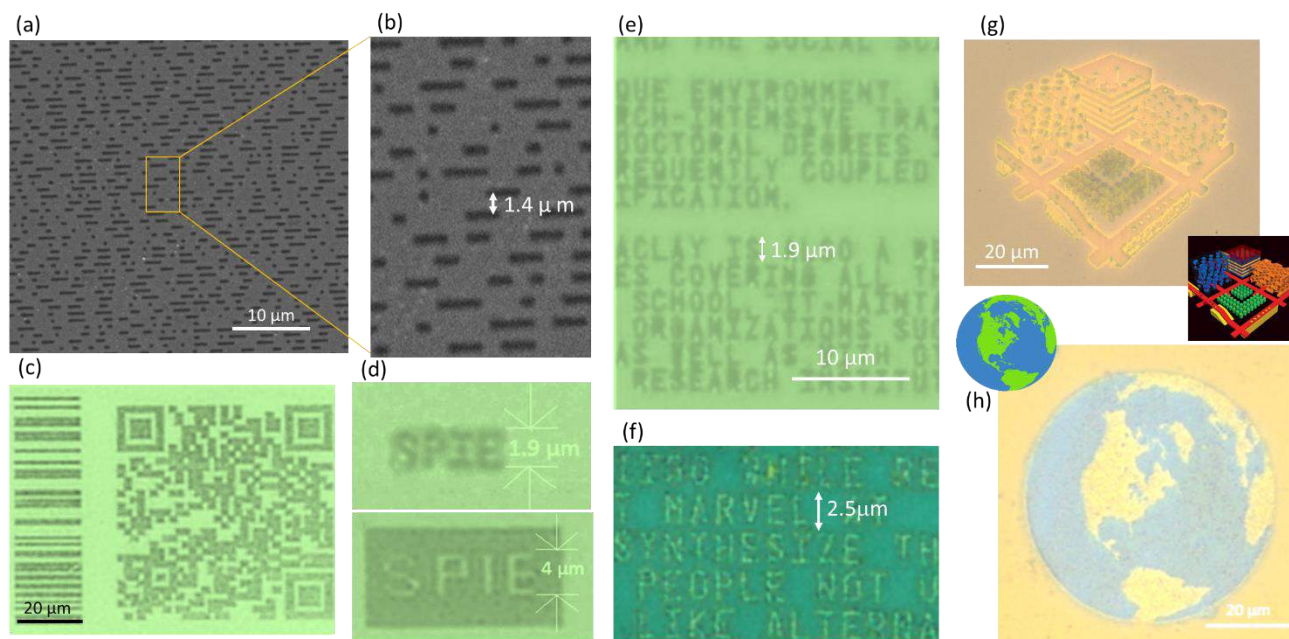


Figure 3: (a, b) Image SEM d'écriture binaire avec la méthode DLW, la période est de 1,4 μm . c) Code à barres et code QR réalisés sur le film Au par la méthode DLW, qui renvoient au site Web du laboratoire de l'auteur. (d) Écriture directe de texte de PNS avec Au NPs à micro-échelle. La hauteur de la lettre est de 1,9 μm . (e) Écriture de texte directe inverse. (f) Rédaction directe de texte avec Au NPs sur une seule page. (g) Écriture directe de texte avec Ag NPs. (h) L'impression nano couleur des Au NPs. (i) L'impression nano couleur des motifs Ag NPs. L'insertion d'image est l'image d'origine.

Nous avons également démontré la fabrication des Au NHA en utilisant ce système DLW (Fig. 2 (g)) et étudié théoriquement leurs propriétés optiques. Dans l'expérience, deux types de structures Au NHA, carrées et hexagonales, sont obtenues sur la couche Au de 50 nm d'épaisseur. Les périodes de structures carrées et hexagonales sont respectivement de 1 μm et 1,1 μm . Les nano-trous expérimentaux montrent des formes irrégulières, qui sont cohérentes avec les simulations dues à la surface rugueuse du film Au. Ensuite, le spectre de transmission de Au NHA de ces deux structures est étudié. Le pic de transmission élevé apparaît autour de 1550 nm pour la structure carrée et à 1450 nm pour la structure hexagonale. Les nano-trous étant irréguliers, la distribution et la transmission du champ électrique du NHA sont étudiées et comparées aux modèles idéaux. Nous avons constaté que même les distributions de champ électrique de la structure réelle et du modèle idéal

sont très différentes à la position des nano-trous, mais les spectres de transmission sont presque les mêmes (Fig. 2 (h) et (i)). Cela a prouvé que les résonances plasmoniques d'Au NHA dépendent du diamètre, de la période et de la structure du nanohole, mais pas de la forme des nanoholes. Ceci est similaire au résultat de la résonance plasmonique des NPs métalliques, pour laquelle les spectres de résonance dépendent également de la taille moyenne des NPs métalliques au lieu de la forme de chaque NP.

Plusieurs applications de PNS basées sur les Au et Ag NPs ont été démontrées. Une nouvelle méthode de stockage de données utilisant des Au ou Ag NPs est d'abord introduite. Comme notre méthode d'écriture DLW est similaire à celle des CD et DVD, nous avons utilisé cette méthode pour écrire les codes binaires sur film métallique et comparer sa capacité avec celle des CD et DVD standard (Fig.3 (a) et (b)). La capacité d'écriture plasmonique est d'environ 914 Mo pour le moment, ce qui est mieux qu'un CD standard mais moins bon que le DVD standard. Ensuite, le code à barres micrométrique et l'enregistrement du code QR sont également démontrés (Fig. 3 (c)). Un exemple de QR code dont la taille est de 70×70 (μm^2), qui renvoie au site Internet de notre laboratoire, est réalisé comme preuve de principe. Après cela, nous démontrons l'écriture de texte directe avec les Au et Ag NPs (Fig. 3 (d)). La hauteur de la lettre des Au NPs est de $1,9 \mu\text{m}$ (Fig. 3 (e)), tandis que la hauteur de la lettre des Ag NPs est de $2,5 \mu\text{m}$ (Fig. 3 (f)). Cela est dû au fait que les Au NPs ont une disposition de particules plus dense que les Ag NPs, donc le bord entre les Au NPs et le film non exposé est plus clair que celui de l'Ag. Ensuite, nous avons démontré l'impression nano couleur de PNS avec Au et Ag NPs (Fig. 3 (g) et (h)). Nous avons introduit le réglage de la couleur plasmonique en modifiant les paramètres de la dose d'exposition. Et puis nous avons appliqué cette idée pour réaliser des nanostructures avec différentes couleurs. Pour obtenir différentes couleurs plasmoniques, les vitesses de balayage, les puissances laser et la distance entre les lignes de balayage varient. Cela permet la réalisation de différentes images aimées à l'échelle microscopique. Les couleurs sont cependant limitées au rouge, au jaune et au vert pour les NPs Au et au jaune et bleu pour les Ag NPs. Parce que la résonance plasmonique localisée des NPs métalliques change très faiblement en fonction de leur taille.

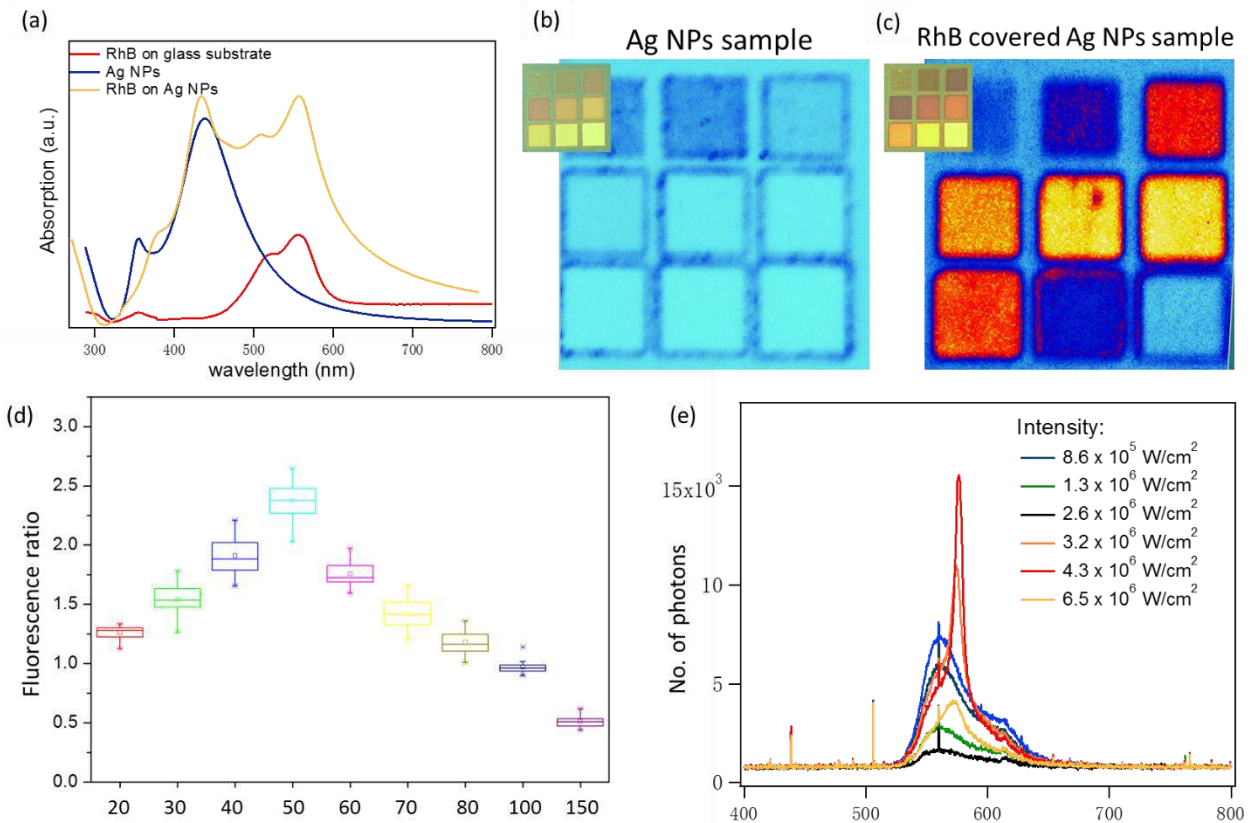


Figure 4: (a) Spectres d'absorption de la couche de fluorophore (RhB), NPs d'Ag et du spin-coating de la couche de fluorophore sur Ag NPs. (b, c) Les images de fluorescence avec les échantillons d'Ag obtenus avant et après le dépôt de RhB, respectivement. Les insertions sont les images de microscope correspondantes. (d) Calcul des taux d'accroissement de la fluorescence. (e) Spectres d'émission de RhB/SU8 revêtus par centrifugation sur une monocouche de NP Au. L'épaisseur de RhB/SU8 est de 1000 nm.

Après cela, nous avons démontré une augmentation de la fluorescence des Ag NPs recouverts de RhB/PMMA (Fig. 4 (a)). Les images de fluorescence présentent des changements significatifs (Fig. 4 (b) et (c)), dont l'échelle de fluorescence est la même. Grâce à l'amélioration du champ à proximité des NPs métalliques, la fluorescence de RhB/PMMA est augmentée d'un facteur allant jusqu'à 2,38 (Fig. 4 (d)). Le taux d'amélioration dépend de la taille des NPs, qui est contrôlée par la puissance laser de la technique DLW. En couvrant une image plasmonique avec un RhB/PMMA mince, nous avons montré que l'image de fluorescence d'une telle structure plasmonique est plus claire avec un contraste plus élevé. Enfin, nous avons démontré le premier essai pour obtenir un laser aléatoire de Au NPs (Fig.

4 (e)). Le résultat préliminaire, en modifiant l'épaisseur du film et l'intensité de pompage, montre qu'une forte émission spontanée amplifiée a été obtenue.

Titre : Réalisation des nanostructures désirées en or et en argent par effet thermique local induit optiquement: Application au stockage de données et à l'imprimante couleur

Mots clés : DLW, Plasmonique, nanoparticules d'or, nanoparticules d'argent, nano-imprimante, stockage de données, laser, fluorescence.

Résumé : Ce travail se concentre sur l'étude des nanoparticules (NPs) d'or (Au) et d'argent (Ag) en utilisant la technique de démouillage thermique induite optiquement et leurs applications. Premièrement, les NPs d'Au et d'Ag sont fabriquées par un procédé de recuit thermique utilisant un four chaud. Cette technique permet d'obtenir des NPs d'Au et d'Ag distribuées de manière aléatoire en grande surface. La taille et les propriétés des NPs sont contrôlées par les conditions de recuit, telles que la température et le temps de recuit. Les propriétés plasmoniques des NPs d'Au et d'Ag sont caractérisées et comparées expérimentalement avec celles de la simulation réalisée par la méthode FDTD. Il a été démontré que ces NPs d'Au et d'Ag en grande surface sont utiles pour des applications comme l'amélioration de la fluorescence et le laser aléatoire à base de l'effet plasmonique. Deuxièmement, nous avons démontré un moyen robuste pour réaliser des nanostructures

plasmoniques souhaitées en utilisant la méthode d'écriture directe par laser. Cette technique repose sur un effet thermique local induit optiquement permettant la réalisation des NPs dans une petite zone, à savoir une zone de focalisation. En déplaçant ainsi le spot de focalisation, toute structure plasmonique souhaitée en 1D et 2D peut être réalisée. La taille et la distribution des NPs peuvent être contrôlées par des doses d'exposition (durée d'exposition et puissance du laser) et par le trajectoire du mouvement du spot de focalisation. De plus, en focalisant un laser continu à 532 nm sur un film d'Au ou d'Ag ayant une épaisseur de 50 nm, nous avons démontré pour la première fois la fabrication directe d'un réseau de nano-trous plasmonique. Il a été démontré que ces structures fabriquées présentaient un fort potentiel pour de nombreuses applications telles que le stockage de données, l'imprimante couleur, l'amélioration de la fluorescence et le laser aléatoire.

Title : Realization of desired Au and Ag nanostructures by optically induced local thermal effect: Application to data storage and color printer

Keywords : Plasmonics, DLW, gold and silver nanoparticles, data storage, nano color printing, fluorescence enhancement, random laser.

Abstract : This work focuses on the investigation of plasmonic Gold (Au) and Silver (Ag) nanoparticles (NPs) by using optically induced local thermal dewetting technique and their applications. Firstly, Au and Ag NPs are fabricated by a thermal annealing method using a hot oven. This technique allows obtaining Au and Ag NPs, which are randomly distributed in a large area. The NPs sizes and properties are controlled by annealing conditions, such as annealing temperature and duration. Plasmonic properties of Au and Ag NPs are experimentally characterized and compared with the simulation ones performed by the FDTD method. These large-area Au and Ag NPs are demonstrated to be useful for applications in fluorescence enhancement and random laser. Secondly, we demonstrate a robust way to realize desired plas-

monic nanostructures by using a direct laser writing method. This technique bases on optically induced local thermal effect allowing the realization of NPs at a small area, i.e. focusing area. By moving thus the laser spot, any desired plasmonic structure can be realized. The NPs sizes and distributions can be controlled by exposure doses (laser power and exposure time) and moving trajectory of the focusing spot resulting in different reflection or transmission colors. By focusing a continuous-wave laser at 532 nm on Au films having 50 nm thickness, we demonstrated for the first time the direct fabrication of plasmonic nanoholes array. These fabricated structures are demonstrated to be very potential for many applications such as data storage, color nanoprinter, fluorescence enhancement, and plasmonics based random laser.